The Dissertation Committee for Xiao Li
certifies that this is the approved version of the following dissertation:

Quantum Hall effects in novel 2D electron systems: Nontrivial Fermi surface topology and quantum Hall ferromagnetism

Committee:

Qian Niu, Supervisor

Allan H. MacDonald

Gregory A. Fiete

Zhen Yao

Emanuel Tutuc

Quantum Hall effects in novel 2D electron systems: Nontrivial Fermi surface topology and quantum Hall ferromagnetism

by

Xiao Li, B.S.

DISSERTATION

Presented to the Faculty of the Graduate School of

The University of Texas at Austin

in Partial Fulfillment

of the Requirements

for the Degree of

DOCTOR OF PHILOSOPHY

THE UNIVERSITY OF TEXAS AT AUSTIN

December 2014

To my dear mother

Acknowledgments

I would like to express my sincere gratitude to several people for their support throughout my time in Austin.

First and foremost, I would like to thank my advisor Qian Niu. During my six and a half years with him, I have benefited a lot from him. He is a great physicist. He has great physical insights and can quickly capture the essence of a problem, which makes our discussions very enjoyable. He is also a very nice person. He is always willing to discuss with his students, encourages them to explore new ideas, and is always trying to help. It is my great pleasure to work with him, and my great fortune to be his student.

I would like to thank Allan MacDonald. Allan is a great mentor and a friend. It is rare to see physicists as clever, kind, and knowledgable as him. He played a critical role in my career. I was very fortunate to become one of his mentees during my formative years as a physicist. During these years he opens up the beautiful world of condensed matter theory in front of me, and gave me the tools to make explorations by myself. My knowledge and vision were greatly expanded during these years under his guidance. In addition, he took very good care of me, and opened up various wonderful opportunities for me in every stage of my career. I totally enjoyed this remarkable adventure with him, and I am greatly indebted to him.

I would like to thank my teacher and friend Fan Zhang. I am very fortunate to know him and work under his guidance. Our collaborations dated back to one evening in March 2012, when I received a call from him. He proposed to study the optical conductivity of trilayer graphene with me, and gave me very detailed instructions along the way. This initial project laid a solid foundation for our very successful collaborations later. We have published two papers in Physical Review Letters to date, and a lot more are on the way. The guidance and help from Fan was a key factor in my PhD studies. My career would have been very different without him.

I would like to thank Chuanwei Zhang and Vito Scarola. I did not get to know them until the last year of my PhD studies, but they also played important roles in my career. I had the great opportunity to work with them during the summer of 2014, and learnt a lot from them. In addition, they always have firm belief in me. I am very grateful for their support.

I would like to thank my other collaborators, including Yugui Yao, Zhenhua Qiao, Shengyuan Yang, Wang-kong Tse, and Jeil Jung. The various interactions with them greatly benefited me, and helped me become a better physicist.

I would like to thank my other committee members, Professors Greg Fiete, Zhen Yao, and Emanuel Tutuc. Their help was invaluable to me. I also want to thank my other teachers in Austin: Professors Alexander Demkov, Ken Chih-Kang, Jim Chelikowsky, Elaine Li, Keji Lai, Linda Reichl, Duane Dicus, E. C. George Sudarshan, and Steven Weinberg.

It has been great to interact with many members in Qian's and Allan's group, including Yang Gao, Lifa Zhang, Bangguo Xiong; Ashley Da Silva, Yasufumi Araki, Karin Everschor-Sitte, Matthias Sitte, John Tolsma, and Guru Khalsa. I would like to especially thank Hua Chen, Fengcheng Wu, Gaurav Chaudhary, Inti Sodemann, and Rohit Hedge for numerous valuable discussions and interactions.

I would also want to specially thank my colleague and friends Ran Cheng and Ming Xie. We enjoyed a lot of great experiences together, and shared many great memories. It was great to become friends with you.

Quantum Hall effects in novel 2D electron systems: Nontrivial Fermi surface topology and quantum Hall ferromagnetism

Publication No. _____

Xiao Li, Ph.D.
The University of Texas at Austin, 2014

Supervisor: Qian Niu

In this thesis we discuss quantum Hall effects in bilayer graphene and other novel two-dimensional electron systems, focusing on the interplay between nontrivial Fermi surface topology and electron-electron interactions. In the first chapter I will give a brief introduction to some aspects of the quantum Hall effects.

The second chapter discusses the physics in bilayer graphene in the absence of external magnetic fields. The first half discusses the band gap opening and trigonal warping effects in its bandstructure, and the second half focuses on the insulating ground state that results from electron-electron interactions.

The third chapter discusses the single-particle Landau level structure in bilayer graphene. We will see that when both the band gap and trigonal warping effects are present, the highest Landau level in the valence band is

three-fold degenerate at small magnetic fields. As the field increases, the three fold degeneracy is lifted and the Landau level structure gradually reduces to that in the absence of trigonal warping effects. At the end of the chapter we will demonstrate a formalism to map the momentum distribution of the single-particle Landau level structure. Such a mapping will give valuable information about the single-particle bandstructure.

The fourth chapter deals with electron-electron interactions in the integer quantum Hall regime, where there is no fractional filling of the orbital degrees of freedom. In such a regime, the effect of electron-electron interactions often leads to spontaneous ordering of the internal degrees of freedom, such as spin, layer and valley. The first part of the chapter will establish the general formalism of Hartree-Fock theory in the quantum Hall regime, and then a specific theory for gapped bilayer graphene with trigonal warping effects is constructed. The resulting ground states are analyzed in the last part of the chapter.

Table of Contents

Acknowledgments **v**

Abstract **viii**

List of Figures **xiii**

List of Tables **xvi**

Chapter 1. Introduction **1**
1.1 Structure and outline 1

Chapter 2. Material consideration: Few-layer graphene **4**
2.1 Bandstructure of monolayer graphene 4
2.1.1 Lattice structure of monolayer graphene 4
2.1.2 Tight-binding Hamiltonian 6
2.1.3 The continuum limit 7
2.2 Bandstructure of bilayer graphene 8
2.2.1 Lattice structure and tight-binding Hamiltonian 8
2.2.2 Continuum model for bilayer graphene 9
2.2.3 Bandstructure of pristine bilayer graphene 10
2.2.4 Trigonal warping effects 11
2.2.5 Band gap opening in pristine bilayer graphene 13
2.2.6 Band gap opening in the trigonal warping regime 15
2.3 Spontaneous insulating ground states in bilayer graphene . . . 17
2.3.1 Introduction 18
2.3.2 Continuum model mean-field theory 19
2.3.3 Microscopic theory of domain walls 22
2.3.4 Interlayer coherence and domain walls 23
2.3.5 Ising critical temperature estimate 26

2.3.6 Phenomenological theory of domain walls 27
2.3.7 Discussion 28

Chapter 3. Fermi surface topology and Landau levels 32
3.1 Landau level structure in monolayer graphene 32
3.1.1 Landau level structure in gapped Dirac fermions 33
3.2 Landau level structure in bilayer graphene 38
3.2.1 Landau levels in pristine bilayer graphene 38
3.2.2 Gapped bilayer graphene with no trigonal warping . . . 41
3.2.3 Gapped bilayer graphene with trigonal warping 41
3.2.3.1 Estimate of the breakdown 44
3.3 Mapping momentum distributions of Landau levels 44
3.3.1 Formulation 44
3.3.2 Application to the degenerate case 46
3.3.3 Application to cases with higher fields 49

Chapter 4. Quantum Hall ferromagnetism 52
4.1 Hartree-Fock theory in the integer QH regime 52
4.1.1 Coulomb interactions in the quantum Hall regime 53
4.1.2 Density matrix in the quantum Hall regime 54
4.1.3 Hartree-Fock approximation 56
4.2 QH ferromagnetism in bilayer graphene: theory 56
4.2.1 The Hartree energy 58
4.2.2 The exchange energy 58
4.2.2.1 The two integrals 60
4.2.2.2 The structure of $\mathcal{S}^{\lambda\sigma}_{\alpha\beta}$ matrix 61
4.2.3 The full Hartree-Fock Hamiltonian 62
4.3 QH ferromagnetism in bilayer graphene: results 63
4.3.1 Results at $B = 1\,\mathrm{T}$ 63
4.3.1.1 Filling factor $\nu = 1$ 63
4.3.1.2 Filling factor $\nu = 2$ 64
4.3.1.3 Filling factor $\nu = 3$ 66
4.3.1.4 Filling factor $\nu = 4$, $\nu = 5$, and $\nu = 6$ 66
4.3.2 Possible future directions 67

Appendix **68**

Appendix A. Useful results for quantum Hall physics **69**
A.1 LL wavefunctions in the symmetric gauge 69
A.1.1 Working in the symmetric gauge 69
A.1.2 Two sets of creation and annihilation operators 70
A.2 LL wavefunctions in the Landau gauge 73
A.3 Calculation of the pseudopotentials 73
A.3.1 Pseudopotentials in 2DEG: formalism 73
A.3.2 Pseudopotentials in graphene: the pseudospin structure 75
A.3.3 Projected density operator in graphene 75

Appendix B. Form factors in quantum Hall ferromagnetism **77**
B.1 Derivations in the Landau gauge 77
B.2 Derivations in the symmetric gauge 80

Publication List **82**

Bibliography **84**

Vita **96**

List of Figures

2.1 (a) Lattice structure of monolayer graphene. (b) Brillouin zone of both monolayer and bilayer graphene. These two figures are adapted from Ref. [4]. (c) Lattice structure of AB-stacked bilayer graphene. This figure is adapted from Ref. [1]. 5

2.2 Bandstructure of monolayer graphene. (a) Full three-dimensional illustration. (b) A two-dimensional cut, showing the linear dispersion near valley K and K'. 7

2.3 (a) Bandstructure of pristine bilayer graphene along the high symmetry directions. The parameters are taken from Ref. [77]. (b) Full three-dimensional illustration. (b) The low-energy spectrum of bilayer graphene in the limit of $\gamma_3 = \gamma_4 = \Delta = 0$. The bands are labeled by the pair of values (χ, α) in Eq. (2.15). This figure is adapted from Ref. [1]. 11

2.4 Detail of the effect of γ_4 and Δ on the low-energy spectrum near the K point. In each case the solid line represent the labelled tight-binding parameters with $\gamma_3 = 0$, and the dashed lines correspond to $\gamma_3 = \gamma_4 = \Delta = 0$. These parameters are all given in units of eV. The k_x momentum is measured from the K point, and $k_y = 0$ throughout. This figure is adapted from Ref. [1]. 12

2.5 (a) Effect of inclusion of trigonal warping (solid line) in spectrum. The dashed line is for $v_3 = 0$. An asymmetry about $k_x = 0$ is introduced in the spectrum, but electron-hole symmetry persists. The inset shows the very low energy spectrum, and the band overlap of about 2 meV is induced by the trigonal warping. (b) Isoenergetic lines in momentum space for $v_3/v \simeq 0.1$. For $E \simeq 1$ meV, the Fermi surface splits into four pockets. This figure is adapted from Ref. [1]. 12

2.6 Band gap opening in bilayer graphene. The dashed line, solid blue line, and solid red line represent $u/\gamma_1 = 0$, 0.1, and 0.3, respectively. 14

2.7 Contour plot of the valence band in bilayer graphene, obtained from a two-band model. Here we choose $\bar{u} = -0.2$ and $v_3/v = 0.1$. 15

2.8 Characteristic cross sections in the valence band dispersion in bilayer graphene. This figure is adapted from Ref. [58]. 16

2.9 (a) Schematic summary of our domain wall calculations. Two domain walls are oriented along the y direction and the mass changes sign along the x direction. (b)-(c) Typical mean-field solutions for $m_z(x)$ and $m_x(x)$ variation across a domain wall. Note the different scales in (b) and (c). (d) Energy spectrum of a model with sharp domain walls. The gray area is the bulk continuum. Black and gray colors are used to distinguish chiral states localized at the domain walls which propagate in opposite directions, while solid and dashed lines are used to distinguish states with $\langle\sigma_x\rangle < (>) 0$. The two black dots identify the states with $E = \pm|m_0|/\sqrt{2}$. 21

2.10 Microscopic domain wall properties for square simulation cells with side L and a uniform energy gap $2m_0$. In these figures, red dots are numerical data, while the thin solid lines are power-law fits. (a) Condensation energy $E_{\rm c}$ of bilayer graphene (in units $\gamma_1/\mu{\rm m}^2$) as a function of m_0. The dashed line is obtained from microscopic calculations. (b) Domain wall width ξ as a function of m_0. (c) Domain wall energy $E_{\rm DW}$ as a function of L. (d) Domain wall surface tension $J \equiv E_{\rm DW}/L$ (in units of $\gamma_1/0.1\mu{\rm m}^2$) as a function of m_0. The dashed line is the Ginzburg-Landau theory prediction for the domain wall surface tension. (e) and (f) Comparison of the collective ($T_c^{\rm DW}$) and mean-field ($T_c^{\rm MF}$) critical temperatures. 24

2.11 Tight-binding calculation of distinct domain wall zero-mode patterns in gapped bilayer graphene samples with spin-rotational invariance. The red lines denotes the zero modes localized at domain walls between (a) two QAH regions with opposite total Hall conductance, (b) two QVH regions with opposite layer polarization, and (c) a QVH and a QAH region. The gray lines represent the edge states on the outermost zigzag boundaries. 30

3.1 (a) and (b) Electronic band structure near valley K and K'. (c) LL's with $n = 0, 10, ..., 80$ orbitals. (d)-(f) Enlarged view of the LL's in Group I, II, and III in (c). The $n \neq 0$ LL's are broken into $\tau_z s_z = 1$ doublets and $\tau_z s_z = -1$ doublets, due to the SOC and inversion asymmetry. LL crossing occurs between group II and III. The $n_{\rm I} = 0$ LL is spin degenerate and only appears at valley K. The $n_{\rm II}, n_{\rm III} = 0$ LL's are spin-filtered and appear only at valley K'. 36

3.2 Landau levels for a bilayer (left) and monolayer (right) graphene. Brackets (n, τ_z) indicate LL number n and valley index $\tau_z = \pm 1$. In the center the predicted Hall conductivity σ_{xy} (center) as a function of carrier density for bilayer (solid line) is compared to that of a monolayer (dashed line). This figure is adapted from [37]. 39

3.3 Valence band LL structure for gapped bilayer graphene with no bias or trigonal warping. Here we show the first 10 valence band LL's. 40

3.4 Valence band LL structure for gapped bilayer graphene with bias $\bar{u} = 0.2$. Here we show the first 100 LL's in the $\tau_z = -1$ valley. (a) No trigonal warping effects ($\bar{\lambda} = 0$), (b) With trigonal warping effects ($\bar{\lambda} = 0.1$). The various line cuts in the lowest Landau level correspond to the momentum distribution plots discussed later. 42

3.5 Momentum space distribution of the three LLL states at $B = 1\,\mathrm{T}$. Here we show the spin-up components only. Also we used the same set of parameters as fig. 3.4(b). This set of plots corresponds to line cut A in that figure. The energy decreases from left to right. 46

3.6 Making a single-valley state. Here we plot the three states that are localized at a particular valley. They are obtained by making superpositions of the original three degenerate states. 48

3.7 Momentum space distribution of the three LLL states at various B fields. Again we show the spin-up components only. (a)-(c) $B = 2.2\,\mathrm{T}$, (d)-(f) $B = 3.0\,\mathrm{T}$, (g)-(i) $B = 3.5\,\mathrm{T}$. The three sets of plots correspond to line cuts B, C, and D in Fig. 3.4. In addition, in all these plots the energy decreases from left to right within the same group. 49

3.8 Momentum space distribution of the three LLL states at various B fields. Again we show the spin-up components only. (a)-(c) $B = 4.0\,\mathrm{T}$, (d)-(f) $B = 4.8\,\mathrm{T}$, (g)-(i) $B = 10.0\,\mathrm{T}$. The first sets of plots correspond to line cuts E and F in Fig. 3.4, while in the last set the fields are so large that the results should already go back to the case without trigonal warping effects. 50

4.1 Angular dependence of the energy functional in Eq. (4.38). We can see the three minima. 63

4.2 Hartree-Fock ground state at filling factor $\nu = 2$. Panels (a)-(b) correspond to the state $\Psi^{(11)}_{\nu=2}$ and $\Psi^{(12)}_{\nu=2}$, (c)-(d) correspond to $\Psi^{(21)}_{\nu=2}$ and $\Psi^{(22)}_{\nu=2}$, and (e)-(f) correspond to $\Psi^{(31)}_{\nu=2}$ and $\Psi^{(32)}_{\nu=2}$. . . 65

List of Tables

3.1 Coefficients of T_α^λ 47

4.1 Nonzero values of $\mathcal{S}_{\alpha\beta}^{\lambda\sigma}$ at $B = 1\,\mathrm{T}$. 62

Chapter 1

Introduction

In this document I will describe theories and their connections to the experimental observations in the quantum Hall regime of bilayer graphene and other two-dimensional electron systems. These novel two-dimensional electron systems provide us with a much richer arena to explore quantum Hall physics than traditional GaAs quantum wells, because we have multiple ways to tailor the single-particle bandstructure. For example, we are able to tune the bandstructure externally by gates or strain. Also, we can manipulate various internal degrees like spin, valley and layer. Finally we can even make heterostructures out of monolayer building blocks. All these possibilities enable us to engineer new effective interactions among the carries, which will lead to possible new phases of matter in the quantum Hall regime.

1.1 Structure and outline

In this section I will briefly summarize the structure of each chapter.

Chapter 2 discusses the properties of bilayer graphene in the absence of external magnetic fields. After a brief introductory discussion of monolayer graphene, the single-particle bandstructure of bilayer graphene is presented.

The mainly focus is on the band gap opening by an external electric field, and the trigonal-warping effects that become important at low energies. The second part of this chapter contains results from my recent publication [30], where I will discuss how electron-electron interactions in clean bilayer graphene samples can give rise to an insulating ground state at zero temperature, and how such a state is destroyed by thermal excitations when temperature is increased. Such discussions are not only interesting in their own right, but also familiarize the readers with Hartree-Fock theory of electron-electron interactions, which are essential in the discussions of quantum Hall ferromagnetism in Chapter 4.

Chapter 3 discusses the single-particle Landau level structure of monolayer and bilayer graphene. In this chapter I first use monolayer graphene and monolayer molybdenum disulfide as examples to show how to compute the Landau level structure in a family of two-dimensional electron systems. I will then focus on the Landau level structure in bilayer graphene, and discuss how band gap opening and trigonal warping effects modify the Landau level structure. In particular, when both effects are present, the Landau level structure cannot be easily written in a closed form. In such cases, I will show how to use numerical methods to solve the Landau levels. The last part of the chapter discusses how to map the momentum distributions of the single-particle Landau level structure by making projections onto the coherent states. We will see that such mappings provide valuable information of the Landau level structure.

Chapter 4 discusses the effect of electron-electron interactions in the integer quantum Hall regime. This chapter mainly contains unpublished work. It starts with an illustration of how to construct the Hartree-Fock Hamiltonian for electron-electron interactions in the integer quantum Hall regime. This general formalism is then applied to establish a theory for gapped bilayer graphene with trigonal warping effects. The results and their implications for the experiments are discussed in the last section of the chapter.

Chapter 2

Material consideration: Few-layer graphene

In this chapter we are going to review the physics of neutral bilayer graphene and its ABC-stacked multilayer cousins [28, 38, 70, 74]. They are attractive platforms for unconventional two-dimensional electron system physics because flat bare bands cross near their Fermi levels, and because order induces large momentum-space Berry curvatures in their quasiparticle bands. In the first half of the chapter we will review its single-particle bandstructure, including trigonal warping effects, and band gap opening by external electric field. In the second half we will use mean-field theory to demonstrate how electron-electron interaction will drive neutral bilayer graphene into an insulating state at very low temperatures. This discussion will familiarize the readers with Hartree-Fock approximation of electron-electron interactions, which is the key to develop the theory of quantum Hall ferromagnetism.

2.1 Bandstructure of monolayer graphene

2.1.1 Lattice structure of monolayer graphene

The lattice structure of monolayer graphene is shown in Fig. 2.1(a). The unit cell of monolayer graphene contains two inequivalent atoms, labelled

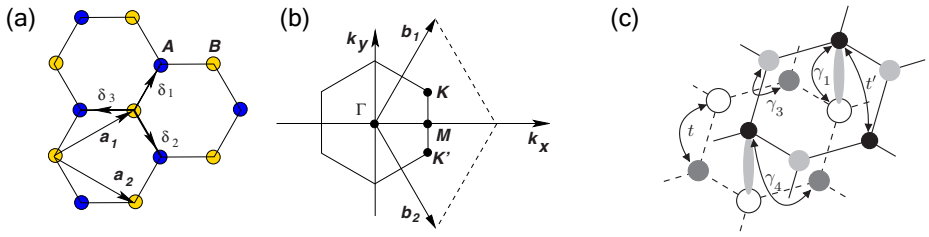

Figure 2.1: (a) Lattice structure of monolayer graphene. (b) Brillouin zone of both monolayer and bilayer graphene. These two figures are adapted from Ref. [4]. (c) Lattice structure of AB-stacked bilayer graphene. This figure is adapted from Ref. [1].

by A and B. The lattice vector can be written as

$$\boldsymbol{a}_1 = \frac{a}{2}(3, \sqrt{3}), \quad \boldsymbol{a}_2 = \frac{a}{2}(3, -\sqrt{3}), \tag{2.1}$$

where $a = 1.42\,\text{Å}$ is the carbon-carbon distance. The three nearest neighbors vectors in real-space are given by

$$\boldsymbol{\delta}_1 = \frac{a}{2}(1, \sqrt{3}), \quad \boldsymbol{\delta}_2 = \frac{a}{2}(1, -\sqrt{3}), \quad \boldsymbol{\delta}_3 = -a(1, 0). \tag{2.2}$$

The Brillouin zone of monolayer graphene is shown in Fig. 2.1(b), and the reciprocal lattice vectors are

$$\boldsymbol{b}_1 = \frac{2\pi}{3a}(1, \sqrt{3}), \quad \boldsymbol{b}_2 = \frac{2\pi}{3a}(1, -\sqrt{3}). \tag{2.3}$$

The K and K' points in the Brillouin zone are of particular importance in the low-energy physics in monolayer graphene. They are called the Dirac points for reasons that will become clear later. Their coordinates in the momentum space are given by

$$\boldsymbol{K} = \frac{2\pi}{3\sqrt{3}a}(\sqrt{3}, 1), \quad \boldsymbol{K}' = \frac{2\pi}{3\sqrt{3}a}(\sqrt{3}, -1). \tag{2.4}$$

2.1.2 Tight-binding Hamiltonian

The tight-binding Hamiltonian for monolayer graphene is given by

$$\mathcal{H} = -t \sum_{\langle i,j\rangle,\sigma} \left(a^\dagger_{i\sigma} b_{j\sigma} + \text{H.c.} \right) - t' \sum_{\langle\langle i,j\rangle\rangle,\sigma} \left(a^\dagger_{i\sigma} a_{j\sigma} + b^\dagger_{i\sigma} b_{j\sigma} + \text{H.c.} \right), \tag{2.5}$$

where $a_{i\sigma}(a^\dagger_{i\sigma})$ annihilates (creates) an electron with spin $\sigma(\sigma =\uparrow,\downarrow)$ on site $\boldsymbol{R}_i$ in sublattice A, and an equivalent definition is used for sublattice B. $t = 2.8\,\text{eV}$ is the energy for hopping between the nearest neighbors, while $t' \simeq 0.1t$ is the energy for hopping between next-nearest neighbors [4]. If we ignore this next-nearest neighbor hopping term, the Hamiltonian for monolayer graphene can be written in the momentum space as

$$\mathcal{H} = \sum_{\boldsymbol{k},\sigma} \begin{pmatrix} a^\dagger_{\boldsymbol{k}\sigma} & b^\dagger_{\boldsymbol{k}\sigma} \end{pmatrix} \begin{pmatrix} 0 & -tf_{\boldsymbol{k}} \\ -tf^*_{\boldsymbol{k}} & 0 \end{pmatrix} \begin{pmatrix} a_{\boldsymbol{k}\sigma} \\ b_{\boldsymbol{k}\sigma} \end{pmatrix}, \tag{2.6}$$

where we have defined

$$f_{\boldsymbol{k}} = e^{i\boldsymbol{k}\cdot\boldsymbol{\delta}_1} + e^{i\boldsymbol{k}\cdot\boldsymbol{\delta}_2} + e^{i\boldsymbol{k}\cdot\boldsymbol{\delta}_3} = e^{-ix} + e^{i\left(\frac{x}{2}+\frac{\sqrt{3}}{2}y\right)} + e^{i\left(\frac{x}{2}-\frac{\sqrt{3}}{2}y\right)}. \tag{2.7}$$

The energy bands derived from the above model have the following form

$$E_\pm(\boldsymbol{k}) = \pm t \sqrt{3 + 2\cos(\sqrt{3}ak_y) + 4\cos\left(\frac{3}{2}ak_x\right)\cos\left(\frac{\sqrt{3}}{2}ak_y\right)}. \tag{2.8}$$

A plot of the monolayer graphene bandstructure is given in Fig. 2.2. We can see that the low energy states locate near the K and K' points in the Brillouin zone, and the band dispersion is linear in this region.

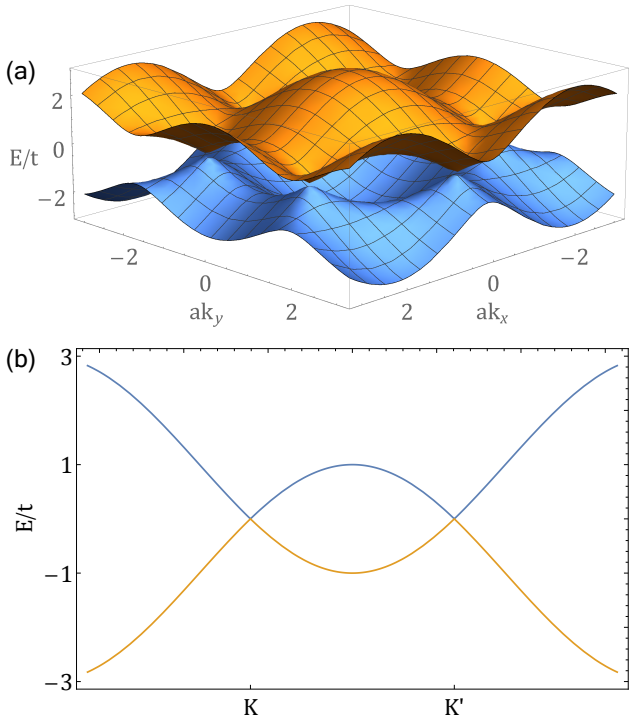

Figure 2.2: Bandstructure of monolayer graphene. (a) Full three-dimensional illustration. (b) A two-dimensional cut, showing the linear dispersion near valley K and K'.

2.1.3 The continuum limit

In fact, we can explicitly demonstrate that the band dispersion is linear near the two valleys. To begin with, we define $x = ak_x$, $y = ak_y$ and assume they are both small. In this case we can expand the exponential functions up to linear in x and y, and obtain

$$f(\tau \boldsymbol{K} + \boldsymbol{k}) \simeq e^{i\tau 2\pi/3}\left[1 + \frac{i}{2}(x + \sqrt{3}y)\right] + e^{-i\tau 2\pi/3}\left[1 + \frac{i}{2}(x - \sqrt{3}y)\right] + (1 - ix)$$
$$= \left(1 + e^{i\tau 2\pi/3} + e^{-i\tau 2\pi/3}\right) + \frac{\sqrt{3}i}{2} y \left(e^{i\tau 2\pi/3} - e^{-i\tau 2\pi/3}\right)$$

$$+\frac{i}{2}x\left(e^{i\tau 2\pi/3}+e^{-i\tau 2\pi/3}-2\right)$$
$$=0-\frac{3}{2}ix-\frac{3}{2}\tau y=-\frac{3}{2}(\tau y+ix)=-\frac{3a}{2}(\tau k_y+ik_x). \tag{2.9}$$

Therefore we have arrived at the low-energy continuum model of monolayer graphene, given by

$$\mathcal{H}=\hbar v\begin{pmatrix}0 & \tau k_x+ik_y\\ \tau k_x-ik_y & 0\end{pmatrix}, \tag{2.10}$$

where we have defined the Fermi velocity $v=3at/2\hbar=1.0\times10^6\,\mathrm{m/s}$, and rotated the coordinate system by $\pi/2$. Such a continuum model is widely used in the literature.

2.2 Bandstructure of bilayer graphene

2.2.1 Lattice structure and tight-binding Hamiltonian

When we stack two layers of graphene on top of each other, we will obtain two different structures, i.e., AA-stacked and AB-stacked bilayer graphene. We will only discuss AB-stacked bilayer graphene in this thesis. The lattice structure of AB-stacked bilayer graphene is shown in Fig. 2.1(c). In this structure, each unit cell contains four different atoms, which we call A_1, B_1, A_2 and B_2. They represent, respectively, the atoms on the A and B sublattice of layer 1 and layer 2. These two layers are stacked in such a way that A_1 atoms are directly on top of the B_2 atoms. We can write down a tight-binding model for AB-stacked bilayer graphene as follows [4],

$$\mathcal{H}=-\gamma_0\sum_{\langle i,j\rangle,l,\sigma}\left(a^\dagger_{m,i,\sigma}b_{m,j,\sigma}+\text{H.c.}\right)-\gamma_1\sum_{j,\sigma}\left(a^\dagger_{1,j,\sigma}a_{2,j,\sigma}+\text{H.c.}\right) \tag{2.11}$$

$$- \gamma_4 \sum_{j,\sigma} \left(a^\dagger_{1,j,\sigma} b_{2,j,\sigma} + a^\dagger_{2,j,\sigma} b_{1,j,\sigma} + \text{H.c.} \right) - \gamma_3 \sum_{j,\sigma} \left(b^\dagger_{1,j,\sigma} b_{2,j,\sigma} + \text{H.c.} \right).$$

In the above model, we use the graphite nomenclature for the various hopping parameters in bilayer graphene. As shown in Fig. 2.1(c), $\gamma_0 = t$ is the in-plane hopping energy; $\gamma_1 = 0.4\,\text{eV}$ is the hopping energy between atoms A_1 and B_2; $\gamma_4 \simeq 0.04\,\text{eV}$ is the hopping energy between atoms $A_1(B_1)$ and atom $A_2(B_2)$; and finally, $\gamma_3 \simeq 0.3\,\text{eV}$ connects A_2 and B_1. For a detailed discussion on the exact values of these parameters, we refer the readers to Ref. [1].

2.2.2 Continuum model for bilayer graphene

Similar to monolayer graphene, we can also obtain a continuum description of bilayer graphene, which is valid for states near the two valleys. This four-band description of bilayer graphene is given by [1, 37]

$$\mathcal{H} = \tau_z \begin{pmatrix} \frac{u}{2} & v_3\pi & v_4\pi^\dagger & v_0\pi^\dagger \\ v_3\pi^\dagger & -\frac{u}{2} & v_0\pi & v_4\pi \\ v_4\pi & v_0\pi^\dagger & -\frac{u}{2} + \tau_z\Delta & \tau_z\gamma_1 \\ v_0\pi & v_4\pi^\dagger & \tau_z\gamma_1 & \frac{u}{2} + \tau_z\Delta \end{pmatrix}. \tag{2.12}$$

In the above model, $\pi = \pi_x + i\pi_y$, $\tau_z = \pm 1$ labels the two valleys, and u is the on-site energy difference between the two layers. $\Delta \simeq 0.015\,\text{eV}$ represent the asymmetry between the two sublattices within each layer, which arises due to the presence of the dimer bond [1]. The various velocities that appear in the above model are converted from the corresponding hopping energies as $v_i = 3a\gamma_i/2\hbar$. We note further that the basis of the above Hamiltonian is different between the two valleys. For $\tau_z = +1$, the basis states are A, $\tilde{B}$, $\tilde{A}$, and B, where $\tilde{A}$ denotes an A atom in the top layer, etc. On the other hand,

for $\tau_z = -1$, the basis states are $\tilde{B}$, A, B, $\tilde{A}$.

Sometimes it is difficult to directly deal with this four-band model, and a low-energy two-band description for bilayer graphene is desired. Such an effective Hamiltonian is given by [1, 37]

$$\mathcal{H}_2 = -\frac{1}{2m}\begin{pmatrix} 0 & (\pi^\dagger)^2 \\ \pi^2 & 0 \end{pmatrix} + h_w + h_a, \quad h_w = \tau_z v_3 \begin{pmatrix} 0 & \pi \\ \pi^\dagger & 0 \end{pmatrix},$$
$$h_a = \tau_z u \left[\frac{1}{2}\begin{pmatrix} 1 & 0 \\ 0 & -1 \end{pmatrix} - \frac{v^2}{\gamma_1^2}\begin{pmatrix} \pi^\dagger\pi & 0 \\ 0 & -\pi\pi^\dagger \end{pmatrix}\right], \tag{2.13}$$

where we have defined $m = \gamma_1/2v^2$, and neglected the v_4 and Δ terms. If we let $\hbar v k_x/\gamma_1 = x$ and $\hbar v k_y/\gamma_1 = y$, the above two-band model can be rewritten conveniently as

$$\mathcal{H}_2/\gamma_1 = \begin{pmatrix} \bar{u}\left(\frac{1}{2} - r^2\right) & \bar{\lambda}(x+iy) - (x-iy)^2 \\ \bar{\lambda}(x-iy) - (x+iy)^2 & -\bar{u}\left(\frac{1}{2} - r^2\right) \end{pmatrix}, \tag{2.14}$$

where $r^2 = x^2 + y^2$, $\bar{u} = \tau_z u/\gamma_1$, $\bar{\lambda} = \tau_z v_3/v$.

2.2.3 Bandstructure of pristine bilayer graphene

The bandstructure of bilayer graphene is shown in Fig. 2.3(a). In the simplest case, with $\gamma_3 = \gamma_4 = \Delta = 0$, the spectrum near the K point is quadratic,

$$E = \chi\sqrt{v_0^2 p^2 + \gamma_1^2/2 + \alpha\gamma_1\sqrt{v^2p^2 + \gamma_1^2/4}}, \tag{2.15}$$

where $\chi = \pm 1$ refers to the conduction and valence band, and $\alpha = \pm 1$ to the low-energy and split branches, as illustrated in Fig. 2.3(b). A cross-over to a linear spectrum occurs at $p \simeq \gamma_1/2v_0$, corresponding to an electron density

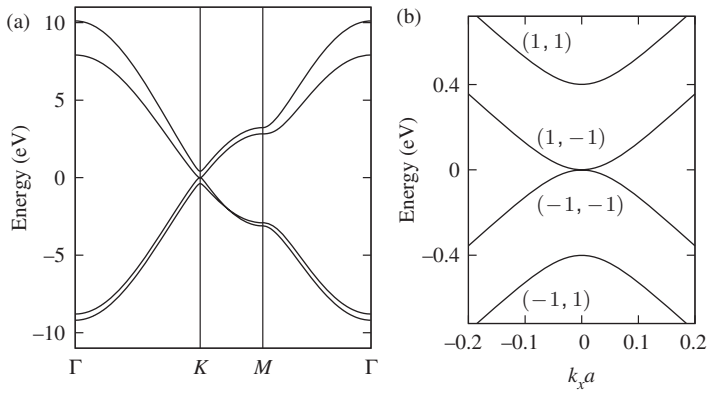

Figure 2.3: (a) Bandstructure of pristine bilayer graphene along the high symmetry directions. The parameters are taken from Ref. [77]. (b) Full three-dimensional illustration. (b) The low-energy spectrum of bilayer graphene in the limit of $\gamma_3 = \gamma_4 = \Delta = 0$. The bands are labeled by the pair of values (χ, α) in Eq. (2.15). This figure is adapted from Ref. [1].

$n^{\rm lin} \simeq \gamma_1^2/(4\pi\hbar^2 v_0^2) \simeq 4 \times 10^{12}\,{\rm cm}^{-2}$ and an energy of $\gamma_1/5$ [37]. This density is lower than the one at which the higher energy band becomes occupied, $n^{(2)} \simeq 2\gamma_1^2/(\pi\hbar^2 v_0^2) \simeq 8n^{\rm lin}$ [37].

We also would like to understand the roles of γ_4 and Δ. Their effects on the bandstructure are shown in Fig. 2.4. We find that γ_4 introduces an electron-hole asymmetry, while Δ increases the conduction band energy near the K point. At larger momentum ($k_x a \sim 0.1$), however, these two effects cancel each other, leaving the bandstructure unchanged.

2.2.4 Trigonal warping effects

The next-nearest neighbor couplings may become important at low energies. In fact the direct coupling between atomic sites not involved in the

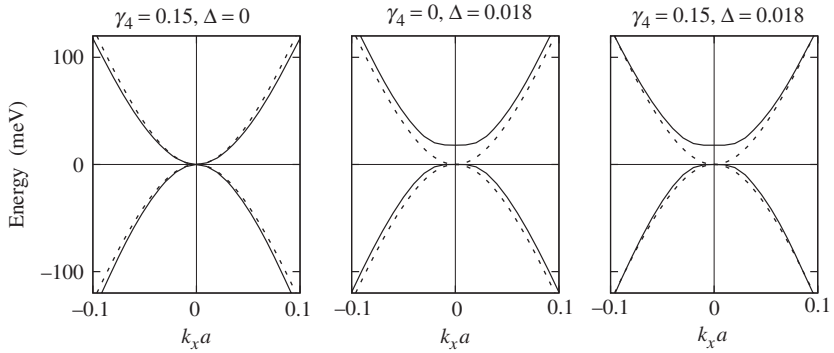

Figure 2.4: Detail of the effect of γ_4 and Δ on the low-energy spectrum near the K point. In each case the solid line represent the labelled tight-binding parameters with $\gamma_3 = 0$, and the dashed lines correspond to $\gamma_3 = \gamma_4 = \Delta = 0$. These parameters are all given in units of eV. The k_x momentum is measured from the K point, and $k_y = 0$ throughout. This figure is adapted from Ref. [1].

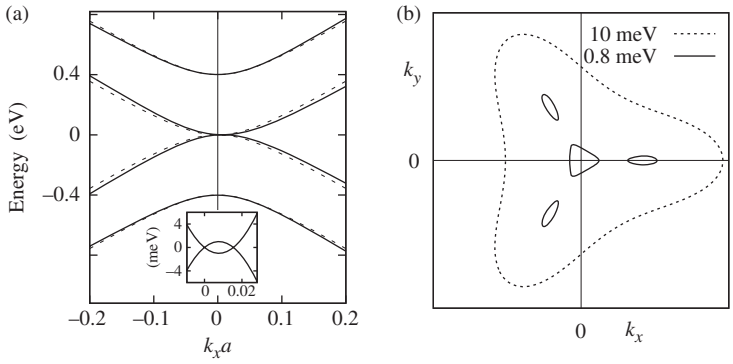

Figure 2.5: (a) Effect of inclusion of trigonal warping (solid line) in spectrum. The dashed line is for $v_3 = 0$. An asymmetry about $k_x = 0$ is introduced in the spectrum, but electron-hole symmetry persists. The inset shows the very low energy spectrum, and the band overlap of about 2 meV is induced by the trigonal warping. (b) Isoenergetic lines in momentum space for $v_3/v \simeq 0.1$. For $E \simeq 1$ meV, the Fermi surface splits into four pockets. This figure is adapted from Ref. [1].

dimer bond, parametrized by γ_3 in Fig. 2.1(c), causes the low-energy spectrum to become anisotropic. This effect is called the trigonal warping effect, and it has a substantial effect on the low-energy properties of bilayer graphene.

A plot of the bandstructure in the trigonal warping regime is shown in Fig. 2.5. We can see that in this regime, the band dispersion is asymmetric about $k_x = 0$, but the particle-hole symmetry is still present, because sublattice symmetry is not broken. For small energies, a Lifshitz transition occurs whereby the Fermi surface breaks into four different pockets: one central region with area $A_c \simeq \pi\epsilon^2/(\hbar v_3)^2$ (ϵ is the band energy), and three elliptical regions with area $A_l \simeq A_c/3$. The center of the three elliptical regions are at momenta with magnitude $\gamma_1 v_3/v^2$ and angles 0, $2\pi/3$, and $4\pi/3$. The electron density at which this Lifshitz transition occurs is $n_L \simeq (v_3/v)^2 n^{\rm lin} \simeq 1\times 10^{11}\,{\rm cm}^{-2}$, where $n^{\rm lin}$ is defined after Eq. (2.15). We further note that the Berry's phase [62] of the central pocket is $-\pi$, while that of each of the three side pockets is π, and therefore preserving the overall Berry's phase of 2π in bilayer graphene [46].

2.2.5 Band gap opening in pristine bilayer graphene

The symmetry governing the degeneracy of the highest valence and lowest conduction bands at the K points in neutral bilayer graphene is the inversion symmetry. If this symmetry is broken, then a gap is expected to appear in the low-energy spectrum. This breaking of symmetry can be modelled within the tight-binding approximation by assuming that the two layers are at different electrostatic potentials, so that the difference between them is pa-

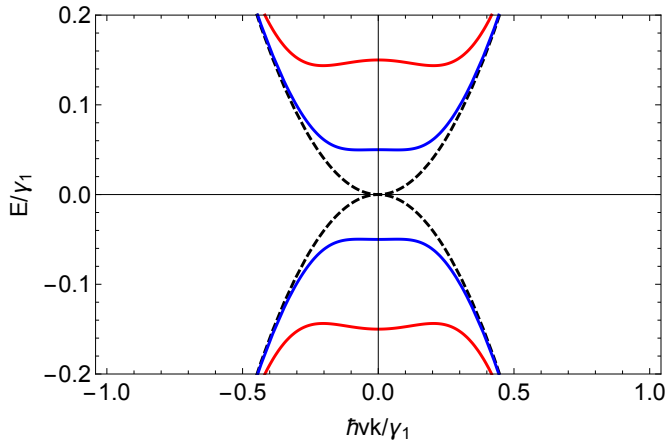

Figure 2.6: Band gap opening in bilayer graphene. The dashed line, solid blue line, and solid red line represent $u/\gamma_1 = 0$, 0.1, and 0.3, respectively.

rameterized by the energy u. This effect is included in the tight-binding model in Eq. (2.12). A plot of bilayer graphene in the presence of interlayer bias is shown in Fig. 2.6. We can see that for modest interlayer bias, a band gap indeed appears at the K point, while the quadratic nature of the low-energy dispersion is retained. However, for higher values of the bias, the quadratic dispersion is replaced by a 'Mexican hat' dispersion [red solid line in Fig. 2.6]. The band dispersion in a minimum model is given by

$$E^2 = v^2p^2 + \gamma_1^2/2 + u^2/4 + \alpha\sqrt{v^2p^2(u^2+\gamma_1^2) + \gamma_1^4/4}, \tag{2.16}$$

where $\alpha = +1$ denotes the split bands, while $\alpha = -1$ denotes the low-energy bands. From this expression we find that the gap exactly at the K point is u, while the minimum separation of the valence and conduction bands is

$$\tilde{u} = \frac{\gamma_1 u}{\sqrt{u^2+\gamma_1^2}}, \tag{2.17}$$

which is located at a momentum of

$$p^2 = \frac{u^2}{4v_0^2}\frac{u^2 + 2\gamma_1^2}{u^2 + \gamma_1^2}. \tag{2.18}$$

We find that for a bias up to $u/\gamma_1 \simeq 0.2$, the band gap is still located at the K point. Finally, in the above discussions we have treated the size of the gap as a phenomenological parameter. In a real experiment, however, the bias potential may not equal to the size of the gap, due to screening effects. Therefore, a self-consistent calculation is needed to obtain the actual band gap. For more discussions on this topic, we refer the readers to Ref. [1].

2.2.6 Band gap opening in the trigonal warping regime

Finally we would like to discuss the bandstructure of gapped bilayer graphene with trigonal warping effects. We will see that in this case the energy bands have a very rich structure.

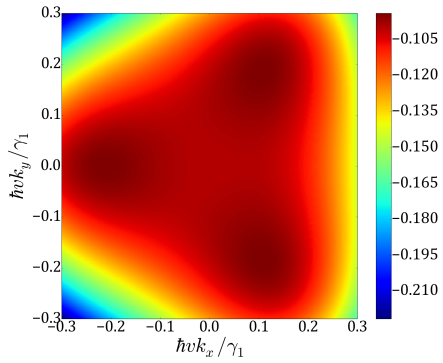

Figure 2.7: Contour plot of the valence band in bilayer graphene, obtained from a two-band model. Here we choose $\bar{u} = -0.2$ and $v_3/v = 0.1$.

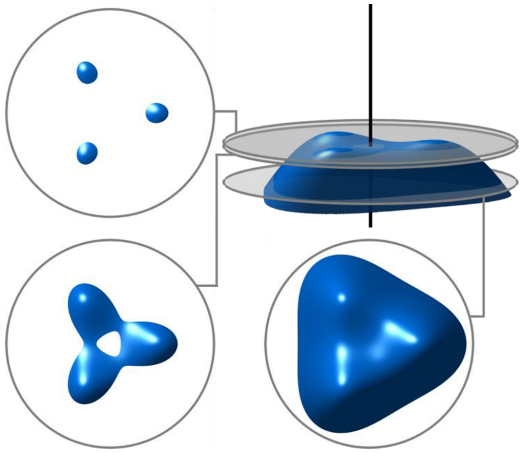

Figure 2.8: Characteristic cross sections in the valence band dispersion in bilayer graphene. This figure is adapted from Ref. [58].

The energy dispersion for the two-band model in Eq. (2.14) is given by

$$\varepsilon^2 = (1+\bar{u}^2)r^4 - 2\bar{\lambda}r^3\cos 3\phi + (\bar{\lambda}^2 - \bar{u}^2)r^2 + \frac{\bar{u}^2}{4}, \tag{2.19}$$

which is plotted in Fig. 2.7. We can see that the top of the valence band is splitter into three separate pockets. When the energy is lowered, they undergo a Lifshitz transition and becomes one piece. This is seen more clearly in Fig. 2.8, where slices of the valence band dispersion are presented.

We now want to find out the location of the three separate Fermi pockets and obtain a low-energy expansion near each point. For valley $K(\tau_z = +1)$, the Fermi pockets locate at directions of $\phi = 0$, $2\pi/3$, and $4\pi/3$, while for valley K', the three Fermi pockets will occur at directions of $\phi = \pi/3$, π, and $5\pi/3$. Their radial distance from the center r_c can be obtained by finding the

minimum of Eq. (2.19) from the following equation,

$$2(\bar{u}^2+1)r_c^2 - 3\bar{\lambda}r_c + (\bar{\lambda}^2 - \bar{u}^2) = 0, \tag{2.20}$$

whose sole solution is

$$r_c = \frac{3\bar{\lambda} + \sqrt{9\bar{\lambda}^2 - 8(1+\bar{u}^2)(\bar{\lambda}^2 - \bar{u}^2)}}{4(\bar{u}^2+1)}. \tag{2.21}$$

Note that this result holds for both valleys.

Now we can expand the energy dispersion near r_c, and find that ε^2 will have the following form,

$$\varepsilon^2 \approx \mathcal{A} + \mathcal{B}r^2, \tag{2.22}$$

where the new r is now measured from r_c, not from zero. The coefficient $\mathcal{B}$ is

$$\mathcal{B} = \frac{8\bar{u}^4 - 8(\bar{\lambda}^2-1)\bar{u}^2 + \bar{\lambda}(\bar{\lambda} + 3\sqrt{\bar{\lambda}^2 + 8\bar{u}^2(1+\bar{u}^2-\bar{\lambda}^2)})}{4(\bar{u}^2+1)}, \tag{2.23}$$

while the coefficient $\mathcal{A}$ is too complicated to show here. From the result in Eq. (2.22), we can see that the low energy dispersion near these Fermi pockets are like massive Dirac fermions, because terms linear in r vanishes exactly. We will see later that this unusual bandstructure has very rich consequences in the quantum Hall regime.

2.3 Spontaneous insulating ground states in bilayer graphene

In this section we are going to discuss the spontaneous insulating ground states in bilayer graphene that have been observed at low temperatures in the

experiments. We will first use mean-field theory to demonstrate that this insulating state could arise due to electron-electron interactions. We further show that as the temperature increases, this insulating state will disappear. We then present two different estimates of this critical temperature and discuss various aspects associated with the phase transition. Most of the results are adapted from my work published in Ref. [30].

2.3.1 Introduction

Theoretical studies have identified a variety of potential broken symmetry states in neutral suspended bilayer graphene [7, 9, 17, 18, 21, 23, 25, 26, 31, 36, 41–44, 49, 51, 53, 54, 56, 57, 65, 66, 70, 71, 73, 75, 78]. The band eigenstates in bilayer graphene are equal weight coherent sums of components localized in each layer, and have an interlayer phase that is strongly wavevector dependent. When lattice-scale corrections to bilayer graphene's massive Dirac model [4,37] are neglected, the broken symmetry states predicted by mean-field theory have a charged quasiparticle energy gap [41, 42, 70, 73, 75] and spontaneous layer polarization within each of the system's four spin-valley flavors, each giving rise to a quantized Hall contribution contribution with magnitude e^2/h. Recent experiments [13, 14, 24, 39, 50, 59, 60, 63, 64] appear to rule out a competing family of nematic states [7, 26, 36, 57], which do not have a quasiparticle gap and break rotational symmetry [10].

The theoretical expectation [18, 41, 44, 65, 70] is that among the gapped broken symmetry states long-range Coulomb interactions should favor the sub-

set with no overall layer-polarization. Recent experiments [14] utilize Zeeman response to an in-plane magnetic field [71] to identify the ground state as either a layer antiferromagnet [70] in which opposite spins have opposite layer polarization, or a quantum spin Hall insulator [44, 70] in which layer polarization changes when either spin or valley is reversed. (In mean-field theories the former state is favored by lattice-scale exchange interactions [18].) In this Letter we present a microscopic theory of domain walls in which the sense of layer polarization of one flavor is reversed, focusing on the unusual properties associated with the ordered states' topological character. These domain walls are expected to be present in disordered bilayer graphene samples because they can be induced by spatial variation in the potential difference between layers. They also proliferate thermally above an Ising phase transition temperature, which we show is substantially suppressed relative to mean-field theory estimates.

2.3.2 Continuum model mean-field theory

We first establish our notation by discussing uniform chiral symmetry breaking in bilayer graphene in terms of the ordered state quasiparticle Hamiltonians [70] suggested by mean-field calculations and renormalization group analyses [18, 31, 41, 42, 49, 71, 73, 75]:

$$\begin{aligned} \mathcal{H}^{HF} &= \sum_{\boldsymbol{k}\alpha\beta ss'} c^{\dagger}_{\boldsymbol{k}\alpha s}\big[h_0 + h_F\big] c_{\boldsymbol{k}\beta s'} \,, \\ h_0 &= -\epsilon_{\boldsymbol{k}}\big[\cos(2\phi_{\boldsymbol{k}})\sigma_x^{\alpha\beta} + \sin(2\phi_{\boldsymbol{k}})\sigma_y^{\alpha\beta}\big]\delta_{ss'} \,, \\ h_F &= -\big[V_0 + V_z\sigma_z^{\alpha\alpha}\sigma_z^{\beta\beta}\big]\ \Delta_{\alpha s}^{\beta s'} \,. \end{aligned} \tag{2.24}$$

Here Greek letters label layer, s and s' label spin, $\epsilon_{\boldsymbol{k}} = (v_{\rm SL}\hbar k)^2/\gamma_1$ is the band dispersion, $v_{\rm SL}$ is the single-layer Dirac-model velocity, γ_1 is the inter-layer hopping energy, $\cot\phi_{\boldsymbol{k}} = \tau_z k_x/k_y$ with $\tau_z = \pm 1$ denoting valley K or K', and $V_{0,z} = (V_s \pm V_d)/2$ is the sum and difference of the same (s) and different (d) layer interactions, which for convenience we assume to be short-ranged. The order parameters $\Delta^{\beta s'}_{\alpha s} = A^{-1}\sum_{\boldsymbol{k}} \langle c^\dagger_{\boldsymbol{k}\beta s'} c_{\boldsymbol{k}\alpha s}\rangle_f$ must be determined self-consistently. Note that in using short-range interactions we are assuming that the screened Coulomb interaction range is short relative to the short-distance cut-off of the two-band continuum model, $v_{\rm SL}\hbar/\gamma_1$, but much larger than the graphene lattice constant. The form used for the mean-field Hamiltonian in Eq. (2.24) has been simplified by noting that the mean-field ground state has no net layer polarization, and that the mean-field interaction vertices are diagonal in layer [71]. This Hamiltonian generates a family of states differing only in the flavor dependence of the sign of interaction-generated mass terms proportional to $m_z\sigma_z$. In this Letter we concentrate on domain walls formed within a single flavor, reserving comments on the role of spin and valley degrees-of-freedom to the end of the article.

The gap equation can be solved to yield an implicit solution for m_z [59]:

$$1 = \nu_0 V_s \int_0^{\gamma_1} \frac{1}{2\varepsilon}[f(-\varepsilon-\mu) - f(\varepsilon-\mu)]d\varepsilon\,, \tag{2.25}$$

where $\nu_0 = \gamma_1/(4\pi\hbar^2 v_{\rm SL}^2)$ is the band density-of-states per flavor, γ_1 is the continuum model ultraviolet cutoff energy, μ is the Fermi energy, $\varepsilon = \sqrt{\epsilon_{\boldsymbol{k}}^2 + m_z^2}$, and $f(\varepsilon) = (1 + e^{\varepsilon/k_BT})^{-1}$ is the Fermi function. For charge-neutral bilayer

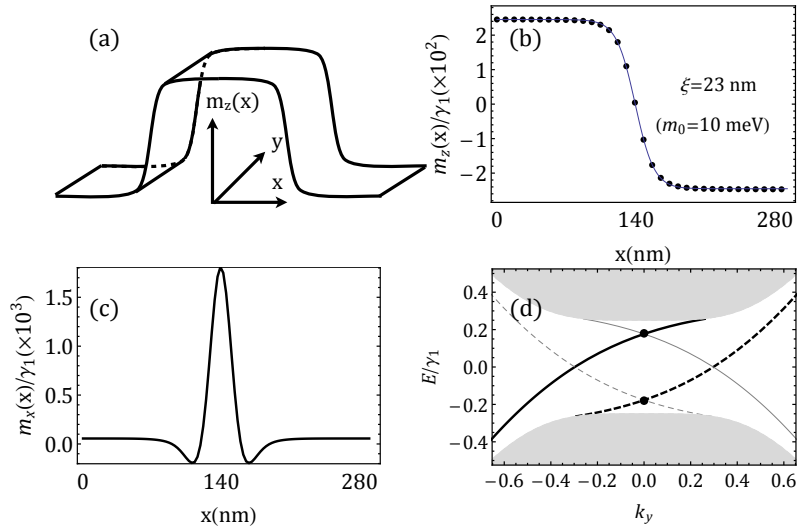

Figure 2.9: (a) Schematic summary of our domain wall calculations. Two domain walls are oriented along the y direction and the mass changes sign along the x direction. (b)-(c) Typical mean-field solutions for $m_z(x)$ and $m_x(x)$ variation across a domain wall. Note the different scales in (b) and (c). (d) Energy spectrum of a model with sharp domain walls. The gray area is the bulk continuum. Black and gray colors are used to distinguish chiral states localized at the domain walls which propagate in opposite directions, while solid and dashed lines are used to distinguish states with $\langle\sigma_x\rangle < (>) 0$. The two black dots identify the states with $E = \pm|m_0|/\sqrt{2}$.

graphene and $m_z \ll \gamma_1$, we find that the quasiparticle gap is

$$2m_z = 4\gamma_1 \exp(-2/V_s\nu_0) \tag{2.26}$$

at zero temperature, and that m_z vanishes at $T = T_c^{\rm MF}$, where

$$T_c^{\rm MF} = e^{\gamma} m_z/\pi k_B, \tag{2.27}$$

and γ is Euler's constant [59].

2.3.3 Microscopic theory of domain walls

We now consider the microscopic electronic structure of the domain walls that separate regions with opposite layer-polarization signs. Because the layer-pseudospin dependent term in the band Hamiltonian is not a small correction to an otherwise pseudospin independent Hamiltonian, it is immediately clear that bilayer graphene domain walls are quite different from those of an ordinary easy-axis ferromagnet. In order to use periodic boundary conditions we must, as illustrated in Fig. 2.9(a), allow for two adequately separated domain walls along the direction in which we allow the sign of mass to change. We use a plane-wave expansion method to solve the spatially inhomogeneous gap equations. The interaction terms in the mean-field Hamiltonian are spatially local and can be parameterized in terms of position dependent masses $m_i(x)$ associated with the three Pauli matrices σ_i. For short-range interactions, their plane-wave matrix elements are

$$m_i(k_1', k_1) = \frac{V_s}{2A} \sum_{f\alpha\beta,\boldsymbol{q}} \langle c^\dagger_{k_1'+q_x,q_y,\alpha} \sigma_i^{\alpha\beta} c_{k_1+q_x,q_y,\beta} \rangle_f \,, \tag{2.28}$$

where $i = x, y, z$, and f labels filled quasiparticle states. Note that the mass terms depend on $k_1' - k_1$ only, and that they are independent of the momentum in the y direction. The inverse Fourier transform with respect to $k_1' - k_1$ specifies $m_i(x)$.

The self-consistent mean-filed equations are readily solved in the presence of domain walls. Results for finite square simulation cells of side L are summarized in Fig. 2.9 and Fig. 2.10. A typical result for the domain

wall m_z profile, plotted in Fig. 2.9(b), can be accurately fit to the form $m_z(x) = m_0 \tanh[(x - x_0)/\sqrt{2}\xi]$, where $2m_0$ is the quasiparticle gap and x_0 is the position of the domain wall center. As illustrated in Fig. 2.10(c), the energy cost of a domain wall $E_{\rm DW}$ in our numerical calculation is accurately proportional to L, indicating that finite-size effects are not playing a large role. Fig 2.10(d) and (b) illustrate our finding that the domain wall energy per unit length (the two-dimensional *surface tension*) $J = E_{\rm DW}/L$ and the domain wall width ξ have power-law dependences on the uniform system mass m_0. An unbiased fit of numerical results to $J \sim m_0^{\alpha}$ and $\xi \sim m_0^{\beta}$ yields $\alpha = 1.72$ and $\beta = -0.36$. These values are close to expectations based on dimensional analysis as we discuss later. We conclude that the surface tension increases and the domain wall width decreases with increasing m_0.

2.3.4 Interlayer coherence and domain walls

The band states of bilayer graphene are coherent combinations [37] of top and bottom layer components with an interlayer phase ϕ that is twice the momentum orientation angle $\phi_{\boldsymbol{k}}$. The m_x and m_y pseudospin magnetizations of both gapped and ungapped states therefore vanish after summing over momenta. As illustrated in Fig 2.9(c), our numerical calculations have revealed that a finite net in-plane pseudospin magnetization develops inside domain walls with a magnitude typically one order smaller than m_0. The in-plane pseudospin magnetization is oriented across the domain wall, *i.e.*, in the x-direction for the geometry we have chosen. Intriguingly, the sign of m_x is

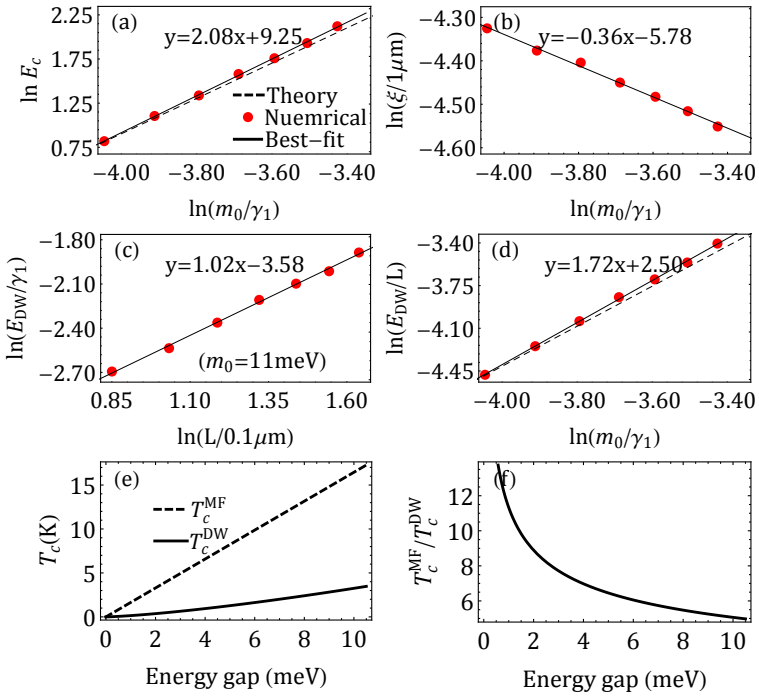

Figure 2.10: Microscopic domain wall properties for square simulation cells with side L and a uniform energy gap $2m_0$. In these figures, red dots are numerical data, while the thin solid lines are power-law fits. (a) Condensation energy E_c of bilayer graphene (in units $\gamma_1/\mu\text{m}^2$) as a function of m_0. The dashed line is obtained from microscopic calculations. (b) Domain wall width ξ as a function of m_0. (c) Domain wall energy E_{DW} as a function of L. (d) Domain wall surface tension $J \equiv E_{\text{DW}}/L$ (in units of $\gamma_1/0.1\mu\text{m}^2$) as a function of m_0. The dashed line is the Ginzburg-Landau theory prediction for the domain wall surface tension. (e) and (f) Comparison of the collective (T_c^{DW}) and mean-field (T_c^{MF}) critical temperatures.

the same for both kink and anti-kink domain walls. The appearance of these in-plane pseudospin components is a surprise since they are not an obvious consequence of spatial dependence of m_z. For example the uniform system m_x and m_y quasiparticle linear response to pseudospin fields in the $\hat{z}$ direction,

characterized by the response functions $\chi_{xz}(\boldsymbol{q})$ and $\chi_{yz}(\boldsymbol{q})$, both vanish identically. As we explain below, the appearance of a nonzero m_x in the domain walls is related to the topological character of the ordered states.

Near a domain wall, the sign of m_z is reversed and the local value of the Hall conductivity changes by two quantized units [35, 70, 72], giving rise to two chiral zero modes per valley propagating along the domain wall, as illustrated in Fig. 2.9(d). As we now explain, we attribute the finite m_x value in the domain wall to the properties of the topological edge states it traps. At any value of k_y the mean-field Hamiltonian $\mathcal{H}$ in the presence of domain walls is invariant under simultaneous rotation by 180° around the pseudospin $\hat{x}$ axis and mirror transformation $x \to -x$ through the domain wall: $\sigma_x \mathcal{H} \sigma_x = \mathcal{H}(-\partial_x, -x)$. Here we assume that $x = 0$ is chosen to lie at the midpoint of a single domain wall. It follows that for any k_y, the two components of the eigenstates $\psi(x) = [u(x), v(x)]^{\mathrm{T}}$ satisfy $v(x) = \pm u(-x)$, and hence that the pseudospin operator σ_x will have a nonzero expectation value near $x = 0$. Similarly since $\sigma_y \mathcal{H}(k_y) \sigma_y = -\mathcal{H}(-k_y)$, if $(u, v)^{\mathrm{T}}$ is an eigenstate of $\mathcal{H}$ at k_y with eigenvalue E, then $(v, -u)^{\mathrm{T}}$ is an eigenstate at $-k_y$ with eigenvalue $-E$. It follows that the two chiral states with $E = 0$ will appear at opposite values of k_y and have opposite expectation values of $\langle \sigma_x \rangle$. For example in the case of a sharp kink, *i.e.*, for $m_z(x) = m_0 \, \mathrm{sgn}(x)$, the chiral states at $k_y = 0$ have $E = \pm |m_0| / \sqrt{2}$ (lying in the gap) and $\langle \sigma_x \rangle = \mp 1$. Although the edge states are not fully polarized in the general case, states within a given chiral state branch have nonzero values of $\langle \sigma_x \rangle$ with a common sign and the edge state

occupations are generically different for any position of the chemical potential within the uniform-state mass gap.

Typical behavior is illustrated in Fig. 2.9(d). The dashed and solid edge state branches have different signs of $\langle \sigma_x \rangle$ and different occupations. As a consequence, $m_x(x)$ exhibits a positive peak at each domain wall center. This in-plane pseudospin magnetization is independent of the domain wall sign and valley index, and thus survives summation over flavors for any gapped broken symmetry state that breaks chiral symmetry within flavors [70]. We note that this nonlinear response also arises near electric field driven domain walls [2, 12, 19, 27, 35, 47, 55, 67, 72] and layer stacking domain walls [2, 55, 72].

2.3.5 Ising critical temperature estimate

We now utilize our numerical results for domain wall properties to estimate the critical temperature T_c^{DW} above which domain walls nucleated by thermal fluctuations proliferate and Ising long-range order within flavors is lost. For this purpose we follow a common physical argument [5] which compares the energy cost associated with domain wall nucleation with the corresponding entropic free energy gain. The energy cost to form a domain wall with perimeter P in the uniform state is JP, whereas the entropy is $k_B \ln C_P$. Here C_P is the number of distinct closed-loop non-intersecting P/W-step walks. For domain walls of width ξ, $W \sim 2\sqrt{2}\xi$ [5] is the minimum distance over which a domain wall can change direction and $C_P = (1+\sqrt{2})^{P/W}$ [5]. It then follows that for temperatures above $T_c^{\mathrm{DW}} = WJ/(k_B \ln(1+\sqrt{2}))$, the proliferation of

domains separating regions with different layer polarization signs is thermodynamically favored and long-range order is lost. Combining our numerical results for ξ and J yields

$$\frac{k_B T_c^{\mathrm{DW}}}{m_0} = \frac{0.64}{\ln(1+\sqrt{2})}(m_0/\gamma_1)^{\alpha+\beta-1}\,. \tag{2.29}$$

Since $\alpha+\beta-1>0$ and $m_0 \ll \gamma_1$, we conclude that $k_B T_c^{\mathrm{DW}} \ll m_0$.

We have so far ignored fermionic thermal fluctuations which produce particle-hole excitations and would limit the critical temperature if the domain wall energy was very large. Because the mean-field theory gap equation is identical to that of BCS theory, it implies a critical temperature limit that is proportional to m_0. As illustrated in Fig. 2.10 (e) and (f), the ratio $T_c^{\mathrm{MF}}/T_c^{\mathrm{DW}}$ decreases with increasing m_0, in agreement with Eq. (2.29). Noting that $\gamma_1 \sim 400\,\mathrm{meV}$ and that experimental [59] values of m_0 in bilayer graphene are always smaller than 4 meV, we conclude that the temperature to which spontaneous layer polarization order survives is limited in practice by domain wall nucleation.

2.3.6 Phenomenological theory of domain walls

The domain wall shape found in our numerical calculations is consistent [5, 52] with the Ising-order Ginzburg-Landau-theory energy functional

$$F = \int d^2\vec{r}\left[\frac{c}{2}(\nabla m_z)^2 + \mathcal{V}[m_z(x)] - E_c\right], \tag{2.30}$$

where $\mathcal{V}[m_z] = -r m_z(x)^2/2 + u m_z(x)^4$ with both r and u positive, and $E_c = -r^2/16u$ is the condensation energy per unit area of a ground state with uniform m_z.

We include the constant E_c in this expression so that the minimum value of F, which occurs for constant masses $m_z^* = \pm m_0 = \pm(r/4u)^{1/2}$, is zero. For a single domain wall configuration in which $m_z \to \pm m_0$ for $x \to \pm\infty$, the functional (2.30) is minimized by $m_z(x) = \pm m_0 \tanh[(x-x_0)/\sqrt{2}\xi]$ with $\xi = \sqrt{c/r}$. The close agreement between our numerical domain wall shapes and this analytic expression demonstrates that the Ginzburg-Landau theory for spontaneously gapped states in bilayer graphene is of the standard Ising magnetism form, in spite of the unusual microscopic physics. The Ginzburg-Landau model reproduces microscopic values for m_0, ξ, and E_c when we set $c = 4E_c\xi^2/m_0^2$, $r = 4E_c/m_0^2$, and $u = E_c/m_0^4$. (Note that m_0 is strongly temperature dependent for a given value of the interaction strength.) In Fig. 2.10(a) we demonstrate that the Ginzburg-Landau theory expression for the domain wall surface tension $J = 8\sqrt{2}\xi E_c/3$ agrees accurately with our microscopic calculations, and that the power laws relating ξ and J to the microscopic gap satisfy $\alpha - \beta = 2$, also in agreement with the GL theory.

2.3.7 Discussion

It is instructive to compare spontaneously gapped bilayer graphene with BCS superconductors. In both cases mean-field theory predicts a critical temperature that is linear in the the gap parameter m_0. Fluctuation effects differ qualitatively in the two cases, however, in the first place because of the difference between the order parameter dimensions. In superconductors the excitations whose proliferation limits the critical temperature are vortices rather

than domain walls. Additionally the free fermion dispersion is linear near the Fermi energy in the superconductor case but *quadratic* in bilayer graphene. As a result, the coherence length in superconductors is related to the gap Δ by $\xi \sim \hbar v_{\rm SL}/\Delta$, and the collective fluctuation limit on the critical temperature must therefore exceed the nucleation energy of a vortex, *i.e.*, $k_B T_c \sim E_c \xi^2 \sim \varepsilon_F$ which is independent of and much larger than the mean-field critical temperature estimate. A similar estimate of the collective limit on T_c can be obtained by appealing to Kosterlitz-Thouless theory. These considerations explain why critical temperatures of weakly disordered superconducting thin films is still accurately predicted by mean-field theory, even though the phase transition is ultimately of Kosterlitz-Thouless character. In bilayer graphene on the other hand, the relationship between ξ and the gap can be estimated using $m_0 \sim (\hbar v_{\rm SL}/\xi)^2/\gamma_1$. This estimate yields $\beta = -0.5$, in rough agreement with the value $\beta = -0.36$ obtained by fitting our numerical results. It follows that for bilayer graphene, collective fluctuations limit the critical temperature to a value that is substantially lower than the mean-field-theory estimate. Unlike the case of superconductors, in bilayer graphene thermal fluctuations in the order parameter configuration play an important role in limiting the critical temperature.

When the four spin-valley flavors are taken into account, the $2^4 = 16$ gapped broken symmetry states that are close in energy [18] can be classified into five distinct phases [70]. This in turn leads to 16 distinct types of domain walls. In Fig. 2.11 we illustrate the cases in which spin rotational invariance

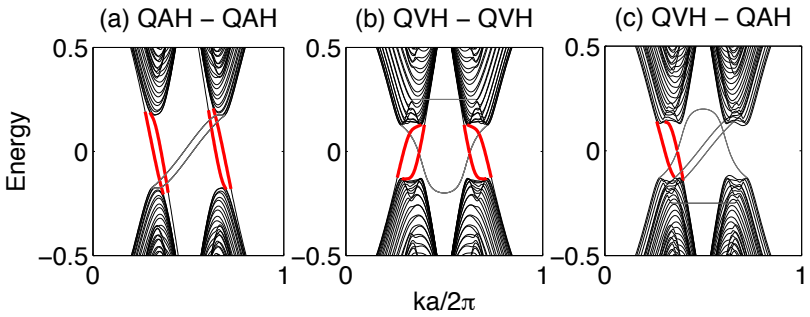

Figure 2.11: Tight-binding calculation of distinct domain wall zero-mode patterns in gapped bilayer graphene samples with spin-rotational invariance. The red lines denotes the zero modes localized at domain walls between (a) two QAH regions with opposite total Hall conductance, (b) two QVH regions with opposite layer polarization, and (c) a QVH and a QAH region. The gray lines represent the edge states on the outermost zigzag boundaries.

is not broken, and only the quantum valley Hall (QVH) state and quantum anomalous Hall (QAH) state are allowed. Because in the absence of intervalley scatterings the valley-projected Chern numbers are quantized [27,35,70,72] to ± 1, all domain walls support edge states, as shown in Fig. 2.11. At a domain wall separating two QAH regions with opposite total Hall conductances, as illustrated in Fig. 2.11(a), the Chern number changes have the same sign for both valleys, yielding four modes with the same chirality. At a domain wall separating two QVH regions with opposite layer polarization, the Chern numbers change by ± 2, with opposite signs for opposite valleys. Thus two chiral zero modes (per spin) appear at valley K and two with opposite chirality at the valley K', as illustrated in Fig. 2.11(b). This type of domain wall can be easily realized using an external electric field [2,12,19,27,35,47,55,67,72] or a stacking fault [2,55,67,72]. Finally, at the domain wall between a QVH and

a QAH regions the Chern number is changed by two for one valley while it is unchanged for the other. Thus the zero modes at the domain wall are chiral in one valley and absent in the other. In all these cases, edge modes have a double spin-degeneracy. States in which spin-rotational invariance is also broken can be similarly analyzed. Each of the 16 types of domain wall hosts a Luttinger liquid [22] with distinct properties. Our work therefore suggests that large-area bilayer graphene gapped states should exhibit interesting transport anomalies. Similar phenomena will occur in thicker ABC-stacked few-layer [70] graphene systems which have larger spontaneous gaps [24, 39] and more robust domain walls.

Chapter 3

Fermi surface topology and Landau levels

In this chapter we would like to use bilayer graphene as an example to discuss Landau level structure in materials with nontrivial Fermi surface topology. We will first review the Landau level structure in pristine bilayer graphene, and then discuss its variations in the presence of a band gap and trigonal warping effects. Finally we will discuss how to compute the Landau level structure using semiclassical theory.

3.1 Landau level structure in monolayer graphene

In this section we would like to derive the Landau level structure for monolayer graphene. Most of the results we used are discussed in more detail in Appendix A, and we will just quote without proof here. In the Landau gauge $\boldsymbol{A} = (0, Bx)$, the single-particle Hamiltonian for graphene in the presence of perpendicular magnetic fields reads

$$\mathcal{H}_K = \frac{\sqrt{2}\hbar v}{\ell}\begin{pmatrix} 0 & a^\dagger \\ a & 0 \end{pmatrix}, \quad \mathcal{H}_{K'} = \frac{\sqrt{2}\hbar v}{\ell}\begin{pmatrix} 0 & -a \\ -a^\dagger & 0 \end{pmatrix}, \tag{3.1}$$

where $\ell = \sqrt{\hbar/eB} = 26.5\,\mathrm{nm}/\sqrt{B[\mathrm{T}]}$ is the magnetic length. As a result, the Landau level energies are given by $E_{n,\pm} = \pm\sqrt{2e\hbar v^2 nB}$. This energy is the

same for both valleys, therefore each of the Landau level is four-fold degenerate in graphene (including spin).

The wave function for the lowest Landau level ($n = 0$) is given by

$$\phi_{0,K} = \begin{pmatrix} 0 \\ \phi_0 \end{pmatrix}, \quad \phi_{0,K'} = \begin{pmatrix} \phi_0 \\ 0 \end{pmatrix}. \tag{3.2}$$

For Landau levels with $n \neq 0$, the wave functions are given by

$$\phi_{n,K} = \frac{1}{\sqrt{2}} \begin{pmatrix} \phi_n \\ \phi_{n-1} \end{pmatrix}, \quad \phi_{n,K'} = \frac{1}{\sqrt{2}} \begin{pmatrix} \phi_{n-1} \\ \phi_n \end{pmatrix}. \tag{3.3}$$

In the above equations, the function ϕ_n is the harmonic oscillator wave function, given by

$$\phi_n \equiv \phi_n(x - X) = \sqrt{\frac{1}{2^n n! \sqrt{\pi}\ell}} e^{-(x-X)^2/2\ell^2} H_n\left(\frac{x - X}{\ell}\right), \tag{3.4}$$

where $X = k_y \ell^2$ is the guiding center of the cyclotron motion, and $H_n(x)$ is the Hermite polynomial.

3.1.1 Landau level structure in gapped Dirac fermions

In this section we are going to discuss Landau levels in gapped Dirac fermions, using monolayer molybdenum disulfide (MoS_2) as an example. Some of the results in this section are adapted from my work published in Ref. [29].

We start from a description of the low-energy model of an isolated monolayer MoS_2, which applies generally to other group-VI dichalcogenides with the same crystal structure. The top and bottom S layers and the middle Mo layer are parallel triangular lattices. Because of their ABA relative stacking

order, the top view of this trilayer forms a honeycomb lattice with S and Mo atoms at A and B sites, respectively. Near the Brillouin zone inequivalent corners K and K', the conduction and valence band states are approximately from $|\phi_c\rangle = |d_{z^2}\rangle$ and $|\phi_v^{\tau_z}\rangle = (|d_{x^2-y^2}\rangle + i\tau_z|d_{xy}\rangle)/\sqrt{2}$ orbitals, respectively. This effective two-band model has been suggested by DFT calculations [61] and supported by optical experiments [3, 34, 48, 69]. To linear order in p, the effective $k\cdot p$ Hamiltonian in the above basis reads

$$\mathcal{H} = v(p_x\tau_z\sigma_x + p_y\sigma_y) + \Delta\sigma_z - \lambda\tau_z s_z\sigma_z + \lambda\tau_z s_z\,, \tag{3.5}$$

where the Pauli matrices $\boldsymbol{\sigma}$ operate on the space of the d_{z^2} and $d_{x^2-y^2} + id_{xy}$ orbitals, $\tau_z = \pm 1$ labels the K and K' valleys, and $s_z = \pm 1$ denotes the electron spin $\uparrow$ and $\downarrow$. The Fermi velocity v is $at/\hbar \sim 0.53 \times 10^6\,\mathrm{m/s}$, where t is the effective hopping between the two Mo d-orbitals mediated by the S p-orbitals. As anticipated, the inversion asymmetry [1] between d_{z^2} and $d_{x^2-y^2} + id_{xy}$ orbitals gives rise to the $\Delta\sigma_z$ mass term which pins the ground state to a quantum valley Hall (QVH) insulator [45, 70]. Mo atoms provide strong intrinsic SOC $\sim \tau_z s_z \sigma_z$ [20, 70] that adjusts the energy gaps to $2(\Delta - \lambda)$ for $\tau_z s_z = 1$ bands and to $2(\Delta + \lambda)$ for $\tau_z s_z = -1$ bands. Note that this SOC perturbation preserves inversion ($\mathcal{P} = \tau_x\sigma_x$) and time reversal ($\mathcal{T} = i\tau_x s_y K$) symmetries. As a combined effect of broken inversion symmetry and strong SOC, the term $\lambda\tau_z s_z$ breaks the particle-hole symmetry by oppositely shifting

[1] Here the orbital inversion symmetry is analogous to the parity inversion symmetry in graphene. For a monolayer MoS_2, this symmetry is only well defined in the low-energy model and is irrelevant in any lattice models.

the $\tau_z s_z = \pm 1$ bands. Using $\Delta = 830\,\text{meV}$ and $\lambda = 37.5\,\text{meV}$ extracted from DFT calculations [61], Fig. 3.1 plots the band structure of a monolayer MoS_2 which exhibits two features that substantially differ from graphene, i.e., (i) a large QVH band gap and (ii) a lifted degeneracy between $\tau_z s_z = \pm 1$ bands. While the conduction band bottoms are lined up for all flavors, the valence band tops have a significant shift in energy between $\tau_z s_z = \pm 1$ bands. These symmetry breaking and spin-valley coupling can be further verified by the flavor-dependent energy dispersions

$$E_\pm = \lambda \tau_z s_z \pm \sqrt{v^2 p^2 + (\Delta - \lambda \tau_z s_z)^2}\,, \tag{3.6}$$

where $\pm$ stands for the conduction and valence bands.

In the presence of a uniform perpendicular magnetic field, the 2D kinetic momentum $\boldsymbol{p}$ in Eq. (3.5) is replaced by $\boldsymbol{\pi} = \boldsymbol{p} + e\boldsymbol{A}/c$. In the Landau gauge $\boldsymbol{A} = (0, Bx)$, the operators $\pi = \pi_x + i\pi_y$ coincide with the lowering operators, satisfying $\pi\phi_n = -i(\hbar/\ell_B)\sqrt{2n}\phi_{n-1}$ and $\pi\phi_0 = 0$. Here $\ell_B = \sqrt{\hbar/(eB)} = 25.6/\sqrt{B[\text{T}]}\,\text{nm}$ is the magnetic length and ϕ_n is the nth LL eigenstate of an ordinary 2DEG. This model is approximately valid when $\hbar v/\ell_B$ is smaller than the band width ~ 300 meV. To focus on the influences from SOC and inversion asymmetry on the LL's, the relatively smaller effects including Zeeman couplings, disorders and Coulomb interactions are neglected. We obtain the flavor-dependent LL spectrum

$$E_{n,\pm} = \lambda \tau_z s_z \pm \sqrt{n\hbar^2\omega_c^2 + (\Delta - \lambda \tau_z s_z)^2}\,, \tag{3.7}$$

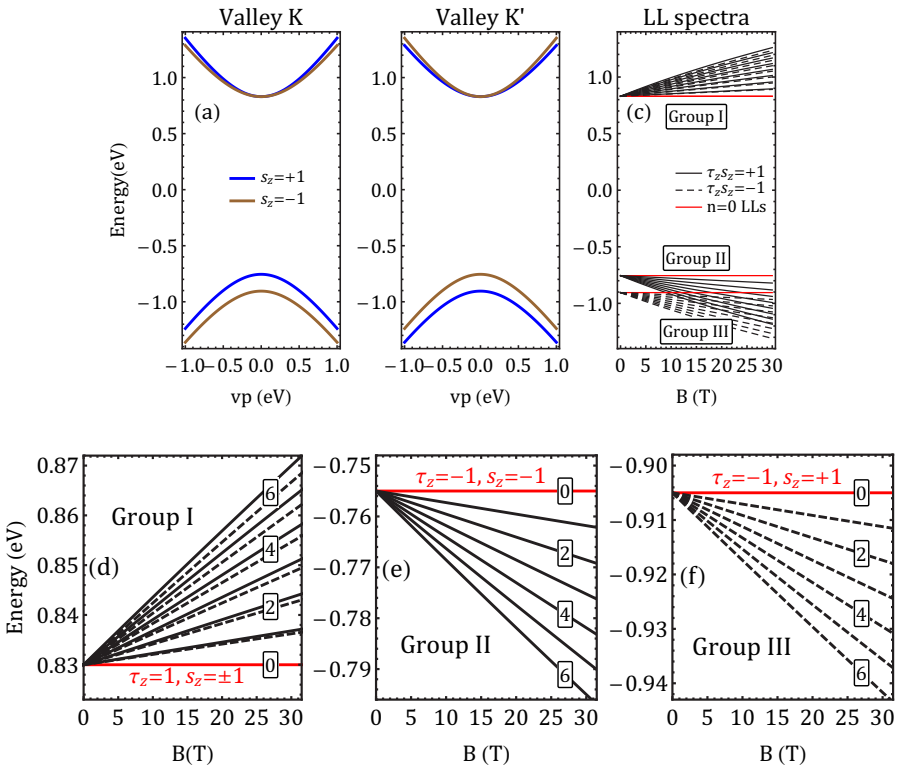

Figure 3.1: (a) and (b) Electronic band structure near valley K and K'. (c) LL's with $n = 0, 10, ..., 80$ orbitals. (d)-(f) Enlarged view of the LL's in Group I, II, and III in (c). The $n \neq 0$ LL's are broken into $\tau_z s_z = 1$ doublets and $\tau_z s_z = -1$ doublets, due to the SOC and inversion asymmetry. LL crossing occurs between group II and III. The $n_{\rm I} = 0$ LL is spin degenerate and only appears at valley K. The $n_{\rm II}, n_{\rm III} = 0$ LL's are spin-filtered and appear only at valley K'.

where $\omega_c = \sqrt{2}v/\ell_B$ is the cyclotron frequency. The corresponding eigenstates with $n > 0$ can be formally written as $(\phi_n, a^{\pm}_{n,s_z}\phi_{n-1})^T$ for valley K and $(b^{\pm}_{n,s_z}\phi_{n-1}, \phi_n)^T$ for K'. For $n = 0$ LL's, the eigenstates are $(\phi_0, 0)^T$ with energy Δ and $(0, \phi_0)^T$ with energy $-\Delta - 2\lambda s_z$. This shows that the $SU(4)$ invariant four anomalous $n = 0$ LL's are broken into a two-fold spin-degenerate conduc-

tion band $n_{\rm I} = 0$ LL at valley K and two spin-split valence band $n_{\rm II}, n_{\rm III} = 0$ LL's at K', as shown in Fig. 3.1(c), leading to quantum Hall effects at $\nu = 0$ and $\nu = -1$ but not $\nu = 1$. This is reminiscent of the anomalous $n = 0$ LL's in few-layer graphene systems [76]. In graphene the $SU(4)$ symmetry of $n = 0$ LL's are completely lifted by electron-electron interactions [6, 11, 68] while the particle-hole symmetry remains, whereas in the monolayer MoS_2 both the $SU(4)$ and particle-hole symmetries are broken by the intrinsic SOC and the inversion asymmetry.

Other unconventional LL features can be visualized in Fig. 3.1(c) and further understood by expanding Eq. (3.7) at $nB < 50\,\mathrm{T}$ as follows,

$$E_{n,\alpha} = (2\lambda\tau_z s_z \delta_{\alpha,-} + \alpha\Delta) + \frac{e\hbar v^2}{\Delta - \lambda\tau_z s_z} nB, \tag{3.8}$$

with $\alpha = \pm$. (i) Because of the heavily massive Dirac Fermion character, LL energies grow *linearly* with B, rather than with $\sqrt{B}$. (ii) SOC break the LL's into two groups with $\tau_z s_z = \pm 1$. However, each $n \neq 0$ LL is still doubly degenerate in each group, consisting of one spin $\uparrow$ state from one valley and one spin $\downarrow$ state from the other valley. (iii) The energies of two group LL's in the valence band not only have different slopes in B but also shift rigidly at $B = 0$, leading to LL crossing effects at

$$B_c = \frac{4\lambda(\lambda + \Delta)}{e\hbar v^2 (n_{\rm II} - n_{\rm III})} + \frac{8\lambda^2 n_{\rm III}}{e\hbar v^2 (n_{\rm II} - n_{\rm III})^2}\,, \tag{3.9}$$

where $n_{\rm II}$ and $n_{\rm III}$ are the LL orbitals for Group II ($\tau_z s_z = 1$) and Group III ($\tau_z s_z = -1$) shown in Fig. 3.1(c).

3.2 Landau level structure in bilayer graphene

In this section we are going to study the single-particle Landau level structure in bilayer graphene, using the two-band model derived in Eq. (2.13). To begin with, we rewrite the two-band Hamiltonian in Eq. (2.13) in a dimensionless form as follows,

$$\mathcal{H}/\gamma_1 = \begin{pmatrix} \bar{u}(\frac{1}{2} - \epsilon_0^2 a^\dagger a) & \bar{\lambda}\epsilon_0 a - \epsilon_0^2 \left(a^\dagger\right)^2 \\ \bar{\lambda}\epsilon_0 a^\dagger - \epsilon_0^2 a^2 & -\bar{u}(\frac{1}{2} - \epsilon_0^2 a a^\dagger) \end{pmatrix}, \tag{3.10}$$

where we have defined $\epsilon_0 = \sqrt{2}\hbar v/\gamma_1 \ell \simeq 0.09\sqrt{B[\mathrm{T}]}$. In the following we will first study the simplest case, where there is neither band gap nor trigonal warping effects. We will see that in this limit the lowest Landau level in bilayer graphene is eight-fold degenerate. We will then add the band gap and discuss how the zeroth Landau level shifts with the band gap. Finally, we will restore the trigonal warping terms. In this case the Fermi surface topology becomes very rich, and we will study how it manifest itself in the Landau level structure.

3.2.1 Landau levels in pristine bilayer graphene

We first discuss the simplest case by letting both $\bar{u}$ and $\bar{\lambda}$ vanish. In this case, the Hamiltonian in valley K reads

$$\mathcal{H}_K/\gamma_1 = -\epsilon_0^2 \begin{pmatrix} 0 & \left(a^\dagger\right)^2 \\ a^2 & 0 \end{pmatrix}. \tag{3.11}$$

We can then obtain the Landau level structure as follows. For the $n = 0$ and $n = 1$ Landau levels we have

$$E_0 = 0, \qquad\qquad E_1 = 0,$$

$$\Phi_0^\intercal = \begin{bmatrix} \phi_0 & 0 \end{bmatrix}, \qquad \Phi_1^\intercal = \begin{bmatrix} \phi_1 & 0 \end{bmatrix}. \tag{3.12}$$

As in monolayer graphene, each of these Landau levels is four-fold degenerate due to spin and valley. As a result, the zero-energy Landau level in pristine bilayer graphene is eight-fold degenerate. Such a structure will be reflected in the Hall conductivity dependence on carrier density $\sigma_{xy}(N)$, which is shown in Fig. 3.2. We can see that near charge neutrality, Hall plateau in bilayer graphene will undergo a jump of $8e^2/h$, which is a manifest of the 2π Berry phase in its bandstructure [46].

This eight-fold degeneracy of the zero-energy Landau level is unusual in two-dimensional systems. We expect that it may have important consequences in the presence of electron-electron interactions [33].

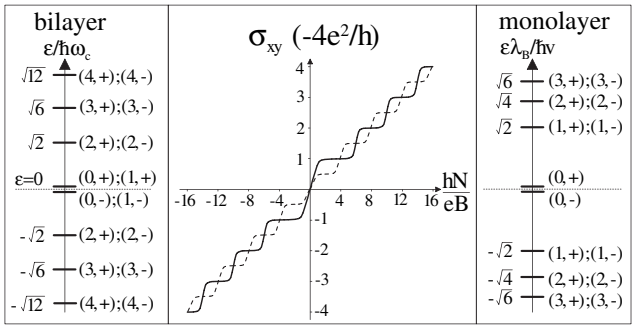

Figure 3.2: Landau levels for a bilayer (left) and monolayer (right) graphene. Brackets (n, τ_z) indicate LL number n and valley index $\tau_z = \pm 1$. In the center the predicted Hall conductivity σ_{xy} (center) as a function of carrier density for bilayer (solid line) is compared to that of a monolayer (dashed line). This figure is adapted from [37].

For $|n| \geq 2$, the Landau level energies of bilayer graphene are given by

$$E_{n,\pm} = \mathrm{sgn}\,(n)\hbar\omega_c\sqrt{|n|(|n|-1)}, \tag{3.13}$$

where $\omega_c = eB/m = 2eB\hbar v^2/\gamma_1$ is the cyclotron frequency in bilayer graphene, and the corresponding wave functions are

$$\Phi^{\intercal}_{|n|\geq 2} = \frac{1}{\sqrt{2}} \begin{bmatrix} \phi_{|n|} & \text{sgn}\,(n)\phi_{|n|-2} \end{bmatrix} . \tag{3.14}$$

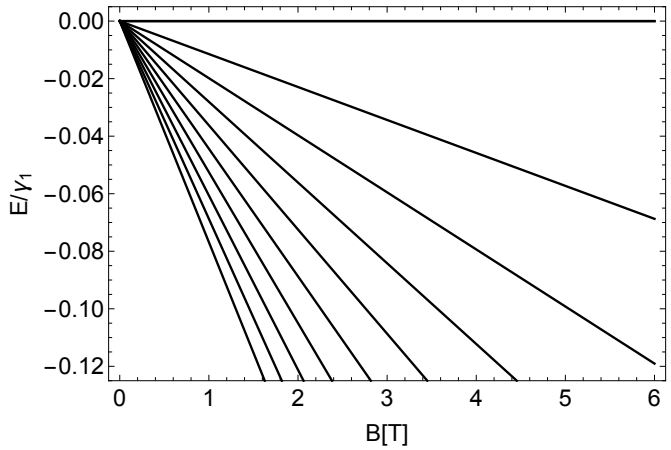

Figure 3.3: Valence band LL structure for gapped bilayer graphene with no bias or trigonal warping. Here we show the first 10 valence band LL's.

The Landau level structure in this simple case is plotted in Fig. 3.3. Because the system has particle-hole symmetry, we only show the valence band Landau levels. The magnetic field dependence of these levels are entirely contained in $\omega_c = eB/m$, so that these Landau levels grow linearly with the perpendicular magnetic field, which is difference from the $\sqrt{B}$ dependence of monolayer graphene Landau levels. In addition, Landau levels with different index n are nearly equally spaced, except for the first few Landau levels. This is reminiscent of the Landau level structure in free electrons.

3.2.2 Gapped bilayer graphene with no trigonal warping

If we include the interlayer bias term but no trigonal warping, the Landau level structure in bilayer graphene can still be obtained exactly as follows. First of all, the $n = 0$ and $n = 1$ LL's have the following energies,

$$\begin{aligned} E_0 &= \frac{\bar{u}}{2}, & E_1 &= \frac{\bar{u}}{2}(1 - 2\epsilon_0^2), \\ \Phi_0^\intercal &= \begin{bmatrix} \phi_0 & 0 \end{bmatrix}, & \Phi_1^\intercal &= \begin{bmatrix} \phi_1 & 0 \end{bmatrix}. \end{aligned} \tag{3.15}$$

Note that these energies are explicitly proportional to the valley index τ_z, so that these two levels appear in the conduction (valence) band in valley $\tau_z = +1(-1)$. For all LL's with $n \geq 2$, we have the following energies

$$E_{n\geq 2} = \frac{1}{2}\left[-\bar{u}^2\epsilon_0^2 \pm \sqrt{4n(n-1)\epsilon_0^4 + \bar{u}^2[(2n-1)\epsilon_0^2 - 1]^2}\right]. \tag{3.16}$$

The corresponding wave functions are

$$\Phi_{n\geq 2}^\intercal = \begin{bmatrix} A_n\phi_n, & B_n\phi_{n-2} \end{bmatrix}, \tag{3.17}$$

where ϕ_n is the usual Harmonic oscillator wave functions, and the coefficients A_n and B_n can be obtained easily. We note that in the limit of $\bar{u} = 0$, the LL structure is reduced to the result we derived in Eq. (3.13). A plot of the valence band LL structure in valley $\tau_z = -1$ is given in Fig. 3.4(a).

3.2.3 Gapped bilayer graphene with trigonal warping

In the presence of the trigonal warping term, the LL structure cannot be solved exactly. We have to obtain it numerically instead. We assume that

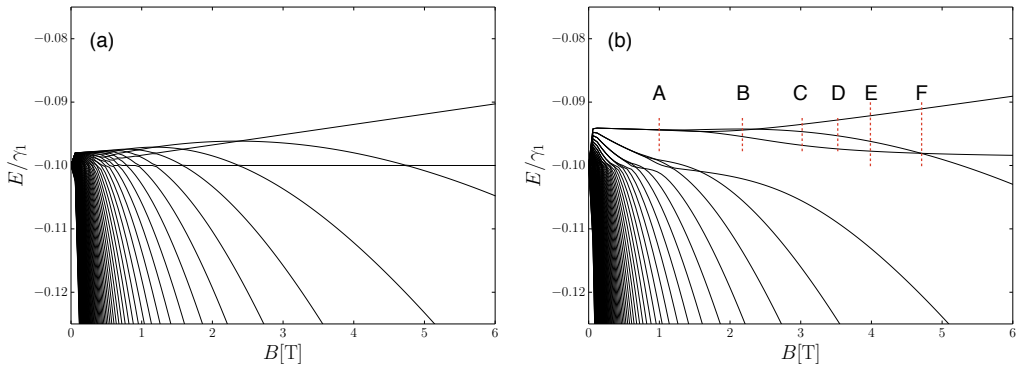

Figure 3.4: Valence band LL structure for gapped bilayer graphene with bias $\bar{u} = 0.2$. Here we show the first 100 LL's in the $\tau_z = -1$ valley. (a) No trigonal warping effects ($\bar{\lambda} = 0$), (b) With trigonal warping effects ($\bar{\lambda} = 0.1$). The various line cuts in the lowest Landau level correspond to the momentum distribution plots discussed later.

the wave function is given by

$$\Phi^{\mathsf{T}} = \left[\sum_{n=0}^{N} A_n \phi_n, \quad \sum_{n=0}^{N-2} B_n \phi_n \right], \tag{3.18}$$

where N is some cutoff we choose. The eigenvalue problem yields the following equations,

$$\begin{aligned} EA_0\phi_0 &= \frac{\bar{u}}{2} A_0\phi_0 + \bar{\lambda}\epsilon_0 B_1\phi_0 \\ EA_1\phi_1 &= \frac{\bar{u}}{2}(1-2\epsilon_0^2) A_1\phi_1 + \bar{\lambda}\sqrt{2}\epsilon_0 B_2\phi_1, \end{aligned} \tag{3.19}$$

and for $n \geq 2$ we have

$$\begin{aligned} EA_n\phi_n &= \frac{\bar{u}}{2}(1-2n\epsilon_0^2) A_n\phi_n - \epsilon_0^2\sqrt{n(n-1)} B_{n-2}\phi_n + \bar{\lambda}\epsilon_0\sqrt{n+1} B_{n+1}\phi_n, \\ EB_{n-2}\phi_{n-2} &= -\epsilon_0^2\sqrt{n(n-1)} A_n\phi_{n-2} - \frac{\bar{u}}{2}[1-2(n-1)\epsilon_0^2] B_{n-2}\phi_{n-2} + \bar{\lambda}\epsilon_0\sqrt{n-2} A_{n-3}\phi_{n-2}. \end{aligned}$$

We can then collect all coefficients in the following basis,

$$\psi^{\mathsf{T}} = \left[A_0, A_1, A_2, B_0, \ldots, A_n, B_{n-2}, \ldots, A_N, B_{N-2} \right], \tag{3.20}$$

so that the above equations can be written in this basis as follows,

$$H_{\rm num} = \begin{pmatrix} H_1 & 0 & W_0 & W_1 & 0 & \cdots & 0 \\ 0 & H_2 & 0 & 0 & W_2 & \cdots & \vdots \\ W_0^\dagger & 0 & H_3 & 0 & 0 & \cdots & \vdots \\ W_1^\dagger & 0 & 0 & H_4 & 0 & \cdots & W_{N-3} \\ 0 & W_2^\dagger & 0 & 0 & H_5 & \vdots & \vdots \\ \vdots & \vdots & \vdots & \vdots & \vdots & \ddots & 0 \\ 0 & \cdots & \cdots & W_{N-3}^\dagger & \cdots & 0 & H_N \end{pmatrix}, \tag{3.21}$$

where the various 2×2 matrix blocks are given by

$$H_1 = \begin{pmatrix} \frac{\bar{u}}{2} & 0 \\ 0 & \frac{\bar{u}}{2}(1-2\epsilon_0^2) \end{pmatrix}, \quad H_{n\geq 2} = \begin{pmatrix} \bar{u}(\frac{1}{2}-n\epsilon_0^2) & -\sqrt{n(n-1)}\epsilon_0^2 \\ -\sqrt{n(n-1)}\epsilon_0^2 & \bar{u}[\frac{1}{2}-(n-1)\epsilon_0^2] \end{pmatrix},$$
$$W_0 = \begin{pmatrix} 0 & \bar{\lambda}\epsilon_0 \\ 0 & 0 \end{pmatrix}, \quad W_1 = \begin{pmatrix} 0 & 0 \\ 0 & \bar{\lambda}\sqrt{2}\epsilon_0 \end{pmatrix}, \quad W_{n\geq 2} = \begin{pmatrix} 0 & \bar{\lambda}\sqrt{n+1}\epsilon_0 \\ 0 & 0 \end{pmatrix}. \tag{3.22}$$

The LL structure can be obtained by diagonalizing the above Hamiltonian, and the result is shown in Fig. 3.4(b). This result reproduces the ones reported in Ref. [58], which is obtained from a four-band calculation. A prominent feature of this Landau level structure is that, when the magnetic field is small, the lowest Landau level (LLL) has a three-fold degeneracy, resulting from the formation of three Dirac cones at low energies. This three-fold degeneracy agrees with their observation that at a magnetic field of $B = 2.5\,\mathrm{T}$, only filling factors at $\nu = -3$ and $\nu = -6$ were seen [58]. In contrast, when the fields larger the cyclotron orbits are much smaller, and states in the Brillouin zone are strongly coupled, lifting the three-fold degeneracy. This is again supported by the experimental observation that at a larger field at $B = 6\,\mathrm{T}$, all integer filling factors between 0 and -6 were seen.

3.2.3.1 Estimate of the breakdown

The breakdown behavior can be estimated by the criterion that the magnetic length ℓ should correspond to a momentum space distance much less than the intervalley distance, i.e., $\ell^{-1} < \Delta K = \sqrt{3}k_c = \sqrt{3}r_c\gamma_1/\hbar v$, with r_c given by Eq. (2.21). However, this estimation seems to give too high an upper bound, because it indicates that $\sqrt{B} < 26.9r_c$, while $r_c = 0.21$ for $\bar{u} = 0.2$ and $\bar{\lambda} = 0.1$. The resulting critical field of $B_c = 31.9\,\mathrm{T}$ is much higher than the experimental observation. To better fit the observation we propose that

$$4\ell^{-1} < \Delta K = \sqrt{3}r_c\gamma_1/\hbar v. \tag{3.23}$$

This gives a critical field of $B_c = 2\,\mathrm{T}$.

3.3 Mapping momentum distributions of Landau levels

In this section we would like to map out the momentum space distribution of the LLL states. This is helpful because we can then identify which part of the momentum space these LLL states come from.

3.3.1 Formulation

This mapping is obtained in the following way. We remind ourselves that the eigenstates of annihilation operator $\hat{a}$ are coherent states:

$$\hat{a}|\alpha\rangle = \alpha|\alpha\rangle, \quad |\alpha\rangle = e^{-|\alpha|^2/2}\sum_{n=0}^{\infty}\frac{\alpha^n}{\sqrt{n!}}|n\rangle. \tag{3.24}$$

Because the momentum operator is related to the annihilation operator, $\hat{\pi} = \sqrt{2}\hbar\hat{a}/\ell$, we can translate the coherent state eigenvalue α to π as $\pi \equiv \pi_x + i\pi_y =$

$\sqrt{2}\hbar\alpha/\ell$, so that

$$\hat{\pi}|\pi\rangle = \pi|\pi\rangle \tag{3.25}$$

With this convention, the dimensionless momenta $x \sim \hbar v k_x/\gamma_1$ is related to α_x as

$$\alpha_x = \frac{k_x\ell}{\sqrt{2}} = \frac{\hbar v k_x}{\gamma_1}\frac{\gamma_1\ell}{\sqrt{2}\hbar v} = \frac{11}{\sqrt{B}}x, \tag{3.26}$$

where $x \equiv \hbar v k_x/\gamma_1$, and $\alpha = \alpha_x + i\alpha_y$.

The momentum distribution of the LLL states can now be found as

$$\phi(\boldsymbol{k}) = \langle\Psi|\pi\rangle = \frac{\sqrt{2\pi\ell^2}}{(\sum_m A_m^2)}\sum_{m=0}^{\infty} A_m e^{-|\alpha|^2/2}\frac{\alpha^m}{\sqrt{m!}}, \tag{3.27}$$

and then we can plot $|\phi(\boldsymbol{k})|^2$ to visualize the Landau level distribution in the momentum space.

We can first quickly see a special case where the LLL comes solely from the nth harmonic component. This is the case in bilayer graphene without trigonal warping effects. In this case, we can compute the average value of momentum k as

$$\langle k_n\rangle = \int \frac{d^2\boldsymbol{k}}{(2\pi)^2}k|\phi_n(\boldsymbol{k})|^2 = \frac{\sqrt{2}}{\ell}\frac{\Gamma(n+\frac{3}{2})}{\Gamma(n+1)}. \tag{3.28}$$

In the limit of large n we have

$$\lim_{n\to\infty}\langle\frac{k_n\ell}{\sqrt{2}}\rangle\frac{1}{\sqrt{n}} = \lim_{n\to\infty}\frac{\Gamma(n+\frac{3}{2})}{\Gamma(n+1)\sqrt{n}} = 1. \tag{3.29}$$

Therefore as a rule of thumb we have $\langle k_n\ell\rangle \simeq \sqrt{2n}$ for large n. We also have

$$\lim_{n\to\infty}\left[\langle\frac{k_n^2\ell^2}{2}\rangle - \langle\frac{k_n\ell}{\sqrt{2}}\rangle^2\right] = \lim_{n\to\infty}\left[(n+1) - \left(\frac{\Gamma(n+\frac{3}{2})}{\Gamma(n+1)}\right)^2\right] = \frac{1}{4}. \tag{3.30}$$

3.3.2 Application to the degenerate case

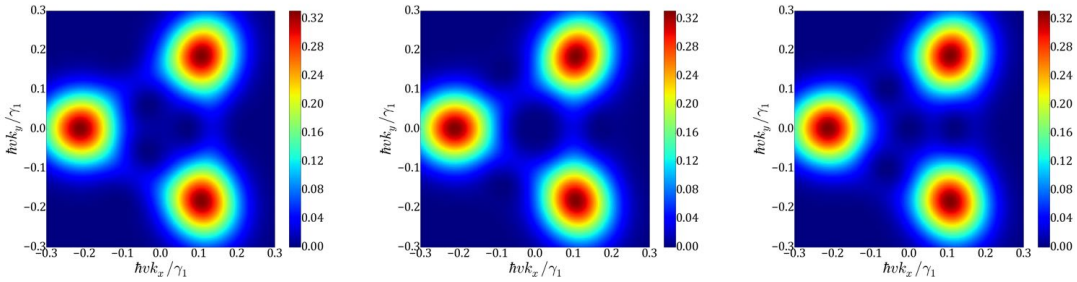

Figure 3.5: Momentum space distribution of the three LLL states at $B = 1\,\mathrm{T}$. Here we show the spin-up components only. Also we used the same set of parameters as fig. 3.4(b). This set of plots corresponds to line cut A in that figure. The energy decreases from left to right.

In Fig. 3.5 we plot the momentum space distribution of the LLL states at a field strength of $B = 1\,\mathrm{T}$ [see Fig. 3.4(b) for a plot of the corresponding LL structure]. We can see that in this case not only the three states are (almost) degenerate in energy, their wave function distribution in momentum space are also almost identical. In addition, the localization of the LLL states matches very well with the original bandstructure in Fig. 2.7.

One interesting point to note is that it is possible to build a state from the above three degenerate states that is solely concentrated around the π valley, but not possible to build a state that is solely concentrated around the $\pi/3$ valley or $-\pi/3$ valley. To see this more clearly we note that centers of each valley are given by $\alpha_s = \dfrac{11 r_c}{\sqrt{B}} e^{i\theta_s}$, where $r_c = 0.21$, and $\theta_s = \pi,\ \pi/3,$ and $-\pi/3$ for the three valleys. Suppose a new state is built from the three

degenerate basis states as follows,

$$|\Psi\rangle = s_0|\Psi_{j=0}\rangle + s_1|\Psi_{j=2}\rangle + s_2|\Psi_{j=1}\rangle, \tag{3.31}$$

where the state label increases with decreasing energy. Its momentum distribution is

$$\phi(\boldsymbol{k}) = \langle\Psi|\pi\rangle \frac{\sqrt{2\pi\ell^2}e^{-|\alpha|^2/2}}{\sum_m \left(\sum_{\lambda=0}^{2} A_m^{(\lambda)} s_\lambda\right)^2} \sum_{m=0}^{\infty} \left(\sum_{\lambda=0}^{2} A_m^{(\lambda)} s_\lambda\right) \frac{\alpha^m}{\sqrt{m!}}. \tag{3.32}$$

In order to build a state at one valley, we need to turn off the above amplitude at the other two valleys. This condition will help us solve for the particular set of (s_0, s_1, s_2). To proceed we calculate the following coefficients:

$$T_\alpha^\lambda = \sum_{m=0}^{\infty} A_m^{(\lambda)} \frac{\alpha^m}{\sqrt{m!}}, \tag{3.33}$$

where α indicates the three pockets, while λ indicates the three basis states. The value of T_α^λ is summarized in the following table.

Table 3.1: Coefficients of T_α^λ

T_α^λ	$\lambda = 0$	$\lambda = 1$	$\lambda = 2$
$\alpha = \pi/3$	-8.2218	$4.1135 - 7.1249i$	$-4.1106 - 7.1198i$
$\alpha = -\pi/3$	-8.2218	$4.1135 + 7.1249i$	$-4.1106 + 7.1198i$
$\alpha = \pi$	-8.2218	-8.2271	8.2213

Now if we try to turn off the amplitudes at valley $\pi/3$ and $-\pi/3$, we need to ensure $\sum_{\lambda=0}^{3} s_\lambda T_{\pi/3}^\lambda = 0$, and $\sum_{\lambda=0}^{3} s_\lambda T_{-\pi/3}^\lambda = 0$. These two conditions and the normalization condition yield a unique solution of

$$|\Psi_\pi\rangle = \frac{1}{\sqrt{3}} \left(|\Psi_{j=0}\rangle + |\Psi_{j=2}\rangle + e^{i\pi}|\Psi_{j=1}\rangle\right). \tag{3.34}$$

This state will be solely localized at the π valley.

However, if we try to build a state localized at the $\pi/3$ valley, we need $\sum_{\lambda=0}^{3} s_\lambda T^\lambda_{-\pi/3} = 0$, and $\sum_{\lambda=0}^{3} s_\lambda T^\lambda_{\pi} = 0$. We find that the following solution will satisfy the requirement:

$$|\Psi_{\pi/3}\rangle = \frac{1}{\sqrt{3}}\left(|\Psi_{j=0}\rangle + e^{-2i\pi/3}|\Psi_{j=2}\rangle + e^{-i\pi/3}|\Psi_{j=1}\rangle\right). \tag{3.35}$$

Similarly we can consider a state localized at the $-\pi/3$ valley, we need $\sum_{\lambda=0}^{3} s_\lambda T^\lambda_{\pi/3} = 0$, and $\sum_{\lambda=0}^{3} s_\lambda T^\lambda_{\pi} = 0$. We find that the following solution will satisfy the requirement:

$$|\Psi_{-\pi/3}\rangle = \frac{1}{\sqrt{3}}\left(|\Psi_{j=0}\rangle + e^{2i\pi/3}|\Psi_{j=2}\rangle + e^{i\pi/3}|\Psi_{j=1}\rangle\right). \tag{3.36}$$

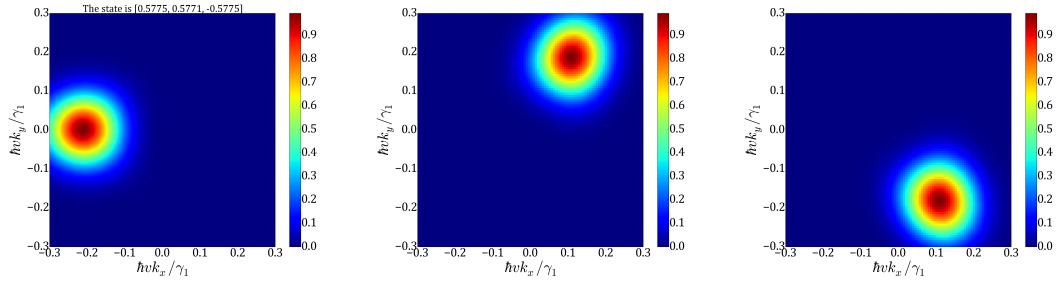

Figure 3.6: Making a single-valley state. Here we plot the three states that are localized at a particular valley. They are obtained by making superpositions of the original three degenerate states.

From these results we find that we can build the other two states from the $|\Psi_\pi\rangle$ state by two unitary transformations, i.e., $|\Psi_{\pi/3}\rangle = U_-|\Psi_\pi\rangle$, and $|\Psi_{-\pi/3}\rangle = U_+|\Psi_\pi\rangle$, where

$$U_- = \begin{pmatrix} 1 & 0 & 0 \\ 0 & e^{-2\pi i/3} & 0 \\ 0 & 0 & e^{-4\pi i/3} \end{pmatrix}, \quad U_+ = \begin{pmatrix} 1 & 0 & 0 \\ 0 & e^{2\pi i/3} & 0 \\ 0 & 0 & e^{4\pi i/3} \end{pmatrix}. \tag{3.37}$$

3.3.3 Application to cases with higher fields

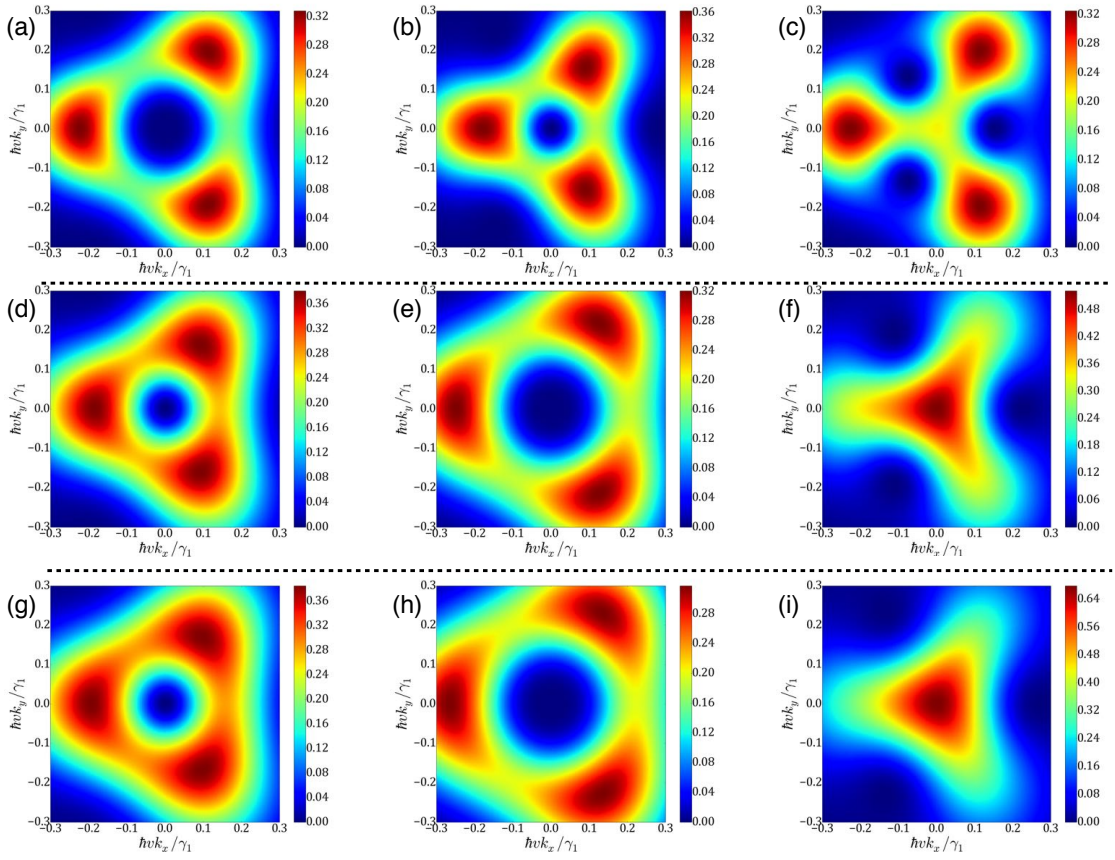

Figure 3.7: Momentum space distribution of the three LLL states at various B fields. Again we show the spin-up components only. (a)-(c) $B = 2.2\,\mathrm{T}$, (d)-(f) $B = 3.0\,\mathrm{T}$, (g)-(i) $B = 3.5\,\mathrm{T}$. The three sets of plots correspond to line cuts B, C, and D in Fig. 3.4. In addition, in all these plots the energy decreases from left to right within the same group.

We can similarly study the momentum distribution at larger fields. In Fig. 3.7 we show three different cases with a field strength of $B = 2.2\,\mathrm{T}$, $B = 3.0\,\mathrm{T}$, and $B = 3.5\,\mathrm{T}$, respectively. A first observation is that there is a

phase transition between the first two cases, as the weight of the third LLL state evolves from three side pockets to the center, while the character of the first two states seems to have been swapped. When going from $B = 3.0\,\mathrm{T}$ to $B = 3.5\,\mathrm{T}$ the change is not very significant.

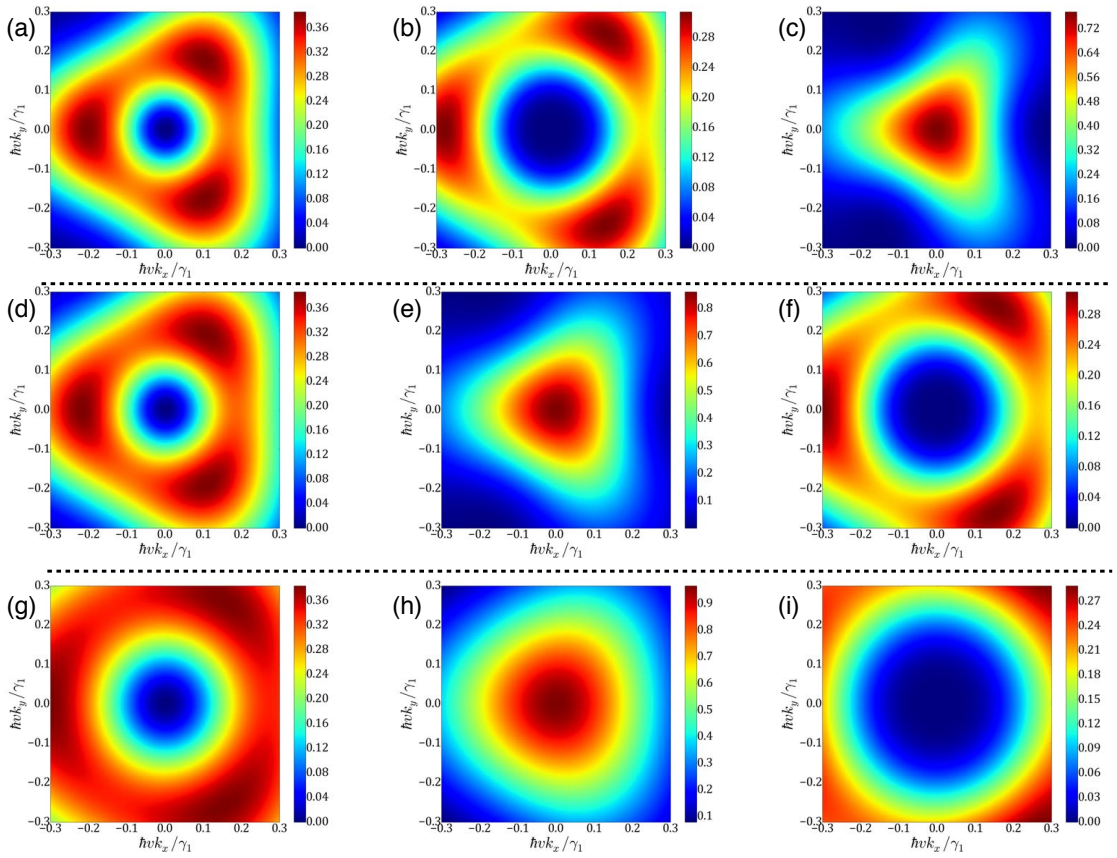

Figure 3.8: Momentum space distribution of the three LLL states at various B fields. Again we show the spin-up components only. (a)-(c) $B = 4.0\,\mathrm{T}$, (d)-(f) $B = 4.8\,\mathrm{T}$, (g)-(i) $B = 10.0\,\mathrm{T}$. The first sets of plots correspond to line cuts E and F in Fig. 3.4, while in the last set the fields are so large that the results should already go back to the case without trigonal warping effects.

Another phase transition occurs at a field strength of $B = 4.8\,\mathrm{T}$, as shown in Fig. 3.8 (d-f). We can see that right at the phase transition, the characters of the second and third LLL state are swapped, so that the second state has its weight at the center, while the third state has its weight moved to the side. This trend continues to very large fields of $B = 10\,\mathrm{T}$ [see Fig. 3.8 (h-i)], where the results should almost be the same as those without trigonal warping effects. Indeed, we can see that the momentum distribution becomes much more isotropic. In addition, we have confirmed that the first LLL state comes mainly from the $n = 1$ harmonic, the second mainly from the $n = 0$ harmonic, while the third mainly from the $n = 2$ harmonic, all within our expectations.

Chapter 4

Quantum Hall ferromagnetism

Electron-electron interactions play a dominant role in the quantum Hall physics. This is because the kinetic energy of the electrons has been quenched by the external magnetic field, and the Coulomb potential is the dominant energy scale in the quantum Hall regime. In this chapter we are going to focus on electron-electron interactions in the integer quantum Hall regime. It is known that in this regime the interplay between quantum Hall physics and electron-electron interactions often leads to spontaneous ordering of internal degrees of freedom, most commonly electron spin or layer degrees of freedom. We will use bilayer graphene as an example to illustrate various interesting aspects in the theory of quantum Hall ferromagnetism.

4.1 Hartree-Fock theory in the integer QH regime

Electron-electron interactions are very different in the integer and fractional quantum Hall regimes. In the fractional quantum Hall regime Coulomb interactions cannot be treated perturbatively, and therefore one often has to resort to some non-perturbative methods like exact diagonalization. In the integer quantum Hall regime, however, Hartree-Fock theory is known to work

quite well, especially for cases where the ground state is gapped. Therefore, in this chapter we will only adopt Hartree-Fock theory to treat electron-electron interactions in bilayer graphene in the integer quantum Hall regime. We first establish the general formalism in this section, and apply it to our specific model in the next section. We will present our results and discussions in the last section.

4.1.1 Coulomb interactions in the quantum Hall regime

The Hartree-Fock theory in the quantum Hall regime was explained nicely in the seminal paper by Allan MacDonald *et al* [8]. We will briefly review this theory here. Working in the Landau gauge, we write, for the Hamiltonian of the two-dimensional electron gas subject to a transverse magnetic field $\boldsymbol{B} = -B_0\hat{z}$ as follows,

$$\begin{aligned}\mathcal{H} = &\sum_{n,X} \varepsilon_n c^\dagger_{n,X} c_{n,X} \\ &+ \frac{1}{2S}\sum_{n_i,X_i} V(\boldsymbol{q})\langle n_1 X_1|e^{i\boldsymbol{q}\cdot\boldsymbol{r}_{\rm op}}|n_4 X_4\rangle\langle n_2 X_2|e^{-i\boldsymbol{q}\cdot\boldsymbol{r}_{\rm op}}|n_3 X_3\rangle c^\dagger_{n_1X_1}c^\dagger_{n_2X_2}c_{n_3X_3}c_{n_4X_4},\end{aligned} \tag{4.1}$$

where $V(\boldsymbol{q}) = 2\pi e^2/|\boldsymbol{q}|$ is the Fourier transform of the Coulomb potential, and

$$\langle \boldsymbol{r}|n, X\rangle = \frac{1}{\sqrt{L_y}} e^{iXy/\ell^2}\phi_n(x - X), \quad n = 0, 1, 2, \cdots . \tag{4.2}$$

The function $\phi_n(x - X)$ is a one-dimensional harmonic oscillator eigenstate,

$$\phi_n(x - X) = \frac{1}{(\sqrt{\pi}\ell 2^n n!)^{1/2}} e^{-(x-X)^2/\ell^2} H_n[(x - X)/\ell], \tag{4.3}$$

where $H_n(x)$ is the Hermite polynomial. X is the guiding center of the cyclotron motion. For a finite system, the allowed values of X are separated by

a minimal distance of $2\pi\ell^2/L_y$. The orbital degeneracy of each Landau level is given by $g = S/2\pi\ell^2$, where S is the area of the two-dimensional electron gas. Finally, the $\boldsymbol{r}_{\rm op}$ appeared in the above Hamiltonian represent the *operator* for real-space coordinates, and it is related to the actual coordinates $\boldsymbol{r}$ by

$$e^{i\boldsymbol{q}\cdot\boldsymbol{r}_{\rm op}} = \int d^2\boldsymbol{r}|\boldsymbol{r}\rangle e^{i\boldsymbol{q}\cdot\boldsymbol{r}}\langle\boldsymbol{r}|. \tag{4.4}$$

The matrix elements $\langle n', X'|e^{i\boldsymbol{q}\cdot\boldsymbol{r}_{\rm op}}|n, X\rangle$ in Eq. (4.1) are given by

$$\langle n_1 X_1|e^{i\boldsymbol{q}\cdot\boldsymbol{r}_{\rm op}}|n_4 X_4\rangle = \delta_{X_1, X_4+q_y\ell^2} e^{\frac{i}{2}q_x(X_1+X_4)} F_{n_1,n_4}(\boldsymbol{q}), \tag{4.5}$$

where

$$F_{n_1,n_4}(\boldsymbol{q}) = e^{-q^2\ell^2}\sqrt{\frac{n_4!}{n_1!}}\left(\frac{iq_x\ell - q_y\ell}{\sqrt{2}}\right)^{n_1-n_4} L_{n_4}^{n_1-n_4}(q^2\ell^2/2),$$

for $n_1 \geq n_4$, where $L_n^\alpha(x)$ is the generalized Laguerre polynomial. Note that $F_{n_1,n_4}(\boldsymbol{q}) = [F_{n_4,n_1}(-\boldsymbol{q})]^*$. For a derivation of the above result, please refer to Appendix B.1.

4.1.2 Density matrix in the quantum Hall regime

We now turn to the density matrix in the quantum Hall regime. In the Landau eigenstate basis, the density operator takes the following form

$$n(\boldsymbol{r}) = \psi^\dagger(\boldsymbol{r})\psi(\boldsymbol{r}) = \langle n_1 X_1|\boldsymbol{r}\rangle\langle\boldsymbol{r}|n_4 X_4\rangle. \tag{4.6}$$

Its Fourier transform is given by

$$n(\boldsymbol{q}) = \int d^2\boldsymbol{r} e^{-i\boldsymbol{q}\cdot\boldsymbol{r}} n(\boldsymbol{r}) = g\sum_{n_1,n_4}\rho_{n_1n_4}(\boldsymbol{q})F_{n_1n_4}(-\boldsymbol{q}), \tag{4.7}$$

where we have introduced the operator

$$\rho_{n_1 n_4}(\boldsymbol{q}) = \frac{1}{g}\sum_X e^{-iq_x X - \frac{i}{2}q_x q_y \ell^2} c^\dagger_{n_1 X} c_{n_4, X+q_y\ell^2}, \tag{4.8}$$

which satisfies

$$\sum_n \rho_{nn}(\boldsymbol{q}=0) = \frac{N}{g}, \tag{4.9}$$

where N is the number operator. $\nu = \langle N\rangle/g$ is the Landau-level filling factor of the electron gas. In most cases, we will actually work with ρ, the so-called *bare density operator*, instead of the physical density operator n.

It is also useful to establish a relation between $\rho_{n_1 n_4}(\boldsymbol{q})$ and $c^\dagger_{n_1 X_1} c_{n_4 X_4}$, because the original Hamiltonian [Eq. (4.1)] is written in terms of the creation and annihilation operators $c_{n,X}$, not the density matrices. Such a relation can be found by inverting Eq. (4.9), which gives

$$c^\dagger_{n_1 X_1} c_{n_4 X_4} = \sum_{\boldsymbol{p}} \rho_{n_1 n_4}(\boldsymbol{p}) e^{\frac{i}{2}p_x(X_1+X_4)} \delta_{X_1, X_4 - p_y\ell^2}. \tag{4.10}$$

In the crystal phase the average density $\langle n(\boldsymbol{q})\rangle$ [and therefore $\langle\rho(\boldsymbol{q})\rangle$] is nonzero only at $\boldsymbol{q} = \boldsymbol{G}$, where $\boldsymbol{G}$ is a reciprocal lattice vector of the two-dimensional lattice formed in the crystal phase (not the crystal structure of the solid). As a result, the expectation value of $c^\dagger_{n_1 X_1} c_{n_4 X_4}$ is given by

$$\langle c^\dagger_{n_1 X_1} c_{n_4 X_4}\rangle = \sum_{\boldsymbol{G}} \langle\rho_{n_1 n_4}(\boldsymbol{G})\rangle e^{\frac{i}{2}G_x(X_1+X_4)} \delta_{X_1, X_4 - G_y\ell^2}. \tag{4.11}$$

On the other hand, if the total charge density is uniform, the average density $\langle\rho(\boldsymbol{q})\rangle$ is nonzero only at $\boldsymbol{q} = \boldsymbol{G} = 0$. Most of our discussions will be carried out in this limit, but we will keep a nonzero $\boldsymbol{G}$ in deriving the general formalism.

4.1.3 Hartree-Fock approximation

Now we would like to make Hartree-Fock approximation to the general Hamiltonian in Eq. (4.1), and derive the Hartree-Fock Hamiltonian.

If we summarize the above results, we obtain the Hartree-Fock approximation for Eq. (4.1) as follows,

$$\mathcal{H}_{\rm HF} = g\sum_{n}\varepsilon_n\rho_{nn}(\boldsymbol{G}=0) + g\sum_{\boldsymbol{G}}\sum_{n,n'}U(n,n';\boldsymbol{G})\rho_{nn'}(\boldsymbol{G}), \tag{4.12}$$

where we have defined an effective potential $U(n,n';\boldsymbol{G})$, given by

$$U(n,n';\boldsymbol{G}) = \sum_{n_1,n_2}\frac{e^2}{\ell}[H(n_1,n_2,n,n';\boldsymbol{G}) - X(n_1,n',n,n_2;\boldsymbol{G})]\langle\rho_{n_1n_2}(-\boldsymbol{G})\rangle, \tag{4.13}$$

with the Hartree and Fock terms defined by

$$H(n_1,n_2,n_3,n_4;\boldsymbol{G}) = \frac{1}{2\pi e^2\ell}V(\boldsymbol{G})F_{n_1,n_2}(\boldsymbol{G})F_{n_3,n_4}(-\boldsymbol{G}), \tag{4.14}$$

$$X(n_1,n_2,n_3,n_4;\boldsymbol{G}) = \frac{\ell}{e^2S}\sum_{\boldsymbol{q}}V(\boldsymbol{q})F_{n_1,n_2}(\boldsymbol{q})F_{n_3,n_4}(-\boldsymbol{q})e^{i\boldsymbol{q}\times\boldsymbol{G}\ell^2}. \tag{4.15}$$

A detailed derivation of this result can be found in the Appendix.

4.2 QH ferromagnetism in bilayer graphene: theory

In this chapter we are going to focus on the three-fold degenerate LL's in gapped bilayer graphene with trigonal warping [see Eq. (3.10)]. We will show that electron-electron interaction breaks this degeneracy, and makes all integer filling factors appear even at low magnetic fields. The energy scale for this splitting is estimated to be $e^2/\kappa\ell\gamma_1 \simeq 0.14\sqrt{B}$. In this section we will

use the formalism established in the previous section to construct a theory to describe quantum Hall ferromagnetism in bilayer graphene, and leave the results to the next section.

First of all we find that the plane-wave matrix element for the lowest LL is given by

$$\langle \lambda_1 X_1 | e^{i\boldsymbol{q}\cdot\boldsymbol{r}} | \lambda_4 X_4 \rangle = e^{\frac{i}{2}q_x(X_1+X_4)} \delta_{X_1, X_4+q_y\ell^2} S_{\lambda_1\lambda_4}(\boldsymbol{q}), \tag{4.16}$$

where the term $S_{\lambda_1\lambda_4}(\boldsymbol{q})$ is

$$S_{\lambda_1\lambda_4}(\boldsymbol{q}) = \sum_{n_1,n_2=0}^{N} \left[A_{n_1}^{(\lambda_1)} A_{n_2}^{(\lambda_4)} + B_{n_1}^{(\lambda_1)} B_{n_2}^{(\lambda_4)} \right] F_{n_1 n_2}(\boldsymbol{q}). \tag{4.17}$$

In the above result, we have introduced $B_{N-1} = 0$, $B_N = 0$, and the term $F_{n_1 n_2}(\boldsymbol{q})$ reads

$$F_{n_1 n_2}(\boldsymbol{q}) = e^{-q^2\ell^2/4} \sqrt{\frac{n_<!}{n_>!}} \left(\frac{\tilde{q}}{\sqrt{2}} \right)^{n_> - n_<} L_{n_<}^{n_> - n_<} \left(\frac{q^2\ell^2}{2} \right), \tag{4.18}$$

with $n_{>(<)}$ being the larger (smaller) of n_1 and n_2, $q^2 \equiv q_x^2 + q_y^2$, and

$$\tilde{q} = \begin{cases} (iq_x - q_y)\ell = iq\ell e^{i\theta}, & n_1 \geq n_2 \\ (iq_x + q_y)\ell = iq\ell e^{-i\theta}, & n_1 < n_2, \end{cases} \tag{4.19}$$

where $\theta = \arctan(q_y/q_x)$ is the relative angle between q_x and q_y. As a result, we can write it in a simple way as

$$\tilde{q}^{(n_> - n_<)} = (iq\ell)^{(n_> - n_<)} e^{i(n_1 - n_2)\theta}. \tag{4.20}$$

We further note that the Laguerre polynomial is defined as

$$L_m^{(\alpha)}(x) = \sum_{k=0}^{m} \frac{(-1)^k}{k!} \binom{m+\alpha}{m-k} x^k. \tag{4.21}$$

4.2.1 The Hartree energy

We can first consider the Hartree energy, which is given by

$$H_H = \frac{g^2}{S}\sum_{\boldsymbol{G}\lambda\sigma} V(\boldsymbol{G})\rho_{\lambda\lambda}(-\boldsymbol{G})\langle\rho_{\sigma\sigma}(\boldsymbol{G})\rangle \times \sum_{n_i,m_i=0}^{N}\left[A^{(\lambda)}_{n_1}A^{(\lambda)}_{n_2}+B^{(\lambda)}_{n_1}B^{(\lambda)}_{n_2}\right]\left[A^{(\sigma)}_{m_1}A^{(\sigma)}_{m_2}+B^{(\sigma)}_{m_1}B^{(\sigma)}_{m_2}\right]F_{n_1n_2}(\boldsymbol{G})F_{m_1m_2}(-\boldsymbol{G}), \tag{4.22}$$

where $g = S/2\pi\ell^2$ is the orbital degeneracy of a single Landau level. We adopt the usual approximation that $\langle\rho_{\sigma\sigma}(\boldsymbol{G})\rangle \neq 0$ only when $\boldsymbol{G} = 0$, and then rewrite the above Hartree potential as follows,

$$H_H = \frac{g^2}{S}\sum_{\lambda\sigma}\rho_{\lambda\lambda}\langle\rho_{\sigma\sigma}\rangle Y_{\lambda\sigma}, \tag{4.23}$$

where the integral matrix $Y_{\lambda\sigma}$ is given by

$$Y_{\lambda\sigma} = \sum_{n_i,m_i=0}^{N} F_{n_1n_2}(\boldsymbol{0})F_{m_1m_2}(\boldsymbol{0})\lim_{q\to 0}V_s(q)\Big[\left(A^{(\lambda)}_{n_1}A^{(\lambda)}_{n_2}A^{(\sigma)}_{m_1}A^{(\sigma)}_{m_2}+B^{(\lambda)}_{n_1}B^{(\lambda)}_{n_2}B^{(\sigma)}_{m_1}B^{(\sigma)}_{m_2}\right) + e^{-qd}\left(A^{(\lambda)}_{n_1}A^{(\lambda)}_{n_2}B^{(\sigma)}_{m_1}B^{(\sigma)}_{m_2}+B^{(\lambda)}_{n_1}B^{(\lambda)}_{n_2}A^{(\sigma)}_{m_1}A^{(\sigma)}_{m_2}\right)\Big]. \tag{4.24}$$

This is difficult to handle. However we can argue that because we do want a layer-polarized state, this Hartree energy is not important. We will ignore it in the following calculations.

4.2.2 The exchange energy

We can then consider the exchange energy, which is given formally by

$$H_F = -\frac{N_\phi}{A}\sum_{\lambda_i}\rho^{\lambda_1\lambda_3}\langle\rho^{\lambda_2\lambda_4}\rangle\sum_{\boldsymbol{q}}V(\boldsymbol{q})S_{\lambda_1\lambda_4}(\boldsymbol{q})S_{\lambda_2\lambda_3}(-\boldsymbol{q}). \tag{4.25}$$

We should emphasize that in this case we can no longer limit our considerations to intravalley scattering processes only. This is because all these electron pockets are close to each other, and it would be inappropriate to neglect any of the scattering processes.

The resulting exchange energy matrix will be given by

$$\langle\alpha|H_F|\beta\rangle = -\frac{N_\phi}{A}\sum_{\lambda\sigma}\langle\rho^{\lambda\sigma}\rangle \mathbb{S}^{\lambda\sigma}_{\alpha\beta}, \tag{4.26}$$

where the integral is given by

$$\mathbb{S}^{\lambda\sigma}_{\alpha\beta} = \sum_{\boldsymbol{q}} V(\boldsymbol{q}) S_{\alpha\sigma}(\boldsymbol{q}) S_{\lambda\beta}(-\boldsymbol{q}) \tag{4.27}$$

We first rewrite the form factor as follows,

$$S_{\alpha\sigma}(\boldsymbol{q})S_{\lambda\beta}(-\boldsymbol{q}) = \sum_{n_i,m_i=0}^{N} \left[A^{(\alpha)}_{n_1}A^{(\sigma)}_{n_2} + B^{(\alpha)}_{n_1}B^{(\sigma)}_{n_2}\right]\left[A^{(\lambda)}_{m_1}A^{(\beta)}_{m_2} + B^{(\lambda)}_{m_1}B^{(\beta)}_{m_2}\right] F_{n_1n_2}(\boldsymbol{q})F_{m_1m_2}(-\boldsymbol{q}).$$

Therefore we just need to study the following two integrals,

$$\begin{aligned} I_s(n_1,n_2;m_1,m_2) &= \frac{\ell\kappa}{e^2}\frac{1}{A}\sum_{\boldsymbol{q}} V(\boldsymbol{q})F_{n_1n_2}(\boldsymbol{q})F_{m_1m_2}(-\boldsymbol{q}) \qquad (4.28)\\ &= \sqrt{\frac{n_<!m_<!}{n_>!m_>!}}\int_0^\infty dx e^{-x^2/2}L^{n_d}_{n_<}(x^2/2)L^{m_d}_{m_<}(x^2/2)\left(\frac{ix}{\sqrt{2}}\right)^{n_d+m_d}\\ &\quad\cdot(-1)^{m_d}\cdot\frac{1}{2\pi}\int_0^{2\pi}d\theta e^{i\theta(n_1-n_2+m_1-m_2)}\\ &= (-1)^{m_d}\delta_{m_2,n_1-n_2+m_1}\sqrt{\frac{n_<!m_<!}{n_>!m_>!}}\\ &\quad\cdot\int_0^\infty dx e^{-x^2/2}L^{n_d}_{n_<}(x^2/2)L^{m_d}_{m_<}(x^2/2)\left(\frac{ix}{\sqrt{2}}\right)^{n_d+m_d},\\ I_d(n_1,n_2;m_1,m_2) &= (-1)^{m_d}\delta_{m_2,n_1-n_2+m_1}\sqrt{\frac{n_<!m_<!}{n_>!m_>!}} \qquad (4.29) \end{aligned}$$

$$\cdot \int_0^\infty dx e^{-x^2/2} e^{-(d/\ell)x} L_{n_<}^{n_d}(x^2/2) L_{m_<}^{m_d}(x^2/2) \left(\frac{ix}{\sqrt{2}}\right)^{n_d+m_d},$$

where we have defined $n_d \equiv n_> - n_<$ and $m_d \equiv m_> - m_<$. In the above derivations, we have assumed the interaction potential $V(\boldsymbol{q})$ to be the long-range Coulomb potential, $V(\boldsymbol{q}) = 2\pi e^2/\kappa q$, while the factor $e^{-qd} = e^{-(d/\ell)x}$ captures the fact that electron-electron interaction between different layers are suppressed. We usually take the layer separation to be $d = 0.335\,\text{nm}$ [**?**]. As a result, we have $d/\ell = 0.013\sqrt{B}$.

Finally, the exchange energy matrix is given by

$$\langle \alpha | H_F | \beta \rangle = -N_\phi \frac{e^2}{\kappa \ell} \sum_{\lambda\sigma} \langle \rho^{\lambda\sigma} \rangle \mathcal{S}_{\alpha\beta}^{\lambda\sigma}, \tag{4.30}$$

where $\mathcal{S}_{\alpha\beta}^{\lambda\sigma}$ has the following form,

$$\begin{aligned}\mathcal{S}_{\alpha\beta}^{\lambda\sigma} = \sum_{n_i,m_i=0}^{N} \Big\{ &\left[A_{n_1}^{(\alpha)} A_{n_2}^{(\sigma)} A_{m_1}^{(\lambda)} A_{m_2}^{(\beta)} + B_{n_1}^{(\alpha)} B_{n_2}^{(\sigma)} B_{m_1}^{(\lambda)} B_{m_2}^{(\beta)}\right] I_s(n_1, n_2; m_1, m_2) \\ &+ \left[A_{n_1}^{(\alpha)} A_{n_2}^{(\sigma)} B_{m_1}^{(\lambda)} B_{m_2}^{(\beta)} + B_{n_1}^{(\alpha)} B_{n_2}^{(\sigma)} A_{m_1}^{(\lambda)} A_{m_2}^{(\beta)}\right] I_d(n_1, n_2; m_1, m_2)\Big\}. \end{aligned} \tag{4.31}$$

We now just need to compute the 3×3 coefficient matrix.

4.2.2.1 The two integrals

The Laguerre polynomial oscillates very fast when its order becomes large. This makes direct numerical integrations complicated. Actually this type of integrals has been studied before [15, 32]. A useful identity is

$$\int_0^\infty e^{-x} x^\alpha L_m^{(\beta)}(x) L_n^{(\gamma)}(x) dx \equiv I_{m,n}(\alpha, \beta, \gamma) \tag{4.32}$$

$$= \frac{\Gamma(\alpha+1)\Gamma(n+\gamma+1)\Gamma(\beta-\alpha+m)}{\Gamma(m+1)\Gamma(n+1)\Gamma(\gamma+1)\Gamma(\beta-\alpha)} \cdot {}_3F_2(-n, \alpha+1, \alpha-\beta+1; \gamma+1, \alpha+1-\beta-m; 1).$$

Therefore, we try to simplify the two integrals as follows. The first integral is simple,

$$I_s(n_1, n_2; m_1, m_2) = (-1)^{m_d}\delta_{m_2, n_1-n_2+m_1}\sqrt{\frac{n_<!m_<!}{n_>!m_>!}}\frac{i^{n_d+m_d}}{\sqrt{2}}I_{m_<,n_<}\left(\frac{n_d+m_d-1}{2}, m_d, n_d\right),$$

Currently I did not find a good way to deal with the second integral, so I will just leave it with numerical evaluations:

$$I_s(n_1, n_2; m_1, m_2) = (-1)^{m_d}\delta_{m_2, n_1-n_2+m_1}\sqrt{\frac{n_<!m_<!}{n_>!m_>!}}\frac{i^{n_d+m_d}}{\sqrt{2}} \cdot \cdot \int_0^\infty dy e^{-\frac{\sqrt{2}d}{\ell}\sqrt{y}} e^{-y} y^{(n_d+m_d-1)/2} L_{m_<}^{m_d}(y) L_{n_<}^{n_d}(y). \quad (4.33)$$

4.2.2.2 The structure of $\mathcal{S}_{\alpha\beta}^{\lambda\sigma}$ matrix

We will take a look at the structure of $\mathcal{S}_{\alpha\beta}^{\lambda\sigma}$ matrix at $B = 1\,\mathrm{T}$. Its nonzero values can be grouped into four sets, as shown in Table 4.1. We note that the values quoted in the first column are approximate; the actual values roughly have a 5% variations around these quoted values. For the first row, for example, the three values are all close to 0.64; but the actual values are $\mathcal{S}_{00}^{00} = 0.644587$, $\mathcal{S}_{11}^{11} = 0.648812$, and $\mathcal{S}_{22}^{22} = 0.646215$.

We note that these sets of nonzero values all satisfy the relation that

$$\alpha + \lambda = \beta + \sigma \mod 3, \quad (4.34)$$

Table 4.1: Nonzero values of $\mathcal{S}^{\lambda\sigma}_{\alpha\beta}$ at $B = 1\,\mathrm{T}$.

$\mathcal{S}^{\lambda\sigma}_{\alpha\beta}$	$(\alpha, \beta, \lambda, \sigma)$
0.64	(0, 0, 0, 0), (1, 1, 1, 1), (2, 2, 2, 2)
0.47	(0, 0, 1, 1), (0, 0, 2, 2), (0, 1, 1, 0), (0, 2, 2, 0) (1, 0, 0, 1), (1, 1, 0, 0), (1, 1, 2, 2), (1, 2, 2, 1) (2, 0, 0, 2), (2, 1, 1, 2), (2, 2, 0, 0), (2, 2, 1, 1)
0.29	(0, 2, 1, 2), (1, 2, 0, 2), (2, 0, 2, 1), (2, 1, 2, 0)
−0.29	(0, 1, 0, 2), (0, 1, 2, 1), (0, 2, 0, 1), (1, 0, 1, 2) (1, 0, 2, 0), (1, 2, 1, 0), (2, 0, 1, 0), (2, 1, 0, 1)

which is similar to the requirement that $n_1 - n_2 + m_1 - m_2 = 0$. We can view both conditions as a manifest of angular momentum conservation.

4.2.3 The full Hartree-Fock Hamiltonian

The full Hartree-Fock Hamiltonian can be written as follows,

$$\langle \alpha s|\mathcal{H}|\beta s'\rangle = (E^{(\alpha)}_{\mathrm{LL}}\delta_{ss'} + E_z\sigma^z_{ss'})\delta_{\alpha\beta} - \frac{e^2}{\kappa\ell}\sum_{\lambda\sigma}\mathcal{S}^{\lambda\sigma}_{\alpha\beta}\Delta^{\lambda\sigma}_{ss'}\delta_{ss'}. \tag{4.35}$$

In the above equation, ss' denote electron spin, and $\lambda\sigma$ denote the three flavors in the LLL state. $E^{\lambda}_{\mathrm{LL}}$ is the single-particle LL energy for flavor λ, $E_z = g\mu_B B$ is the Zeeman energy, with the assumption that $g = 2$. Finally, the expectation value of the density matrix $\rho^{\lambda s}_{\sigma s'}$ is defined as follows,

$$\Delta^{\lambda\sigma}_{ss'} = \langle c^\dagger_{\sigma s} c_{\lambda s'}\rangle. \tag{4.36}$$

To simplify numerical calculations, we scale the typical energies by γ_1, and obtain the following

$$\frac{E_z}{\gamma_1} = 2.89\times 10^{-4} B[\mathrm{T}], \quad \frac{E_F}{\gamma_1} \equiv \frac{e^2}{\kappa\ell\gamma_1} = 0.14\frac{\sqrt{B}}{\kappa}. \tag{4.37}$$

4.3 QH ferromagnetism in bilayer graphene: results

4.3.1 Results at $B = 1\,\mathrm{T}$

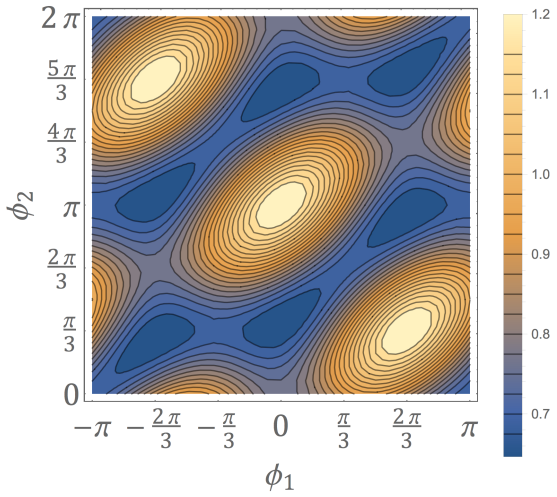

Figure 4.1: Angular dependence of the energy functional in Eq. (4.38). We can see the three minima.

In this section we study how the interaction breaks the three-fold orbital degeneracy at a field strength of $B = 1\,\mathrm{T}$.

4.3.1.1 Filling factor $\nu = 1$

We first look at the case of filling one of the six components, and the results are exactly *the single-valley states* given in Eqs. (3.34)-(3.36), with spin polarized in the down state. Numerical iterations yield the state $|\Psi_{-\pi/3}\rangle$, with an energy of -0.2688, but in fact all three states are equally good. For this one-component case we can obtain a simple analytical expression to show why such valley polarized state is the preferred ground state. This argument goes like this. We write down the general expression for the trial wave function as

$|\Psi\rangle = [r_0, r_1 e^{i\phi_1}, r_2 e^{i\phi_2}]^\intercal$, with the normalization constraint that $r_0^2 + r_1^2 + r_2^2 = 1$. As a result, the Fock energy of this state [i.e., the second term in Eq. (4.35)] is given by

$$E = -\frac{e^2}{\kappa\ell}\big[\mathcal{S}_{00}^{00}(r_0^4 + r_1^4 + r_2^4) + 4\mathcal{S}_{00}^{11}(r_0^2 r_1^2 + r_0^2 r_2^2 + r_1^2 r_2^2) + 4\mathcal{S}_{02}^{12} r_0 r_1 r_2^2 \cos(2\phi_2 - \phi_1) \\ + 4\mathcal{S}_{01}^{02} r_0^2 r_1 r_2 \cos(\phi_1 + \phi_2) + 4\mathcal{S}_{01}^{02} r_0 r_1^2 r_2 \cos(2\phi_1 - \phi_2)\big], \tag{4.38}$$

where $\mathcal{S}_{00}^{00} \simeq 0.64$, $\mathcal{S}_{00}^{11} \simeq 0.47$, $\mathcal{S}_{02}^{12} \simeq 0.29$, and $\mathcal{S}_{01}^{02} \simeq -0.29$ represent the four different values of the exchange integral matrix. We then find that the minimum of this function is achieved at $r_0 = r_1 = r_2 = \dfrac{1}{\sqrt{3}}$, while the angles ϕ_2 and ϕ_2 can take any of the three values: $(\phi_1, \phi_2) = (0, \pi)$, $(\phi_1, \phi_2) = (-2\pi/3, -\pi/3)$, or $(\phi_1, \phi_2) = (2\pi/3, \pi/3)$. This is indeed the three valley polarized states we found in Eqs. (3.34)-(3.36). A plot of the angular dependence of this functional is shown in Fig. (4.1). We can clearly identify the existence of three minima.

4.3.1.2 Filling factor $\nu = 2$

We now look at the filling factor $\nu = 2$ state. In this state the spins are still polarized as a down state. Numerical iteration yields the following two states as the ground state:

$$|\Psi_{\nu=2}^{(11)}\rangle = \begin{bmatrix}-0.2600 & 0.8011 & 0.5391\end{bmatrix}^\intercal, \quad E_{\nu=2}^{(11)} = -0.2928, \\ |\Psi_{\nu=2}^{(12)}\rangle = \begin{bmatrix}0.7734 & -0.1614 & 0.6130\end{bmatrix}^\intercal, \quad E_{\nu=2}^{(12)} = -0.2923. \tag{4.39}$$

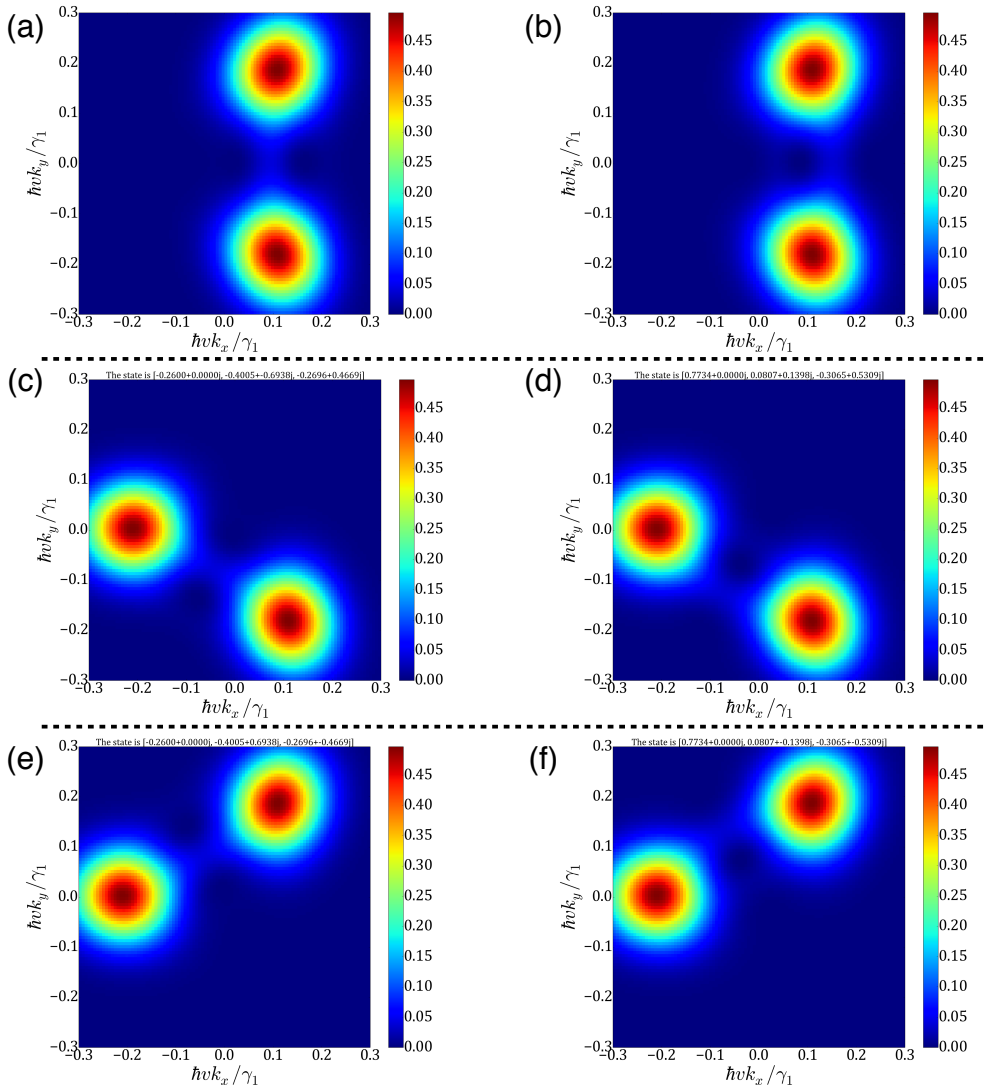

Figure 4.2: Hartree-Fock ground state at filling factor $\nu = 2$. Panels (a)-(b) correspond to the state $\Psi^{(11)}_{\nu=2}$ and $\Psi^{(12)}_{\nu=2}$, (c)-(d) correspond to $\Psi^{(21)}_{\nu=2}$ and $\Psi^{(22)}_{\nu=2}$, and (e)-(f) correspond to $\Psi^{(31)}_{\nu=2}$ and $\Psi^{(32)}_{\nu=2}$.

We can then obtain the other two possibilities by the two unitary transformations in Eq. (3.37):

$$|\Psi^{(21)}_{\nu=2}\rangle = U_-|\Psi^{(11)}_{\nu=2}\rangle = \left[-0.2600 \quad 0.8011e^{-2\pi i/3} \quad 0.5391e^{-4i\pi/3}\right]^\intercal, \quad E^{(11)}_{\nu=2} = -0.2928,$$

$$
\begin{aligned}
|\Psi^{(22)}_{\nu=2}\rangle = U_-|\Psi^{(12)}_{\nu=2}\rangle &= \begin{bmatrix}0.7734 & -0.1614e^{-2i\pi/3} & 0.6130e^{-4i\pi/3}\end{bmatrix}^\intercal, \quad E^{(12)}_{\nu=2} = -0.2923; \\
|\Psi^{(31)}_{\nu=2}\rangle = U_+|\Psi^{(11)}_{\nu=2}\rangle &= \begin{bmatrix}-0.2600 & 0.8011e^{2\pi i/3} & 0.5391e^{4i\pi/3}\end{bmatrix}^\intercal, \quad E^{(11)}_{\nu=2} = -0.2928, \\
|\Psi^{(32)}_{\nu=2}\rangle = U_+|\Psi^{(12)}_{\nu=2}\rangle &= \begin{bmatrix}0.7734 & -0.1614e^{2i\pi/3} & 0.6130e^{4i\pi/3}\end{bmatrix}^\intercal, \quad E^{(12)}_{\nu=2} = -0.2923.
\end{aligned}
\tag{4.40}
$$

An illustration of these ground states is given in Fig. 4.2.

4.3.1.3 Filling factor $\nu = 3$

The filling factor $\nu = 3$ state is quite simple. They are all spin down states, with

$$
\begin{aligned}
|\Psi^{(1)}_{\nu=3}\rangle &= |\Psi_{j=2}, \downarrow\rangle, \quad E^{(1)}_{\nu=3} = -0.3167, \\
|\Psi^{(2)}_{\nu=3}\rangle &= |\Psi_{j=1}, \downarrow\rangle, \quad E^{(2)}_{\nu=3} = -0.3162, \\
|\Psi^{(3)}_{\nu=3}\rangle &= |\Psi_{j=0}, \downarrow\rangle, \quad E^{(3)}_{\nu=3} = -0.3160.
\end{aligned}
\tag{4.41}
$$

4.3.1.4 Filling factor $\nu = 4$, $\nu = 5$, and $\nu = 6$

The filling factor $\nu = 4$ state is built upon the three states at filling factor $\nu = 3$, with the fourth state being a spin-up state, valley polarized, and the energy is -0.2682.

The filling factor $\nu = 5$ state is also built upon the three states at filling factor $\nu = 3$, with the fourth and fifth state repeating the $\nu = 2$ state, although the spin configuration is down. The energy of these two states are -0.2928, and -0.2923, respectively.

The filling factor $\nu = 6$ state manifold contains the following states:

$$
|\Psi^{(1)}_{\nu=6}\rangle = |\Psi_{j=2}, \downarrow\rangle, \quad E^{(1)}_{\nu=6} = -0.3167,
$$

$$
\begin{aligned}
|\Psi^{(2)}_{\nu=6}\rangle &= |\Psi_{j=1},\downarrow\rangle, \quad E^{(2)}_{\nu=6} = -0.31621, \\
|\Psi^{(3)}_{\nu=6}\rangle &= |\Psi_{j=2},\uparrow\rangle, \quad E^{(3)}_{\nu=6} = -0.31616, \\
|\Psi^{(4)}_{\nu=6}\rangle &= |\Psi_{j=0},\downarrow\rangle, \quad E^{(4)}_{\nu=6} = -0.3160, \\
|\Psi^{(5)}_{\nu=6}\rangle &= |\Psi_{j=1},\uparrow\rangle, \quad E^{(5)}_{\nu=6} = -0.3156, \\
|\Psi^{(6)}_{\nu=6}\rangle &= |\Psi_{j=0},\uparrow\rangle, \quad E^{(6)}_{\nu=6} = -0.3154.
\end{aligned} \tag{4.42}
$$

4.3.2 Possible future directions

In this chapter we have explored the quantum Hall ferromagnetism in gapped bilayer graphene with trigonal warping effects, mainly focusing on the small field cases where there exists a three-fold degenerate Landau levels at the top of the valence band. In the future we can explore the phase diagram at higher fields, where the three states are not exactly degenerate, but the spin structure may be more interesting.

Appendix

Appendix A

Useful results for quantum Hall physics

A.1 LL wavefunctions in the symmetric gauge

A.1.1 Working in the symmetric gauge

In this section we are going to develop the general properties of a symmetric gauge Landau-level wavefunctions. The Hamiltonian for the massless Dirac fermions is

$$\mathcal{H} = \hbar v \begin{pmatrix} 0 & k_x - ik_y \\ k_x + ik_y & 0 \end{pmatrix}. \tag{A.1}$$

We will make the usual Peierls substitution that

$$\begin{aligned} \pi_x &= -i\hbar\partial_x + eA_x = -i\hbar\partial_x + \frac{\hbar}{2\ell^2}y, \\ \pi_y &= -i\hbar\partial_y + eA_y = -i\hbar\partial_y - \frac{\hbar}{2\ell^2}x, \end{aligned} \tag{A.2}$$

where we have used the symmetric gauge that $A_x = By/2$, and $A_y = -Bx/2$. The magnetic length is given by $\ell = \sqrt{\hbar/eB} = 25.6\,\mathrm{nm}/\sqrt{B[\mathrm{T}]}$. Under this convention, the commutator between π_x and π_y is

$$[\pi_x, \pi_y] = i\hbar^2/\ell^2. \tag{A.3}$$

We can then define the complex variable z as

$$z = \frac{1}{2\ell}(x + iy), \quad z^* = \frac{1}{2\ell}(x - iy). \tag{A.4}$$

Therefore, the coordinates x and y can be inverted to be

$$x = \ell(z + z^*), \quad y = -i\ell(z - z^*). \tag{A.5}$$

The spatial derivatives work as follows,

$$\partial_z = \ell(\partial_x - i\partial_y), \partial_x = (\partial_z + \partial_{z^*})/(2\ell), \tag{A.6}$$

$$\partial_{z^*} = \ell(\partial_x + i\partial_y), \partial_y = (\partial_z - \partial_{z^*})/(2\ell). \tag{A.7}$$

As a result, the π_x and π_y can be written in terms of z and z^* as follows,

$$\begin{aligned} \pi_x &= \frac{-i\hbar}{2\ell}\left(\partial_z + \partial_{z^*} + z - z^*\right), \\ i\pi_y &= \frac{i\hbar}{2\ell}\left(\partial_z - \partial_{z^*} - z - z^*\right). \end{aligned} \tag{A.8}$$

A.1.2 Two sets of creation and annihilation operators

We can then define one set of creation and annihilation operators a and $a^\dagger$ as follows,

$$a = \frac{\ell}{\sqrt{2}\hbar}(\pi_x + i\pi_y). \tag{A.9}$$

They satisfy the relation that $[a, a^\dagger] = 1$. They can be written in terms of z and z^* as follows,

$$a = -\frac{i}{\sqrt{2}}(z + \partial_{z^*}), \quad a^\dagger = \frac{i}{\sqrt{2}}(z^* - \partial_z). \tag{A.10}$$

It turns out that this set of operators correspond to the relative motion between the electrons. We can also define another set of creation and annihilation

operators, which correspond to the guiding centers of the cyclotron motion. From the classical solution, we learn that the guiding centers are given by

$$C_x = x + \frac{\ell^2}{\hbar}\pi_y, \quad C_y = y - \frac{\ell^2}{\hbar}\pi_x, \tag{A.11}$$

which satisfy the commutation relation that

$$[C_x, C_y] = -i\ell^2. \tag{A.12}$$

Here we have introduced the *relative coordinates* $\boldsymbol{R}$,

$$\boldsymbol{R} = \left(-\frac{\ell^2}{\hbar}\pi_y, \frac{\ell^2}{\hbar}\pi_x\right), \tag{A.13}$$

So that the relative coordinates $\boldsymbol{R}$, guiding center $\boldsymbol{C}$, and the local coordinates $\boldsymbol{r}$ are related by $\boldsymbol{C} = \boldsymbol{r} - \boldsymbol{R}$.

The complex number C is defined as follows,

$$C = C_x + iC_y = 2\ell z - \sqrt{2}i\ell a. \tag{A.14}$$

The second set of creation and annihilation operators are thus given by

$$b^\dagger = \frac{1}{\sqrt{2}\ell}C = \sqrt{2}z - ia, \quad b = \sqrt{2}z^* + ia^\dagger. \tag{A.15}$$

It is easy to verify that

$$b = \frac{1}{\sqrt{2}}\left(z^* + \partial_z\right), \quad b^\dagger = \frac{1}{\sqrt{2}}\left(z - \partial_{z^*}\right), \tag{A.16}$$

and that they satisfy $[b, b^\dagger] = 1$. In addition, we note that the two sets of operators a and b commute with each other.

The ground state (lowest Landau level) of a traditional 2DEG is the one that is annihilated by the operator a, $a|\psi_0\rangle = 0$. If we bring it to the coordinate representation,

$$0 = \langle z|a|\psi_0\rangle = \frac{-i}{\sqrt{2}}\left(z + \frac{\partial}{\partial z^*}\right)\psi_0(z). \tag{A.17}$$

The general solution will be

$$\psi_0(z) = \lambda(z)e^{-zz^*}. \tag{A.18}$$

This energy level is hugely degenerate, and we can choose the ground state as the one being annihilated by the operator b, i.e.,

$$0 = \langle z|b|\psi_0\rangle = \frac{1}{\sqrt{2}}\left(z^* + \frac{\partial}{\partial z}\right)\psi_0(z), \tag{A.19}$$

which yields $\lambda(z) =$ constant. Therefore, the ground state of the Landau levels is given by

$$\langle z|0,0\rangle = \psi_0(z) = \lambda e^{-zz^*}. \tag{A.20}$$

The constant λ is found by the normalization condition,

$$\frac{1}{2\pi\lambda^2\ell^2} = \int_0^\infty d\xi\xi \exp\left[-\frac{\xi^2}{2}\right] = 1. \tag{A.21}$$

The exact ground state wavefunction is therefore

$$\langle z|0,0\rangle = \psi_0(z) = \frac{1}{\sqrt{2\pi\ell^2}}e^{-r^2/4\ell^2}. \tag{A.22}$$

Finally, all states in the LLs can be generated by the $a^\dagger$ and $b^\dagger$ operators,

$$|N,m\rangle = \frac{(a^\dagger)^N(b^\dagger)^m}{\sqrt{N!m!}}|0,0\rangle. \tag{A.23}$$

A.2 LL wavefunctions in the Landau gauge

In this section we list some of the useful properties of the Landau gauge wavefunctions. Assume we take the vector potential to be $\boldsymbol{A} = (0, Bx, 0)$, the corresponding wavefunction for the nth Landau level is given by

$$\phi_n(x, y) = \frac{1}{\sqrt{2\pi\hbar}} e^{ik_y y} \eta_n(x + k_y \ell^2), \tag{A.24}$$

where $\ell^2 = \hbar/eB$ is the magnetic length, and the function $\eta_n(\xi)$ is given by

$$\eta_n(\xi) = (2^n \ell n! \sqrt{\pi})^{-1/2} e^{-\xi^2/2} H_n(\xi),\ \xi = x/\ell. \tag{A.25}$$

These wavefunctions form a orthonormal set, i.e.,

$$\langle \phi_n | \phi_m \rangle \equiv \int_{-\infty}^{\infty} \phi_m^*(\boldsymbol{r}) \phi_n(\boldsymbol{r}) = \delta_{m,n}. \tag{A.26}$$

A.3 Calculation of the pseudopotentials

We now consider how to calculate the pseudopotentials. We will start from the case in conventional 2DEG, and then to graphene, and finally onto our current model.

A.3.1 Pseudopotentials in 2DEG: formalism

We first note that it is often sufficient to consider the electrons within a particular Landau level with index N. The operator that destroys an electron in the Nth LL is

$$\psi(\boldsymbol{r}) = \sum_m \langle \boldsymbol{r} | N, m \rangle c_{N,m}. \tag{A.27}$$

The density operator for the Nth LL is then given by

$$\rho_N(\boldsymbol{r}) = \psi^\dagger(\boldsymbol{r})\psi(\boldsymbol{r}) = \sum_{m_1,m_2} \langle m_1 N|\boldsymbol{r}\rangle\langle \boldsymbol{r}|Nm_2\rangle c^\dagger_{m_1} c_{m_2}, \tag{A.28}$$

where we have omitted the common index N in the operators c. In future it is understood that all operators belong to the Nth LL, unless noted otherwise. Finally, the Fourier transform of the projected density is given by

$$\begin{aligned}\rho_N(\boldsymbol{q}) &= \frac{1}{2\pi}\int d^2\boldsymbol{r}\rho_N(\boldsymbol{r})e^{-i\boldsymbol{q}\cdot\boldsymbol{r}} \\ &= \frac{1}{2\pi}\int d^2\boldsymbol{r}\sum_{m_1 m_2}\langle Nm_1|\boldsymbol{r}\rangle e^{-i\boldsymbol{q}\cdot\boldsymbol{r}}\langle\boldsymbol{r}|Nm_2\rangle c^\dagger_{m_1}c_{m_2}.\end{aligned} \tag{A.29}$$

To further simplify the above result, we note that

$$e^{-i\boldsymbol{q}\cdot\hat{\boldsymbol{r}}} = \int d^2\boldsymbol{r}e^{-i\boldsymbol{q}\cdot\hat{\boldsymbol{r}}}|\boldsymbol{r}\rangle\langle\boldsymbol{r}| = \int d^2\boldsymbol{r}|\boldsymbol{r}\rangle e^{-i\boldsymbol{q}\cdot\boldsymbol{r}}\langle\boldsymbol{r}|, \tag{A.30}$$

where $\hat{\boldsymbol{r}}$ is the coordinate *operator*, while $\boldsymbol{r}$ is just the coordinate. Thus, the result in Eq. (A.29) simplifies to

$$\rho_N(\boldsymbol{q}) = \frac{1}{2\pi}\sum_{m_1 m_2}\langle Nm_1|e^{-i\boldsymbol{q}\cdot\hat{\boldsymbol{r}}}|Nm_2\rangle c^\dagger_{m_1}c_{m_2}. \tag{A.31}$$

The argument of the exponent can be decomposed into the guiding center and relative coordinates defined in Eq. (A.13), and the matrix element is then rewritten as

$$\rho_N(\boldsymbol{q}) = \mathcal{F}_N(\boldsymbol{q})\frac{1}{2\pi}\sum_{m_1 m_2}\langle m_1|e^{-i\boldsymbol{q}\cdot\boldsymbol{C}}|m_2\rangle c^\dagger_{m_1}c_{m_2}, \tag{A.32}$$

where $\mathcal{F}_N(\boldsymbol{q})$ is the *form factor* of the Nth LL, independent of m_1 or m_2,

$$\mathcal{F}_N(\boldsymbol{q}) = \langle N|e^{-i\boldsymbol{q}\cdot\boldsymbol{R}}|N\rangle. \tag{A.33}$$

We can also define the *bare density operator* $\hat{\rho}(\boldsymbol{q})$,

$$\hat{\rho}(\boldsymbol{q}) = \frac{1}{2\pi} \sum_{m_1 m_2} \langle m_1 | e^{-i\boldsymbol{q}\cdot\boldsymbol{C}} | m_2 \rangle c^\dagger_{m_1} c_{m_2}, \tag{A.34}$$

which is identical for any LL. Therefore, the projected density, or the physical density $\rho_N(\boldsymbol{q})$ is given by

$$\rho_N(\boldsymbol{q}) = \mathcal{F}_N(\boldsymbol{q})\hat{\rho}(\boldsymbol{q}). \tag{A.35}$$

A.3.2 Pseudopotentials in graphene: the pseudospin structure

We now proceed to the calculation of pseudopotentials in graphene, in particular, single-layer graphene. The single-particle LL reads $\psi_\sigma(\boldsymbol{r}) = \exp(i\sigma \boldsymbol{K}\cdot\boldsymbol{r})\chi_\sigma(\boldsymbol{r})$, where $\sigma = \pm$ labels the two valleys, and $\chi_\sigma(\boldsymbol{r})$ is

$$\begin{aligned}
\chi_+(\boldsymbol{r}) &= \frac{1}{\sqrt{2}} \sum_{n,m} \begin{bmatrix} i\sqrt{1+\delta_{n,0}}\langle \boldsymbol{r}||n|,m\rangle \\ \mathrm{sgn}(n)\langle \boldsymbol{r}||n|-1,m\rangle \end{bmatrix} c_{n,m,+}, \\
\chi_-(\boldsymbol{r}) &= \frac{1}{\sqrt{2}} \sum_{n,m} \begin{bmatrix} \mathrm{sgn}(n)\langle \boldsymbol{r}||n|-1,m\rangle \\ i\sqrt{1+\delta_{n,0}}\langle \boldsymbol{r}||n|,m\rangle \end{bmatrix} c_{n,m,-},
\end{aligned} \tag{A.36}$$

The $|n,m\rangle$ is the non-relativistic one-particle states for a charged particles in a perpendicular magnetic field, and n is the LL index for graphene. Note that the structure of the $n = 0$ LL is special, because it is the only one that does not contain a mixture of two non-relativistic LLs.

A.3.3 Projected density operator in graphene

We can now compute the projected density. We first consider the projection onto the state with $N \neq 0$,

$$\rho_{N,\sigma_1\sigma_2} = \psi^\dagger_{N,\sigma_1}\psi_{N,\sigma_2}, \tag{A.37}$$

where $\psi_{N,\sigma}$ indicates we will only keep the terms with $c_{N,m,\sigma}$ in the summation in Eq. (A.36). For simplicity, we will omit the index N hereafter.

Due to the pseudospin structure, the projected density will be a matrix in the pseudospin basis. The diagonal entry is given by

$$\rho^{++}(\boldsymbol{q}) = \mathcal{F}_N^{++}(\boldsymbol{q})\hat{\rho}^{++}(\boldsymbol{q}), \tag{A.38}$$

where the *bare density* is given by

$$\hat{\rho}^{++}(\boldsymbol{q}) = \frac{1}{2\pi}\sum_{m_1 m_2}\langle m_1|e^{-i\boldsymbol{q}\cdot\boldsymbol{C}}|m_2\rangle c_{m_1}^\dagger c_{m_2}, \tag{A.39}$$

and the form factor is

$$\mathcal{F}_N^{++}(\boldsymbol{q}) = \frac{1}{2}\left[L_N\left(\frac{q^2\ell^2}{2}\right) + L_{N-1}\left(\frac{q^2\ell^2}{2}\right)\right]e^{-q^2\ell^2/4}. \tag{A.40}$$

On the other hand, the off-diagonal entry is given by

$$\rho^{+-}(\boldsymbol{q}) = \mathcal{F}_N^{+-}(\boldsymbol{q})\hat{\rho}^{+-}(\boldsymbol{q}), \tag{A.41}$$

where the *bare density* is given by

$$\hat{\rho}^{+-}(\boldsymbol{q}) = \frac{1}{2\pi}\sum_{m_1 m_2}\langle m_1|e^{-i\boldsymbol{Q}\cdot\boldsymbol{C}}|m_2\rangle c_{m_1}^\dagger c_{m_2}, \tag{A.42}$$

where $\boldsymbol{Q} = \boldsymbol{q} + 2\boldsymbol{K}$. The form factor $\mathcal{F}_N^{+-}(\boldsymbol{q})$ is given by

$$\mathcal{F}_N^{+-}(\boldsymbol{q}) = \frac{i\mathrm{sgn}(N)}{2}\left[\langle N-1|e^{-i\boldsymbol{Q}\cdot\boldsymbol{R}}|N\rangle - \langle N|e^{-i\boldsymbol{Q}\cdot\boldsymbol{R}}|N-1\rangle\right]. \tag{A.43}$$

Appendix B

Form factors in quantum Hall ferromagnetism

In this appendix we are going to derive the expression for the form factor of Landau levels, which plays a key role in treating electron-electron interactions in the quantum Hall regime [8].

B.1 Derivations in the Landau gauge

In this section we are going to derive the form factor for Landau levels in the Landau gauge. The single-particle LL wave function is given by

$$\langle \boldsymbol{r}|n_2X_2\rangle = \frac{1}{\sqrt{L_y}}e^{iX_2y/\ell^2}\phi_{n_2}(x-X_2), \tag{B.1}$$

where the function $\phi_{n_2}(x-X_2)$ is given by

$$\phi_{n_2}(x-X_2) = \frac{1}{(\sqrt{\pi}\ell 2^{n_2}n_2!)^{1/2}}e^{-(x-X_2)^2/\ell^2}H_{n_2}[(x-x_2)/\ell]. \tag{B.2}$$

The form factor is defined as

$$\langle n_1X_1|e^{i\boldsymbol{q}\cdot\boldsymbol{r}_{\rm op}}|n_2X_2\rangle = \int_{-\infty}^{\infty}dx\phi_{n_1}(x-X_1)\phi_{n_2}(x-X_2)e^{iq_xx}\delta_{X_1,X_2+q_y\ell^2}. \tag{B.3}$$

This is obtained by inserting $1 = \int d\boldsymbol{r}|\boldsymbol{r}\rangle\langle\boldsymbol{r}|$ into the above equation and completing the integration over y. It is further simplified as follows,

$$\langle n_1X_1|e^{i\boldsymbol{q}\cdot\boldsymbol{r}_{\rm op}}|n_2X_2\rangle = \frac{1}{\sqrt{\pi}\ell\sqrt{2^{n_1+n_2}n_1!n_2!}}\int_{-\infty}^{\infty}d(z\ell)e^{iq_x\ell z}e^{-\frac{1}{2}[(z-z_1)^2+(z-z_2)^2]}$$

$$\cdot H_{n_1}(z-z_1)H_{n_2}(z-z_2)\delta_{z_1,z_2+q_y\ell},$$

where we have defined a dimensionless variable $z_i = X_i/\ell$. To proceed, we first deal with the argument of the two exponential functions,

$$-\frac{1}{2}[(z-z_1)^2+(z-z_2)^2]+iq_x\ell z = -\frac{1}{4}(q_x^2\ell^2+q_y^2\ell^2)+\frac{i}{2}q_x\ell(z_1+z_2)-(z-z_0)^2,$$

where we have defined $z_0 = z_2+(q_y+iq_x)\ell/2$. Also it is convenient to introduce a new variable $Z = z - z_0$. As a result,

$$z_0 - z_2 = (q_y+iq_x)\ell/2,\ z_0 - z_1 = (-q_y+iq_x)\ell/2. \tag{B.4}$$

The above form factor can be written formally as

$$\langle n_1X_1|e^{i\boldsymbol{q}\cdot\boldsymbol{r}_{\rm op}}|n_2X_2\rangle = \frac{\delta_{X_1,X_2+q_y\ell^2}}{\sqrt{\pi 2^{n_1+n_2}n_1!n_2!}}e^{\frac{i}{2}q_x(X_1+X_2)}e^{-q^2\ell^2/4}I_0, \tag{B.5}$$

where $q^2 \equiv q_x^2+q_y^2$. I_0 will be the focus of our calculations below, given by

$$I_0 = \int_{-\infty}^{+\infty} dZe^{-Z^2}H_{n_1}(Z+z_0-z_1)H_{n_2}(Z+z_0-z_2). \tag{B.6}$$

To proceed further we note that

$$H_n(x+y) = \sum_{k=0}^{n}\binom{n}{k}H_k(x)(2y)^{n-k},\quad \binom{n}{k} = \frac{n!}{k!(n-k)!}. \tag{B.7}$$

The above integral is then rewritten as

$$I_0 = \sum_{k_1=0}^{n_1}\sum_{k_2=0}^{n_2}\binom{n_1}{k_1}\binom{n_2}{k_2}(iq_x\ell-q_y\ell)^{n_1-k_1}(iq_x\ell+q_y\ell)^{n_2-k_2}\int_{-\infty}^{\infty}dZH_{k_1}(Z)H_{k_2}(Z)e^{-Z^2}.$$

We can then make use of the orthonormal relation of Hermite polynomials,

$$\int_{-\infty}^{\infty}dze^{-z^2}H_{k_1}(z)H_{k_2}(z) = \sqrt{\pi}2^{k_1}k_1!\delta_{k_1k_2}. \tag{B.8}$$

The expression for I_0 is then simplified to

$$I_0 = \sum_{k_1=0}^{n_1} \sum_{k_2=0}^{n_2} \binom{n_1}{k_1} \binom{n_2}{k_2} (iq_x\ell - q_y\ell)^{n_1-k_1} (iq_x\ell + q_y\ell)^{n_2-k_2} \delta_{k_1 k_2} \sqrt{\pi} 2^{k_1} k_1!. \tag{B.9}$$

We now assume that $n_1 \geq n_2$, and use the delta function to kill one summation. As a result, we have

$$I_0 = \sqrt{\pi}(iq_x\ell - q_y\ell)^{n_1-n_2} \sum_{k=0}^{n_2} \binom{n_1}{k} \binom{n_2}{k} 2^k k! (-q^2\ell^2)^{n_2-k}. \tag{B.10}$$

Finally, we recall that the definition for the Laguerre polynomial is

$$L_n^{(\alpha)}(x) = \sum_{t=0}^{n} \frac{(-x)^t}{t!} \binom{n+\alpha}{n-t}, \tag{B.11}$$

which indicates that

$$L_{n_2}^{n_1-n_2}(q^2\ell^2/2) = \sum_{t=0}^{n_2} \frac{(-q^2\ell^2/2)^t}{t!} \binom{n_2+n_1-n_2}{n_2-t} = \sum_{k=0}^{n_2} \frac{(-q^2\ell^2/2)^{n_2-k}}{(n_2-k)!} \binom{n_1}{k}. \tag{B.12}$$

In the last step we have changed the variable to $k = n_2 - t$. Now the expression for I_0 can be simplified as follows,

$$\begin{aligned} I_0 &= \sqrt{\pi}(iq_x\ell - q_y\ell)^{n_1-n_2} \sum_{k=0}^{n_2} \binom{n_1}{k} \frac{(-q^2\ell^2/2)^{n_2-k}}{(n_2-k)!} \cdot 2^{n_2-k}(n_2-k)! \binom{n_2}{k} 2^k k! \\ &= \sqrt{\pi}(iq_x\ell - q_y\ell)^{n_1-n_2} 2^{n_2} n_2! L_{n_2}^{n_1-n_2}(q^2\ell^2/2). \end{aligned} \tag{B.13}$$

Now if we consider the case with $n_1 < n_2$, the results in Eq. (B.9) are rewritten as

$$I_0 = \sqrt{\pi}(iq_x\ell + q_y\ell)^{n_2-n_1} \sum_{k=0}^{n_1} \binom{n_1}{k} \binom{n_2}{k} 2^k k! (-q^2\ell^2)^{n_1-k}, \tag{B.14}$$

and similar results can be obtained.

If we insert the above results back to Eq. (B.5), we finally obtain for $n_1 \geq n_2$,

$$\begin{aligned}\langle n_1 X_1 | e^{i\boldsymbol{q}\cdot\boldsymbol{r}_{\rm op}} | n_2 X_2 \rangle &= \delta_{X_1, X_2+q_y\ell^2} e^{\frac{i}{2}q_x(X_1+X_2)} e^{-q^2\ell^2/4} \\ &\quad \cdot \sqrt{\frac{n_2!}{n_1!}} \left(\frac{iq_x\ell - q_y\ell}{\sqrt{2}}\right)^{n_1-n_2} L_{n_2}^{n_1-n_2}(q^2\ell^2/2),\end{aligned}$$

while for $n_1 < n_2$ we have

$$\begin{aligned}\langle n_1 X_1 | e^{i\boldsymbol{q}\cdot\boldsymbol{r}_{\rm op}} | n_2 X_2 \rangle &= \delta_{X_1, X_2+q_y\ell^2} e^{\frac{i}{2}q_x(X_1+X_2)} e^{-q^2\ell^2/4} \\ &\quad \cdot \sqrt{\frac{n_1!}{n_2!}} \left(\frac{iq_x\ell + q_y\ell}{\sqrt{2}}\right)^{n_2-n_1} L_{n_1}^{n_2-n_1}(q^2\ell^2/2).\end{aligned}$$

B.2 Derivations in the symmetric gauge

We now derive the same result in the symmetric gauge. We first define a complex number q that represents the 2D momentum,

$$\tilde{q} = \ell(\eta q_x + i\eta^{-1} q_y). \tag{B.15}$$

Also we define the complex number R that represents the relative vector $\boldsymbol{R}$ as

$$\tilde{R} = \frac{1}{2\ell}(\eta^{-1} R_x + i\eta R_y) = \frac{i}{\sqrt{2}} a. \tag{B.16}$$

Therefore, the argument of the exponent is given by

$$\begin{aligned}\boldsymbol{q}\cdot\boldsymbol{R} &= q_x R_x + q_y R_y = \tilde{q}\tilde{R}^* + \tilde{q}^*\tilde{R} \\ &= \frac{i}{\sqrt{2}}(\tilde{q}^* a - \tilde{q} a^\dagger).\end{aligned} \tag{B.17}$$

Therefore, the exponent in the form factor can be decomposed into two parts,

$$e^{-i\boldsymbol{q}\cdot\boldsymbol{R}} = e^{\frac{i}{\sqrt{2}}(\tilde{q}^* a - \tilde{q} a^\dagger)} = \exp\left[\frac{-\tilde{q}a^\dagger}{\sqrt{2}}\right] \exp\left[\frac{\tilde{q}^* a}{\sqrt{2}}\right] e^{-|\tilde{q}|^2/4}, \tag{B.18}$$

where we have used the identity that when $[A, B]$ is a c-number,

$$e^{A+B} = e^B e^A e^{[A,B]/2}, \tag{B.19}$$

The form factor can now be evaluated to be

$$\mathcal{F}_N(\boldsymbol{q}) = \frac{1}{N!}\langle 0|a^N e^{-\tilde{q}a^\dagger/\sqrt{2}} e^{\tilde{q}^* a/\sqrt{2}} \left(a^\dagger\right)^N |0\rangle e^{-|\tilde{q}|^2/4}.$$

For the lowest LL ($N = 0$), it is found that

$$\mathcal{F}_0(\boldsymbol{q}) = e^{-|\tilde{q}|^2/4}. \tag{B.20}$$

In the limit of $\eta = 1$, it reduces to the familiar result $\mathcal{F}_0(\boldsymbol{q}) = e^{-q^2\ell^2/4}$. Note the difference between $|\tilde{q}|^2$ and q^2, where the latter is $q^2 = q_x^2 + q_y^2$. In general, the form factor is given by

$$\mathcal{F}_N(\boldsymbol{q}) = L_N\left(\frac{|\tilde{q}|^2}{2}\right) e^{-|\tilde{q}|^2/4}, \tag{B.21}$$

where $L_N(x)$ is the Laguerre polynomial.

Publication List

1. **Xiao Li**, Fan Zhang, Qian Niu, and A. H. MacDonald, *Quantum Hall effects in topological crystalline insulator surface states*, in preparation (2014).

2. Fan Zhang, **Xiao Li**, Ji Feng, C. L. Kane, and E. J. Mele, *Zeeman field-tuned transitions for surface Chern insulators*, eprint **arXiv**:1309.7682 (2013).

3. **Xiao Li**, Fan Zhang, Qian Niu, and A. H. MacDonald, *Spontaneous layer-pseudospin domain walls in bilayer graphene*, **Phys. Rev. Lett.** 113, 116803 (2014).

4. RuiLin Chu, **Xiao Li**, Sanfeng Wu, Qian Niu, Xiaodong Xu, and Chuanwei Zhang, *Valley-splitting and valley-dependent inter-Landau-level optical transitions in monolayer MoS_2 quantum Hall systems*, **Phys. Rev. B** 90, 045427 (2014).

5. Tianyi Cai, Shengyuan A. Yang, **Xiao Li**, Fan Zhang, Junren Shi, Wang Yao, and Qian Niu, *Magnetic control of the valley degree of freedom of massive Dirac fermions with application to transition metal dichalcogenides*, **Phys. Rev. B** 88, 115140 (2013).

6. Zhenhua Qiao, **Xiao Li**, Wang-Kong Tse, Hua Jiang, Yugui Yao, and Qian Niu, *Topological phases in gated bilayer graphene: effects of Rashba spin-orbit coupling and exchange field*, **Phys. Rev. B** 87, 125405 (2013).

7. **Xiao Li**, Fan Zhang, and Qian Niu, *Unconventional quantum Hall effect and tunable spin Hall effect in Dirac materials: application to an isolated MoS2 trilayer*, **Phys. Rev. Lett.** 110, 066803 (2013).

8. **Xiao Li**, Zhenhua Qiao, Jeil Jung, and Qian Niu, *Unbalanced edge modes and topological phase transition in gated trilayer graphene*, **Phys. Rev. B** 85, 201404(R) (2012).

9. Zhenhua Qiao, Hua Jiang, **Xiao Li**, Yugui Yao, and Qian Niu, *Microscopic theory of quantum anomalous Hall effect in graphene*, **Phys. Rev. B** 85, 115439 (2012).

Bibliography

[1] D. Abergel, J. Berashevich, K. Ziegler, and T. Chakraborty. Properties of graphene: a theoretical perspective. *Adv. Phys.*, 59(4):261–482, Aug. 2010.

[2] J. S. Alden, A. W. Tsen, P. Y. Huang, R. Hovden, L. Brown, J. Park, D. A. Muller, and P. L. McEuen. Strain solitons and topological defects in bilayer graphene. *Proc. Natl. Acad. Sci. USA*, 110(28):11256–11260, July 2013.

[3] T. Cao, G. Wang, W. Han, H. Ye, C. Zhu, J. Shi, Q. Niu, P. Tan, E. Wang, B. Liu, and J. Feng. Valley-selective circular dichroism of monolayer molybdenum disulphide. *Nat. Commun.*, 3:887, 2012.

[4] A. H. Castro Neto, N. M. R. Peres, K. S. Novoselov, and A. K. Geim. The electronic properties of graphene. *Rev. Mod. Phys.*, 81(1):109–162, Jan. 2009.

[5] P. M. Chaikin and T. C. Lubensky. *Principles of Condensed Matter Physics*. Cambridge University Press, reprint edition, Sept. 2000.

[6] J. G. Checkelsky, L. Li, and N. Ong. Zero-Energy State in Graphene in a High Magnetic Field. *Phys. Rev. Lett.*, 100(20):206801, May 2008.

[7] A. M. Cook, C. Hickey, and A. Paramekanti. Emergent dome of nematic order around a quantum anomalous Hall critical point. *Phys. Rev. B*, 90(8):085145, Aug. 2014.

[8] R. Cote and A. H. MacDonald. Collective modes of the two-dimensional Wigner crystal in a strong magnetic field. *Phys. Rev. B*, 44(16):8759–8773, Oct. 1991.

[9] V. Cvetkovic, R. E. Throckmorton, and O. Vafek. Electronic multicriticality in bilayer graphene. *Phys. Rev. B*, 86(7):075467, Aug. 2012.

[10] G. Dávid, P. Rakyta, L. Oroszlány, and J. Cserti. Effect of the band structure topology on the minimal conductivity for bilayer graphene with symmetry breaking. *Phys. Rev. B*, 85(4):041402, Jan. 2012.

[11] X. Du, I. Skachko, F. Duerr, A. Luican, and E. Y. Andrei. Fractional quantum Hall effect and insulating phase of Dirac electrons in graphene. *Nature*, 462(7):192–195, Nov. 2009.

[12] G. A. Farias and F. M. Peeters. Chiral states in bilayer graphene: Magnetic field dependence and gap opening. *Phys. Rev. B*, 84(12):125451, Sept. 2011.

[13] F. Freitag, J. Trbovic, M. Weiss, and C. Schönenberger. Spontaneously Gapped Ground State in Suspended Bilayer Graphene. *Phys. Rev. Lett.*, 108(7):076602, Feb. 2012.

[14] F. Freitag, M. Weiss, R. Maurand, J. Trbovic, and C. Schönenberger. Spin symmetry of the bilayer graphene ground state. *Phys. Rev. B*, 87(16):161402, Apr. 2013.

[15] M. Glasser and N. Horing. Ground-state energy of a two-dimensional electron gas in a magnetic field: Hartree-Fock approximation. *Phys. Rev. B*, 31(7):4603–4611, Apr. 1985.

[16] M. O. Goerbig, R. Moessner, and B. Douçot. Electron interactions in graphene in a strong magnetic field. *Phys. Rev. B*, 74(16):161407, Oct. 2006.

[17] E. V. Gorbar, V. Gusynin, V. A. Miransky, and I. A. Shovkovy. Coexistence and competition of nematic and gapped states in bilayer graphene. *Phys. Rev. B*, 86(12):125439, Sept. 2012.

[18] J. Jung, F. Zhang, and A. H. MacDonald. Lattice theory of pseudospin ferromagnetism in bilayer graphene: Competing interaction-induced quantum Hall states. *Phys. Rev. B*, 83(11):115408, Mar. 2011.

[19] J. Jung, F. Zhang, Z. Qiao, and A. H. MacDonald. Valley-Hall kink and edge states in multilayer graphene. *Phys. Rev. B*, 84(7):075418, Aug. 2011.

[20] C. L. Kane and E. J. Mele. Quantum Spin Hall Effect in Graphene. *Phys. Rev. Lett.*, 95(22):226801, Nov. 2005.

[21] M. Kharitonov. Antiferromagnetic state in bilayer graphene. *Phys. Rev. B*, 86(19):195435, Nov. 2012.

[22] M. Killi, T.-C. Wei, I. Affleck, and A. Paramekanti. Tunable Luttinger Liquid Physics in Biased Bilayer Graphene. *Phys. Rev. Lett.*, 104(2):216406, May 2010.

[23] T. C. Lang, Z. Y. Meng, M. M. Scherer, S. Uebelacker, F. F. Assaad, A. Muramatsu, C. Honerkamp, and S. Wessel. Antiferromagnetism in the Hubbard Model on the Bernal-Stacked Honeycomb Bilayer. *Phys. Rev. Lett.*, 109(12):126402, Sept. 2012.

[24] Y. Lee, D. Tran, K. Myhro, J. J. Velasco, N. Gillgren, C. N. Lau, Y. Barlas, J. M. Poumirol, D. Smirnov, and F. Guinea. Giant Interaction-Induced Gap and Electronic Phases in Rhombohedral Trilayer Graphene. *arxiv.org*, page 6413, Feb. 2014.

[25] Y. Lemonik, I. Aleiner, and V. I. Fal'ko. Competing nematic, antiferromagnetic, and spin-flux orders in the ground state of bilayer graphene. *Phys. Rev. B*, 85(24):245451, June 2012.

[26] Y. Lemonik, I. Aleiner, C. Toke, and V. I. Fal'ko. Spontaneous symmetry breaking and Lifshitz transition in bilayer graphene. *Phys. Rev. B*, 82(20):201408, Nov. 2010.

[27] J. Li, I. Martin, M. Büttiker, and A. F. Morpurgo. Topological origin of

subgap conductance in insulating bilayer graphene. *Nat. Phys.*, 7(1):38–42, Nov. 2010.

[28] X. Li, Z. Qiao, J. Jung, and Q. Niu. Unbalanced edge modes and topological phase transition in gated trilayer graphene. *Phys. Rev. B*, 85(20):201404, May 2012.

[29] X. Li, F. Zhang, and Q. Niu. Unconventional Quantum Hall Effect and Tunable Spin Hall Effect in Dirac Materials: Application to an Isolated MoS_2 Trilayer. *Phys. Rev. Lett.*, 110(6):066803, Feb. 2013.

[30] X. Li, F. Zhang, Q. Niu, and A. H. MacDonald. Spontaneous Layer-Pseudospin Domain Walls in Bilayer Graphene. *Phys. Rev. Lett.*, 113(11):116803, Sept. 2014.

[31] A. H. MacDonald, J. Jung, and F. Zhang. Pseudospin order in monolayer, bilayer and double-layer graphene. *Physica Scripta*, 146:4012, Jan. 2012.

[32] A. H. MacDonald and D. Ritchie. Hydrogenic energy levels in two dimensions at arbitrary magnetic fields. *Phys. Rev. B*, 33(12):8336–8344, June 1986.

[33] P. Maher, L. Wang, Y. Gao, C. Forsythe, T. Taniguchi, K. Watanabe, D. Abanin, Z. Papić, P. Cadden-Zimansky, J. Hone, P. Kim, and C. R. Dean. Bilayer graphene. Tunable fractional quantum Hall phases in bilayer graphene. *Science*, 345(6192):61–64, July 2014.

[34] K. F. Mak, K. He, J. Shan, and T. F. Heinz. Control of valley polarization in monolayer MoS_2 by optical helicity. *Nat. Nanotech.*, 7(8):494–498, Aug. 2012.

[35] I. Martin, A. F. Morpurgo, and Y. Blanter. Topological Confinement in Bilayer Graphene. *Phys. Rev. Lett.*, 100(3):036804, Jan. 2008.

[36] A. S. Mayorov, D. C. Elias, M. Mucha-Kruczyński, R. V. Gorbachev, T. Tudorovskiy, A. A. Zhukov, S. V. Morozov, M. I. Katsnelson, V. I. Fal'ko, A. K. Geim, and K. S. Novoselov. Interaction-Driven Spectrum Reconstruction in Bilayer Graphene. *Science*, 333(6044):860–863, Aug. 2011.

[37] E. McCann and V. I. Fal'ko. Landau-Level Degeneracy and Quantum Hall Effect in a Graphite Bilayer. *Phys. Rev. Lett.*, 96(8):086805, Mar. 2006.

[38] E. McCann and M. Koshino. Trigonal warping and Berry's phase Nπ in ABC-stacked multilayer graphene. *Phys. Rev. B*, 80(16):165409, Oct. 2009.

[39] E. McCann, D. Smirnov, W. Bao, L. Jing, J. Velasco, Y. Lee, G. Liu, D. Tran, B. Standley, M. Aykol, S. B. Cronin, M. Koshino, M. Bockrath, and C. N. Lau. Stacking-dependent band gap and quantum transport in trilayer graphene. *Nat. Phys.*, 7(12):948–952, Sept. 2011.

[40] H. Min and A. H. MacDonald. Chiral decomposition in the electronic structure of graphene multilayers. *Phys. Rev. B*, 77(15):155416, Apr. 2008.

[41] H. Min, A. H. MacDonald, G. Borghi, and M. Polini. Pseudospin magnetism in graphene. *Phys. Rev. B*, 77(4):041407, 2008.

[42] R. Nandkishore and L. S. Levitov. Dynamical Screening and Excitonic Instability in Bilayer Graphene. *Phys. Rev. Lett.*, 104(15):156803, Apr. 2010.

[43] R. Nandkishore and L. S. Levitov. Electron interactions in bilayer graphene: Marginal Fermi liquid and zero-bias anomaly. *Phys. Rev. B*, 82(11):115431, Sept. 2010.

[44] R. Nandkishore and L. S. Levitov. Quantum anomalous Hall state in bilayer graphene. *Phys. Rev. B*, 82(11):115124, Sept. 2010.

[45] Q. Niu, D. Xiao, and W. Yao. Valley-Contrasting Physics in Graphene: Magnetic Moment and Topological Transport. *Phys. Rev. Lett.*, 99(23):236809, Dec. 2007.

[46] K. S. Novoselov, E. McCann, U. Zeitler, S. V. Morozov, V. I. Fal'ko, M. I. Katsnelson, D. Jiang, F. Schedin, and A. K. Geim. Unconventional quantum Hall effect and Berry's phase of 2π in bilayer graphene. *Nat. Phys.*, 2(3):177–180, Feb. 2006.

[47] Z. Qiao, J. Jung, Q. Niu, and A. H. MacDonald. Electronic Highways in Bilayer Graphene. *Nano Lett.*, 11(8):3453–3459, Aug. 2011.

[48] G. Sallen, L. Bouet, X. Marie, G. Wang, C. R. Zhu, W. Han, Y. Lu, P. H. Tan, T. Amand, B. L. Liu, and B. Urbaszek. Robust optical emission polarization in MoS_2 monolayers through selective valley excitation. *Phys. Rev. B*, 86(8):081301, Aug. 2012.

[49] M. M. Scherer, S. Uebelacker, and C. Honerkamp. Instabilities of interacting electrons on the honeycomb bilayer. *Phys. Rev. B*, 85(23):235408, June 2012.

[50] D. Smirnov, A. H. MacDonald, W. Bao, J. Velasco, F. Zhang, L. Jing, B. Standley, M. Bockrath, and C. N. Lau. Evidence for a spontaneous gapped state in ultraclean bilayer graphene. *Proc. Natl. Acad. Sci. USA*, 109(27):10802–10805, 2012.

[51] R. E. Throckmorton and O. Vafek. Fermions on bilayer graphene: Symmetry breaking for B=0 and ν=0. *Phys. Rev. B*, 86(11):115447, Sept. 2012.

[52] M. Tinkham. *Introduction to Superconductivity.* Second Edition. Courier Dover Publications, 2nd edition, Apr. 2012.

[53] M. Trushin and J. Schliemann. Pseudospin in Optical and Transport Properties of Graphene. *Phys. Rev. Lett.*, 107(15):156801, Oct. 2011.

[54] M. Trushin and J. Schliemann. Polarization-sensitive absorption of THz radiation by interacting electrons in chirally stacked multilayer graphene. *New J. Phys.*, 14(9):095005, Sept. 2012.

[55] A. Vaezi, Y. Liang, D. H. Ngai, L. Yang, and E.-A. Kim. Topological Edge States at a Tilt Boundary in Gated Multilayer Graphene. *Phys. Rev. X*, 3(2):021018, June 2013.

[56] O. Vafek. Interacting fermions on the honeycomb bilayer: From weak to strong coupling. *Phys. Rev. B*, 82(20):205106, Nov. 2010.

[57] O. Vafek and K. Yang. Many-body instability of Coulomb interacting bilayer graphene: Renormalization group approach. *Phys. Rev. B*, 81(4):041401, Jan. 2010.

[58] A. Varlet, D. Bischoff, P. Simonet, K. Watanabe, T. Taniguchi, T. Ihn, K. Ensslin, M. Mucha-Kruczynski, and V. I. Falkò. Anomalous Sequence of Quantum Hall Liquids Revealing a Tunable Lifshitz Transition in Bilayer Graphene. *Phys. Rev. Lett.*, 113(11):116602, Sept. 2014.

[59] J. Velasco, L. Jing, W. Bao, Y. Lee, P. Kratz, V. Aji, M. Bockrath, C. N. Lau, C. Varma, R. Stillwell, D. Smirnov, F. Zhang, J. Jung, and A. H. MacDonald. Transport spectroscopy of symmetry-broken insulating states in bilayer graphene. *Nat. Nanotech.*, 7(3):156–160, Jan. 2012.

[60] A. Veligura, H. J. Van Elferen, N. Tombros, J. C. Maan, U. Zeitler, and B. J. van Wees. Transport gap in suspended bilayer graphene at zero

magnetic field. *Phys. Rev. B*, 85(15):155412, Apr. 2012.

[61] D. Xiao, G.-B. Liu, W. Feng, X. Xu, and W. Yao. Coupled Spin and Valley Physics in Monolayers of MoS_2 and Other Group-VI Dichalcogenides. *Phys. Rev. Lett.*, 108(19):196802, May 2012.

[62] D. Xiao, Q. Niu, and M.-C. Chang. Berry phase effects on electronic properties. *Rev. Mod. Phys.*, 82(3):1959–2007, July 2010.

[63] A. Yacoby, J. Martin, B. E. Feldman, R. T. Weitz, and M. T. Allen. Local Compressibility Measurements of Correlated States in Suspended Bilayer Graphene. *Phys. Rev. Lett.*, 105(25):256806, Dec. 2010.

[64] A. Yacoby, R. T. Weitz, M. T. Allen, B. E. Feldman, and J. Martin. Broken-Symmetry States in Doubly Gated Suspended Bilayer Graphene. *Science*, 330(6005):812–816, Nov. 2010.

[65] X.-Z. Yan and C. S. Ting. Absence of gapped broken inversion symmetry phase of electrons in bilayer graphene under the renormalized ring-diagram approximation. *Phys. Rev. B*, 86(12):125438, Sept. 2012.

[66] X.-Z. Yan and C. S. Ting. Possible broken inversion and time-reversal symmetry state of electrons in bilayer graphene. *Phys. Rev. B*, 86(23):235126, Dec. 2012.

[67] W. Yao, S. Yang, and Q. Niu. Edge States in Graphene: From Gapped Flat-Band to Gapless Chiral Modes. *Phys. Rev. Lett.*, 102(9):096801, Mar. 2009.

[68] A. F. Young, C. R. Dean, L. Wang, H. Ren, P. Cadden-Zimansky, K. Watanabe, T. Taniguchi, J. Hone, K. L. Shepard, and P. Kim. Spin and valley quantum Hall ferromagnetism in graphene. *Nat. Phys.*, 8(7):550–556, July 2012.

[69] H. Zeng, J. Dai, W. Yao, D. Xiao, and X. Cui. Valley polarization in MoS_2 monolayers by optical pumping. *Nat. Nanotech.*, 7(8):490–493, Aug. 2012.

[70] F. Zhang, J. Jung, G. A. Fiete, Q. Niu, and A. H. MacDonald. Spontaneous Quantum Hall States in Chirally Stacked Few-Layer Graphene Systems. *Phys. Rev. Lett.*, 106(15):156801, Apr. 2011.

[71] F. Zhang and A. H. MacDonald. Distinguishing Spontaneous Quantum Hall States in Bilayer Graphene. *Phys. Rev. Lett.*, 108(18):186804, May 2012.

[72] F. Zhang, A. H. MacDonald, and E. J. Mele. Valley Chern numbers and boundary modes in gapped bilayer graphene. *Proc. Natl. Acad. Sci. USA*, 110(26):10546–10551, June 2013.

[73] F. Zhang, A. H. MacDonald, H. Min, and M. Polini. Spontaneous inversion symmetry breaking in graphene bilayers. *Phys. Rev. B*, 81(4):041402, Jan. 2010.

[74] F. Zhang, A. H. MacDonald, B. Sahu, and H. Min. Band structure of ABC-stacked graphene trilayers. *Phys. Rev. B*, 82(3):035409, July 2010.

[75] F. Zhang, H. Min, and A. H. MacDonald. Competing ordered states in bilayer graphene. *Phys. Rev. B*, 86(15):155128, Oct. 2012.

[76] F. Zhang, D. Tilahun, and A. H. MacDonald. Hund's rules for the N= 0 Landau levels of trilayer graphene. *Phys. Rev. B*, 85(16):165139, Apr. 2012.

[77] L. M. Zhang, Z. Q. Li, D. N. Basov, M. M. Fogler, Z. Hao, and M. C. Martin. Determination of the electronic structure of bilayer graphene from infrared spectroscopy. *Phys. Rev. B*, 78(23):235408, Dec. 2008.

[78] L. Zhu, V. Aji, and C. Varma. Ordered loop current states in bilayer graphene. *Phys. Rev. B*, 87(3):035427, Jan. 2013.

Vita

Xiao Li was born in Fuzhou, Fujian, China in 1986. He received his Bachelor degree in Peking University in 2008 in Beijing, China. He started his graduate studies in the University of Texas at Austin in September 2008.

Permanent address: (e-mail) lixiaophy@gmail.com

This dissertation was typeset with LaTeX[†] by the author.

[†]LaTeX is a document preparation system developed by Leslie Lamport as a special version of Donald Knuth's TeX Program.